Recent Shaping of the Eastern Mediterranean Israeli Continental Margin by Landslides and Faults

Thesis for the Degree of Master of Science
submitted by:

Einav Reuven

Under the supervision of:

Dr. Oded Katz

Prof. Einat Aharonov

December, 2015

Department of Geology
Division of Earth Sciences
Faculty of Mathematics and Natural Sciences
The Hebrew University of Jerusalem

Abstract

The continental slope off the Israeli coast demonstrates morphologic disturbances, indicating that the margin sediments are unstable. This is thought to be due to the Messinian evaporites that lie beneath them, in addition to regular continental slope building processes. Because of the limited resolution of bathymetry and seismic data, previous studies focused only on the large scale disturbances and were unable to resolve small scale features that could indicate the significant processes in shaping the continental slope. Here we show that the geomorphology of the continental slope is strongly influenced by instabilities which continually shape the seafloor. We used new high resolution multi-beam bathymetry, as well as new seismic data, to map and study small-scale landslides and faults. We also found that the primary control on landslides formation is the angle of the slope and a primary control on faults formation mechanism is the flow of the Messinian salt basinward. From our observations we conclude that the seafloor is probably still geomorphologically active today. This approach is important to validate seismic and tsunami hazard models, and to plan the locations of gas lines and other seafloor infrastructure. It can also be used as a first case study of small scale failures in the Mediterranean Sea and shed light on processes of geomorphology instabilities in the Mediterranean Sea and similar environments around the world.

Table of contents

List of figures and tables

1. Introduction

This work studies submarine landslides and faults exposed along the Eastern Mediterranean continental margins, off the coast of Israel (study area is shown in Fig. 1). These slope failures and faults are now comprehensively mapped and analyzed for the first time, thanks to recently released high resolution bathymetry maps of the area (Fig. 2). Previous works studied mostly large scale failures along the continental slope and constrained them to salt tectonics processes, caused by the Messinian salt underlying the Plio-Quarternary sediments (Almagor, 1984; Garfunkel et al., 1979; Garfunkel & Almagor, 1984; Garfunkel, 1984; Gradmann et al., 2005; Almagor & Garfunkel, 1979; Almagor, 1980). The new bathymetric maps along with seismic cross-sections of the studied area enabled us to study for the first time the small and medium failures and to shed light on the basic processes controlling the morphology of the sea floor in the studied area.

Figure 1: The Levant basin at southeast Mediterranean Sea. Research area is marked by a red rectangle.

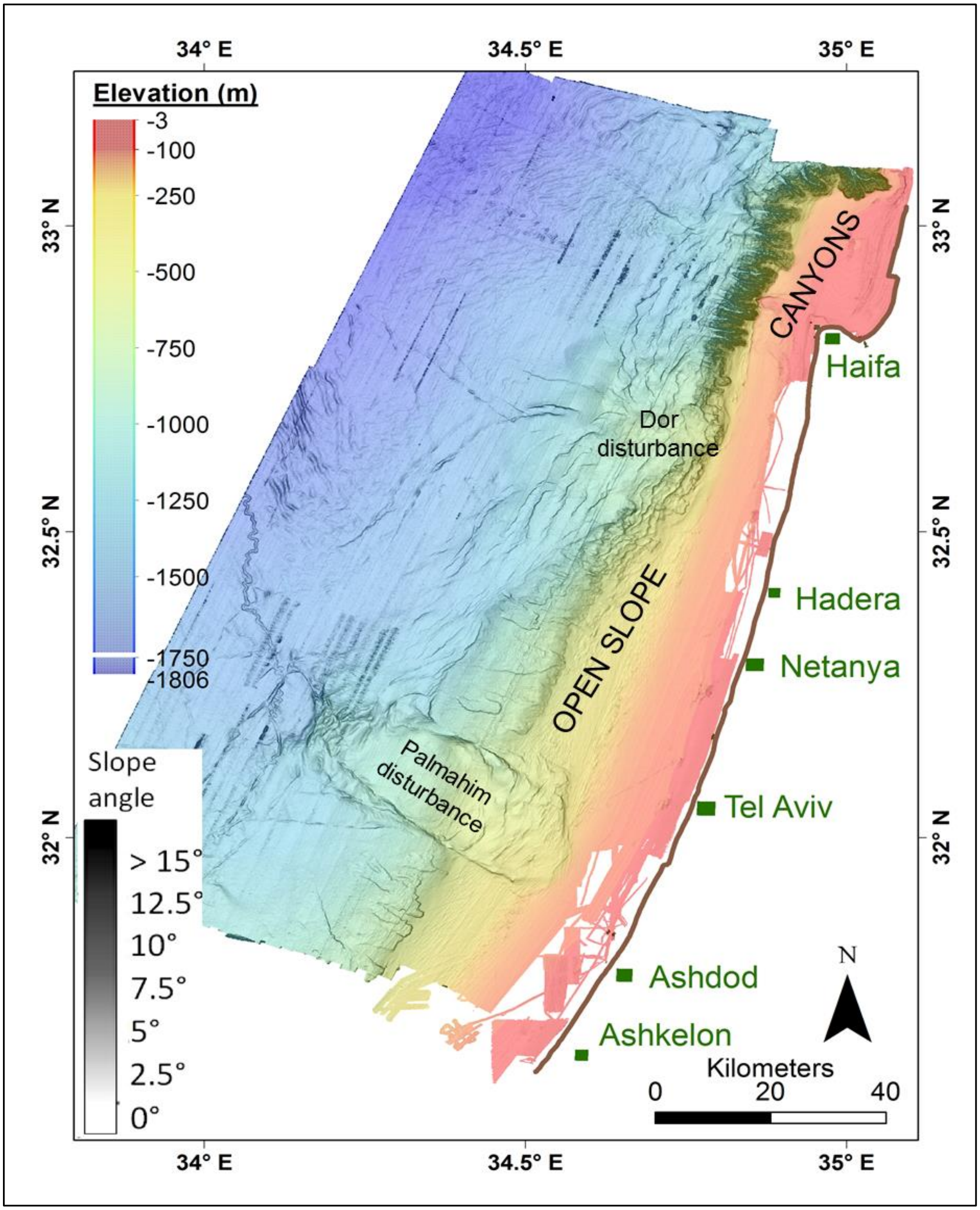

Figure 2: A map showing the bathymetry and the slope angle of the studied area (Sade, 2007; Sade et al., 2007; Tibor et al., 2013).

1.1. General overview of subaqueous near-shelf geomorphology

1.1.1. Submarine landslides

The term "submarine landslide" or "submarine slope failure" refers to an area of disturbed seafloor caused by the downslope movement of a failed mass (McAdoo et al, 2000), where the downward and outward movement of the slope material took place along one or several shear surfaces (Eckel, 1958; Schuster & Krizek, 1978). Submarine landslides are one of the main ways through which sediments are transferred across the continental slope to the deep ocean. In general sediments that had arrived from land (mainly by rivers) and from the continental shelf (by erosion and ocean currents) are often deposited at first stage on the upper continental slope. Their instability as unconsolidated slope deposits, together with other conditions (which will be detailed below) often lead to episodic slope failure and landsliding (Masson et al., 2006).

There are a few important differences between submarine and subaerial landslides (Hampton et al., 1996). First, submarine landslides may have enormous size in comparison to subaerial landslides. The largest known Quaternary subaerial landslide on Earth is the Mount Shasta 26 km^3 slide (Crandell et al., 1984); Whereas, the largest submarine landslide we are aware of, the Agulhas slide off South Africa, has a volume of 20,000 km^3 and is purported to have occurred as a single slope failure event (Dingle, 1977). Additionally, in general submarine landslides displace the sliding material a lot further than subaerial ones. The largest individual flow deposits that have been documented on Earth extends for 1,500 km offshore from northwest Africa (Talling et al., 2007 and references therein). Another difference is the slope angle. In contrast to subaerial landslides, submarine landslides can originate on nearly flat surfaces. For example, a seafloor slope of 0.5˚ on the continental shelf off the Malaspina Glacier in the Gulf of Alaska (Carlson, 1978) or slopes of 0.01˚ of the Mississippi River delta slides (Prior & Coleman, 1978 *in*: Hampton et al., 1996). The sediment in the sea can maintain only moderate slopes in comparison to sediment on land.

There are various conditions and factors promoting submarine landslide occurrence. The first and critical factor for landslide initiation is the force of gravity (Hampton et al., 1996). Another key factor is elevated pore pressure, leading to decreased frictional resistance to sliding, (Masson et al., 2006). Elevated pore pressures can result from transient processes such as earthquake shaking (Masson et al. 2006) or from long-term depositional processes. A mechanism for such pore pressure buildup is non-equilibrium consolidation due to high sedimentation rates of fine, low-permeability sediments (Urgeles and Camerlenghi, 2013). The third key factor for submarine landsliding is the occurrence of weak layers within the stratified sequences (Masson et al., 2006). Gas presence in the sediments also plays a role in destabilization of the slopes. Sultan et al. (2004), show that due to a temperature and pressure increase (e.g. following deglaciation), hydrates may dissociate. The disassociation of gas hydrates alters the bulk physical properties of the sediments (Urgeles et al., 2004) and makes them less stable. Simulation results (Sultan et al., 2004), as well as case studies on the Storegga slide, off shore western Norway (Bünz et al., 2005), show that sediment with increased gas content might liquefy during mobilization of the slide and show different flow mechanisms than sediments containing less gas. In places where evaporites are located under the sediments, salt tectonics can cause instability of the sediments (Garfunkel, 1984; Gradmann et al., 2005; McAdoo et al, 2000), in a mechanism that is explained below.

Triggers for submarine landslides are variable. They include: large storm waves (Hampton et al., 1996), rapid snowmelts (Malamud et al., 2003), intense rainfalls (Malamud et al., 2003; Hungre et al., 2014), sea level change (Camerlenghi et al., 2010), rapid accumulation and underconsolidation, gas charging, gas hydrate disassociation, low tides and volcanic island processes (Locat and Lee, 2000) or imposition of dynamic forces on the slope as a result of earthquakes (Hampton et al., 1996; Masson et al., 2006; Frydman & Talesnick ,1988; Haeussler et al., 2014; McAdoo et al., 2000).

The major hazards related to submarine landslides include destruction of seabed infrastructure by the moving mass, collapse of coastal areas into the sea and landslide-generated tsunamis (Masson et al., 2006).

Subaerial as well as submarine landslides' inventories present frequency-size (area or volume) distribution best fitted with a negative power law (Guzzetti et al., 2002; Malamud et al. 2004; ones Micallef et al., 2008; Urgeles and Camerlenghi, 2013). A power law distribution implies that when we compare the number of events of area size A or greater, with the number of events of size ηA or greater (where η is an arbitrary factor), the number always differs by the same factor of $\eta^{-\beta}$ (where β is an arbitrary factor), regardless of the absolute size of the events (Micallef et al., 2008). Two types of inventories are described in the literature: (1) landslide-event inventories that are associated with a single triggering event (e.g. earthquake); and (2) historical events' triggered landslide inventories, which are the sum of many landslide events that occurred over a long time period within a selected region. They include the cumulative effects of many landslide events that have occurred over tens to thousands of years (Malamud et al., 2004). Guzzetti et al. (2002) widen the observation also to historical long processed inventories. According to them, an historical inventory is composed of landslides which were not necessarily triggered by events. They emphasize the long process of many years that has created the inventory, which is the composition of old to recent landslides.

McAdoo et al. (2000), Micallef et al. (2008), Urgeles and Camerlenghi (2013) present size distribution of submarine landslides inventories. Similar to subaerial ones these inventories show sizes distribution best fitted by a negative power law, but with a different power law exponent. Plotting a size distribution enables the comparison of landslides inventories using statistical tools, as it provides an extensive view of each inventory as a whole.

1.1.2. Submarine landslide in the Mediterranean Sea

The Mediterranean Sea is characterized by its diversity in tectonic and sedimentary environments and therefore it enables a wide vision on different types of submarine slope failures as well as their causes (Camerlenghi et al., 2010) (Fig. 3). Camerlenghi et al. (2010) indicate that unlike megaturbidites or other types of mass transport deposits that cover the large areas of seafloor, submarine landslides in the Mediterranean are relatively small in size and have a total area of less than 400 km^2, and a total volume of less than 100 km^3. Most of the landslides originate on the mid-upper continental slope, in water depths generally shallower than 1,000 m, and generate scar heads mostly less than 40 m high. The largest landslides form scar heads of up to 200 m height. The information about landslides ages around the Mediterranean is not always accurate (Camerlenghi et al., 2010). Considering the youngest age estimation for every landslide, Camerlenghi et al. (2010) summarize that the vast majority of the landslides have occurred between 20 and

10 ka b.p. Available age information suggests that failures exceeding 1000 km^3 are infrequent and may recur every ~40 kyr. Smaller failures, that are >1km^3 may recur every 40 years (Urgeles and Camerlenghi, 2013).

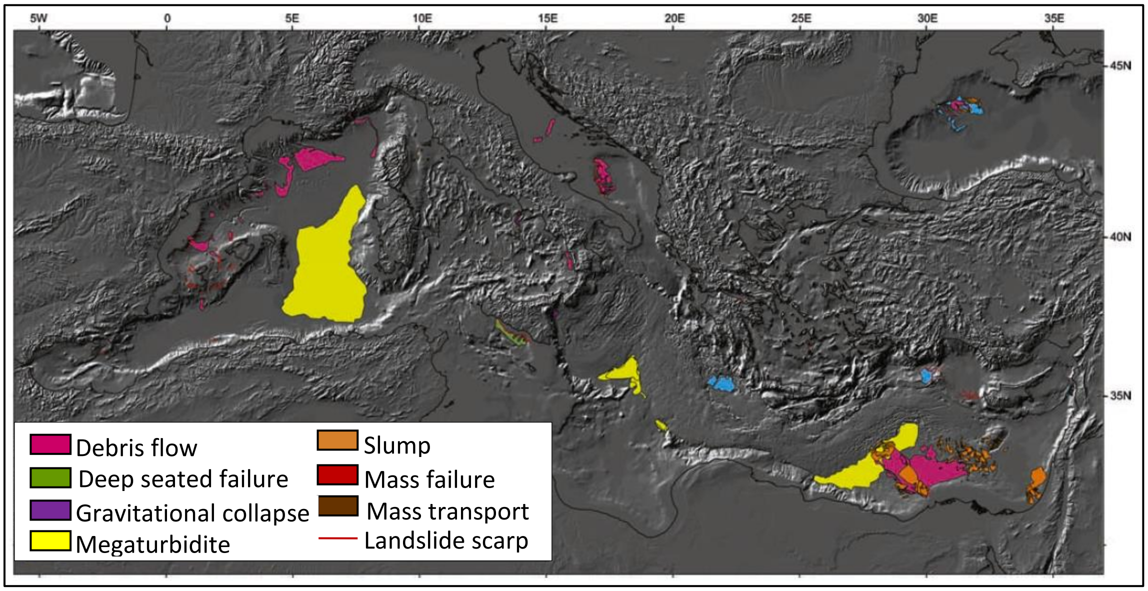

Figure 3: Submarine landslides around the Mediterranean superimposed to the shaded relief map of the bathymetry (Camerlenghi et al., 2010).

The landslides, as well as other mass failures, occur in varied geological settings of the Mediterranean continental margins, among them: aseismic, low sedimentation regions (Balearic); aseismic, large rated sedimentation (Nile deep sea fan, Ebro margin and Rhone deep sea fan) and; tectonically and salt-tectonically active regions (Levantine Basin). In contrast there is lack of evidence for modern submarine landslides at the accretionary wedges (deformation front of the Calabrian and Mediterranean ridges). Camerlenghi et al. (2010) concluded that submarine landslides are common on Mediterranean continental margins that are seismically inactive. Hence, they argue that the paradigm that earthquakes are the main triggers for large submarine landslides should be reconsidered.

Regarding tsunami hazard, Camerlenghi et al. (2010) claim that unknown tsunami sources most probably correspond to aseismic submarine landslides, hence the second most frequent cause of tsunamis in the Mediterranean basin, after sea floor rapture by earthquakes, are submarine landslides.

1.1.3. *Salt tectonics*

One of the mechanisms promoting slope instability and faulting that prevails in our research area is the salt tectonics caused by the Messinian evaporites (Garfunkel et al., 1979; Garfunkel & Almagor, 1984). Salt tectonics, also called Halokinesis, refers to all those processes that are connected with the movements of salt under the influence of gravity (Trusheim, 1987). The common usage of the term "salt" include all rock bodies composed primarily of halite (NaCl) (Hudec and Jackson, 2007). There are two main reasons which make salt inherently unstable under an overburden. First, under pressure, salt is mechanically weak, and deforms ductilly even at geologically rapid strain rates; second, salt is less dense than all moderately and fully compacted siliciclastic rocks and thus exerts buoyancy forces (Hudec and Jackson, 2007).

A few models of gravity gliding, i.e. movement of the overburden basinward due to gravity on a slope, were suggested (Humphris 1978; Martin, 1978 and; Gradmann et al, 2005). This movement can be caused either by the gravity force on the tilted continental slope or by differential loading of a seaward prograding shelf. The result of the overburden's displacement is extensional brittle structures such as listric normal faults (faults that their dip flattens with depth) and rotated blocks along the slope (Netzeband, 2006). The mobile salt layer also flows basinward along with the overburden (Netzeband, 2006). The extension on the slope also leads to mass accumulation in a compression zone at a deeper part of the basin (Netzeband, 2006). A transitional zone of mere translation between extension and compression zones of the sediment package may occur, depending on the distance between the two zones (Crans et al. 1980).

Opposing the flow of salt are two principal resisting forces: strength of the overburden and boundary friction within the salt layer. If driving forces are sufficient to overcome resisting forces, then salt flows (Hudec and Jackson, 2007). Otherwise, salt can remain static in the subsurface for tens or even hundreds of millions of years (Hudec and Jackson, 2007). Hudec and Jackson (2007) continue Kehle's idea (Kehle, 1988), suggesting that because salt behaves as a fluid over geological time scales, it is convenient to refer to it with hydraulic head in fluid statistics (Hudec & Jackson, 2007). A head gradient can be created as a result of one of two factors: differential thickness of the overburden or a tilted surface of the salt. Modern interpretations of salt tectonics suggest differential loading as the dominant force driving salt flow. A laterally varying overburden thickness above a horizontal, tabular salt layer produces a pressure head gradient but no elevation head gradient. Salt will flow along the pressure head gradient (Fig. 4a). The load variation may be produced by sedimentation (e.g., a river delta) or deformation (a stack of thrust slices at the left end of the section) or by erosion. A uniform overburden thickness above an inclined, tabular salt layer produces an elevation head gradient but no pressure head gradient. Salt will flow down the elevation head gradient (Fig. 4b) (Hudec & Jackson, 2007).

In addition, where a thin layer of salt exists, it can serve as a localized detachment plane (Hudec & Jackson, 2007). This structural style is dominated by listric growth faults and low-amplitude salt structures such as salt rollers.

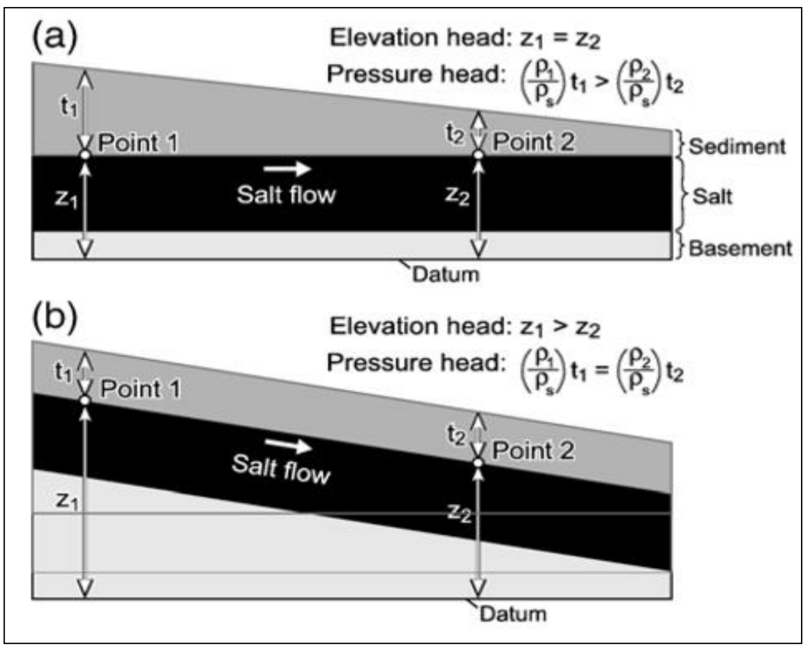

Figure 4: Examples of hydraulic head-gradient analysis in salt tectonics (Hudec & Jackson, 2007): (a) A laterally varying overburden thickness above a horizontal, tabular salt layer produces a pressure head gradient from Point 1 to Point 2 but no elevation head gradient. Salt will flow from left to right along the pressure head gradient. (b) A uniform overburden thickness above an inclined, tabular salt layer produces an elevation head gradient from Point 1 to Point 2 but no pressure head gradient. Salt will flow from left to right down the elevation head gradient.

1.1.4. Listric and Growth Faults

Listric faults, is a geometrical term, describing normal faults whose dip flattens with depth (Shelton, 1984). They can be formed in either sedimentary or basement rocks (Shelton, 1984). These faults may occur where brittle rocks overlie ductile rocks in an extensional regime (like in salt tectonics), as was suggested theoretically, using rock-mechanical and simulated model experiments (Gibbs, 1983; McCaly, 1990; McClay & Scott, 1991) and by foundation-engineering tests and failures. Shelton (1984) adds that, the flattening of the faults indicate an increase in ductility of the rocks with depth and sometimes deformation of the fault because of compaction or tilting of the up-thrown block. In cross sections listric faults may consist of several segments of short faults. This geometry is particularly characteristic of syn-sedimentary faults (growth faults). Indirect signs that may indicate the presence of listric faults in the subsurface are thick progradational sandstone overlying ductile strata and in some cases arcuate fault patterns, basins, or uplifts. Listric normal faults form during rifting, drifting, and evolution of passive continental margins with concomitant basinal development (Shelton, 1984). Listric faults restricted to the sedimentary prism are common features on passive margins, especially in progradational, post-evaporite sequences (Shelton, 1984).

Growth faults, is a mechanical term, describing a specific type of listric normal faults, which form contemporaneously with sedimentation, and are thus syn-sedimentary (Cazes, 2004). They are the structural expression to the inherent tensional stress system that characterizes the upwardly curved margin of a prograding continental platform. The geometries of these faults are related to the depositional character and history of the prograding margin (Galloway, 1986). In shelf and upper slope environments sedimentation rates often reach the rates of faults displacement, changing the stratigraphic thickness and enable to calculate the accumulated throw during the deposition (Baudon and Cartwright, 2008).

1.1.5. Salt tectonics in the Mediterranean Sea

Halokinetic related faulting around the Mediterranean is observed at the Levantine Basin (a subject that is presented in section 1.2.3). Only few works described these phenomena in other places around the Mediterranean:

Evans et al. (1987) worked on the North-eastern continental shelf and slope of the Mediterranean, between Cyprus and Turkey. They divided their research area to a few zones, among them: a zone of terraces (offshore Goksu Delta and offshore Anamur), a zone of faults, a zone with complicated slump structures and a zone of diapirism and anticlines. They suggest that the asymmetric supply of sediments to the Cilician Basin from the north and northeast has produced uneven loading that caused the underlying evaporites and associated sediments to flow. The faults in the outer part of the shelf are a result of the evaporites flow along with the foundering of blocks of overlying sediments. Halokinesis in their research area is suggested to be triggered at least partially by basement tectonics, an idea that was offered due to the agreement between the morphologic-tectonic zones and the salt structures in their eastward trend. Two mechanisms of flow were proposed: lateral flow due to asymmetric loading of sediment from the north and northeast, and vertical flow triggered by differential block subsidence (Evans et al., 1987).

Mascle et al., (2006) studied the Nile continental passive margin off Egypt. They reported that various features interrupt the Nile deep sea fan: channel-levee systems, turbiditity flows, sedimentary slope failures at various scales, massive mud expulsions and fluid seeps. They divided their research area to 4 main provinces, each of them containing different failure phenomena. The researchers suggest that the observed destabilization and strong tectonics of the 3 km thick Plio-Quaternary sediments are due to the salt-driven gravity tectonic activity caused by the 1-3 km thick Messinian salt underlying them. One example is the central province. A wide part of the south of the central province was elevated during the Messinian period, resulting in lack of salt deposits. Above this part Plio-Quaternary sediments are almost undeformed. However, around this platform the post-Miocene sediment cover is strongly affected by gravity spreading and\or gliding processes. They add that the transition between these two, stable and unstable, domains is well defined by the presence of growth faults (Mascle et al., 2006).

1.2. Study area

1.2.1. General Settings

Our study area is located on the submerged continental margin off the Israeli coast, from Ashkelon in the south to Haifa in the north, and from water depth of 50 m to water depth 1750 m, at about 80 km from the shore line (Figs. 2, 5 and 6).

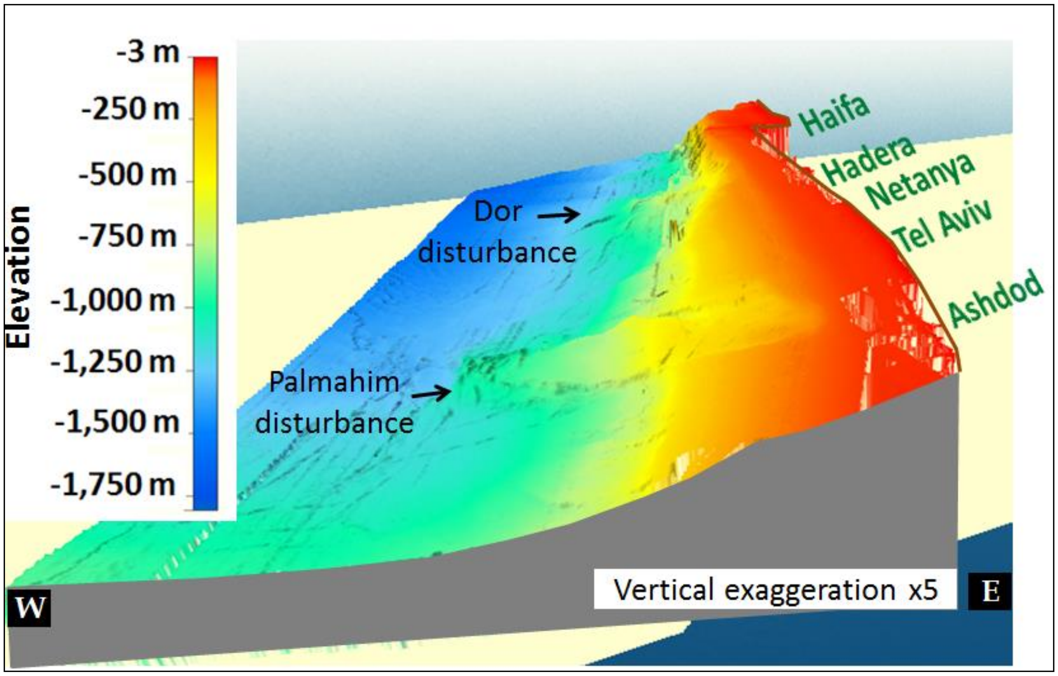

Figure 5: The Studied area elevation (a perspective view from south).

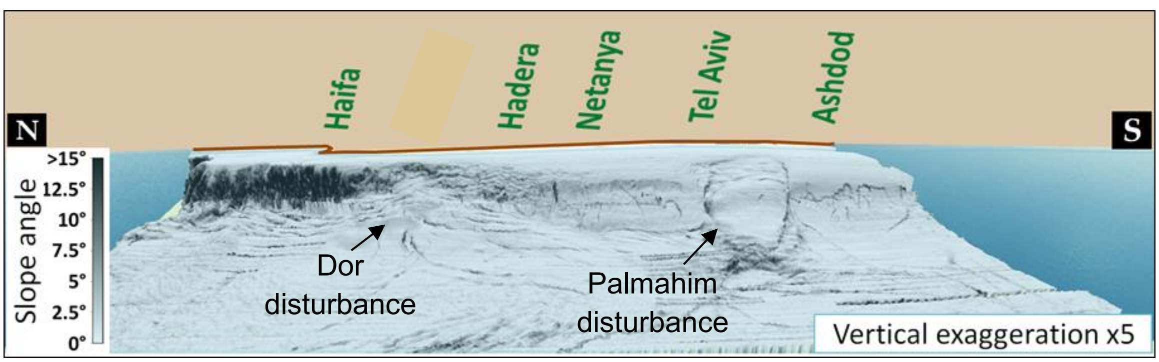

Figure 6: A perspective view of the studied area looking eastwards (from the basin towards the land). A Steep slope cut by canyons in the north, gradually changes southward to moderate open-slope with landslides.

Morphologically, the margins are divided into two provinces (Garfunkel & Almagor, 1984): (a) the Open Slope province (Fig. 2), off southern Israel to off Mount Carmel, which is characterized by a rather wide continental margin, a smooth and a rather rounded submarine topography, and a lack of submarine canyons; and (b) the Canyon province (Fig. 2), from off Mount Carmel and northward, there the continental margin is narrower, considerably steeper and is cut by numerous submarine canyons approximately perpendicular to the shoreline, the largest being Akhziv and Rosh-Hanniqra canyons.

The continental shelf in the studied area is 25 km wide off Ashkelon in the south and it narrows gradually northward up to 10 km off Haifa, then widens to 15 km off Acre, and narrows again to 3 km near the Lebanese border (Ginzburg et al. 1975) (Fig. 2). It extends to water depth of 0 -150 m, with maximum inclination of 0.5^0. The continental slope further west is about 6 to 12 km wide (Fig. 2). At the canyons province its inclinations is up to ~35˚. Southward from there, the slope's average inclination is $\sim 4^0$ and it is gradually decreasing southward: between south from Haifa and Netanya the inclinations gets to a maximum of ~10˚; and further south, from Netanya to Ashkelon it is up to ~5˚. The foot of the slope becomes shallower southward, from 1,500 m off northern Israel to 900 m in the south.

1.2.2. Geological history of the area

The Levantine basin is the easternmost region of the Mediterranean Sea (Gradmann et al., 2005) (Fig 1). It was formed by the division of the northern edge of the African-Arabian part of Gondwanaland in the early Mesozoic (Garfunkel, 1984). In the Cretaceous a convergence of the Arabo-African plate into the Eurasian plate generated the Alpine Orogenic Zone, as the Levantine basin remained south of the zone of intense tectonics. The Levantine zone was only mildly folded and faulted creating the "Syrian Arc" compressional structures, which are exposed on land, and extend in the sea at least until the base of the continental slope (Garfunkel, 1984). The breaking of the African – Arabian plate in the mid- Cenozoic epoch caused a seaward flexure, with a structural relief of 1.5- 2 km, and progredation of sediments over this relief formed the continental shelf and slope (Ginzburg et al., 1975; Garfunkel, 1984). These sediments - mostly clay and silt, were comprehensively derived from the African continental. They were deposited on the east Mediterranean margins since the late Eocene- Oligocene (Almagor and Garfunkel, 1979). In the Messinian the Mediterranean connection to the Atlantic

Ocean narrowed due to several reasons, such as tectonic uplift, sea level changes and climatic conditions. This process caused the Mediterranean desiccation (Hsu¨ et al., 1973, 1978). The consequences were (Almagor & Garfunkel, 1979; Garfunkel & Almagor, 1984): at the basin's margins - the formation of an extensive drainage system characterized by numerous wide canyons, 500 m- 1,000 m deep, cut into Miocene and older formations and; at the basin - the creation of a voluminous evaporitic series, hundreds of meters thick, in the Mediterranean under the Levantine platform. This marginal evaporitic facies is known from offshore and onshore drillings in Messinian and Pre-Messinian drainage channels (Gvirtzman & Buchbinder, 1976; Gradmann et al., 2005). It consists mainly of anhydrite, gypsum, rock salt and dark marly shales. Rock salt deposits, several tens of meters thick, were detected within the anhydrite sequences in a few boreholes between off Tel Aviv and off Ashkelon (Gvirtzman and Buchbinder, 1976). Carbonates and intercalated shales were also identified (Gradmann et al., 2005). Seismic images from the Messinian evaporites of the Levantine Basin show homogenous layers with intercalated reflections (Gradmann et al., 2005). Since the Messinian evaporites consist mainly of salt, and the salt plays a significant role in the formation of the morphology of the area, we occasionally refer in this work to the Messininan evaporites by the term 'salt' or 'Messinian salt', like Hudec and Jackson (2007).

Since the early Pliocene, Messinian evaporites and erosional regions were covered by sediments from Nile origin, mostly silt, clay (Almagor and Garfunkel, 1979), and landward sand (Garfunkel & Almagor, 1984). These sediments are dispersed on a large part of the southern Mediterranean Levantine basin, but a part of them were transported eastward by counterclockwise currents and were accumulated along the coast of Sinai, Israel and Lebanon (Almagor and Garfunkel, 1979; Garfunkel and Almagor, 1984). These sediments, which build the present coastal plain and continental margin (Almagor and Garfunkel, 1979), create a lens shape, which becomes narrower northward, away from the sediment's source (Garfunkel and Almagor, 1984, Ginzburg et al., 1975). Its width ranges from 100 km off northern Sinai to 3 - 5 km off Lebanon (Ginzburg et al., 1975). The continental margin off the coast of Israel is part of this lens. The Pliocene-Quaternary sediments sequence is thickest under the shelf-edge, reaching a thickness of 1.5-2.0 km. At the basin its thickness decreases gradually to a few hundred meters, and becomes thinner landward (Garfunkel and Almagor, 1984). The building of this sedimentary section was accompanied by progradation of sediments over the salt layer and propagation of the Levant shelf northwards and westwards (Gvirzman et al., 2015 and references there in). The present basin configuration, Pliocene–early Pleistocene, is marked by the edge of the Levant shelf reaching the deep basin salt layer and the continental slope collapsing downwards (Gvirzman et al., 2015 and references there in).

1.2.3. Morphology of the sea floor

1.2.3.1. *Disturbances*

Morphological features related to downslope mass movements are very common on the continental slope off Israel, and they locally affect 40% of the surface area (Almagor and Garfunkel, 1979). Up until recently, attention was mainly given to the most distinctive and large landslides on the Israeli continental slope, at least 10 km wide each, known as Palmahim disturbance (Garfunkel et al., 1977; Garfunkel et al. 1979; Almagor & Garfunkel, 1979; Garfunkel, 1984; Gradmann et al., 2005) and Dor disturbance (Garfunkel, 1984; Garfunkel & Almagor, 1984; Gradmann et al., 2005). Both were interpreted as large-scale seaward sliding of the post Messinian sediments forming blocks tilted landward on top of the Messinian evaporites (Garfunkel et al., 1979). Technological limitations prevented extensive previous research of the smaller landslides and slope failures.

1.2.3.2. *Growth faults*

Previous works mapped and interpreted the presence of the growth faults off Israel as a part of the mechanism of salt tectonics (Garfunkel et al., 1979; Almagor & Hall, 1983; Garfunkel, 1984; Garfunkel and Almagor, 1984; Frey-Martinez et al., 2005; Gradmann et al., 2005; Netzeband et al., 2006; Mart and Ryan, 2007; Cartwright and Jackson, 2008; Gvirtzman et al., 2015 and references there in). Many of the faults are considered to be still active and produce a terraced topography on parts of the continental shelf and slope (Almagor and Garfunkel, 1979; Almagor, 1980). The terraces are coast parallel and are up to 30 to 80 m high, 0.5 to ~2 km wide. Their lengths range from 3 to 10 km (Almagor and Garfunkel, 1979) (Fig. 7). The faults, which become flatter with depth, are rooted in the underlying Messinian evaporitic (Almagor and Garfunkel, 1979; Gradman et al., 2005; Gvirzman et al., 2015) (Figs. 7 and 8). It was suggested that these growth faults are formed where a thick series of Pliocene- Quaternary sediments lay upon relatively thick Messinian evaporitic sequences, as a result of gravitational sliding and rotations of large sediments blocks over the Messinian series (Almagor & Garfunkel, 1979; Garfunkel et al., 1979; Garfunkel & Almagor, 1984). Garfunkel and Almagor (1984) suggested that the pressurized fine clastics within the evaporitic beds act as a lubricant, which reduces the shear resistance of the evaporites, and allow them to flow under the sedimentary overburden. Gradmann et al. (2005) added that a new regional tectonics, parallel to the Dead Sea Transform, as well as diapirism and sedimentation, often superpose the process of gravity gliding. These processes were also suggested to be earthquake-triggered within the studied area (Almagor and Garfunkel, 1979). A recent extensive mapping of the sea floor, using higher resolution than before, revealed a complicated picture (Gvirzman et al., 2015), with faults and other morphological features over most of the Israeli Exclusive Economic Zone (EEZ). They identified three different contractional subdomains: (1) a radial fold system associated with the Nile Cone, accompanied by (2) a radial belt of conjugate strike-slip faults, and (3) a domain of wave-like ridges offshore northern Israel that is probably not related to salt tectonics (Gvirzman et al., 2015). Their observations showed that the circum-Nile radial fold system is not limited to the northern Sinai slope, but continues onto the Levant continental slope. They suggested that salt flow away from the Nile is strong enough that evaporites climb updip over the Levant slope and carry the Plio-Pleistocene overburden on top of them, and squeeze them against local rocks (Fig. 9).

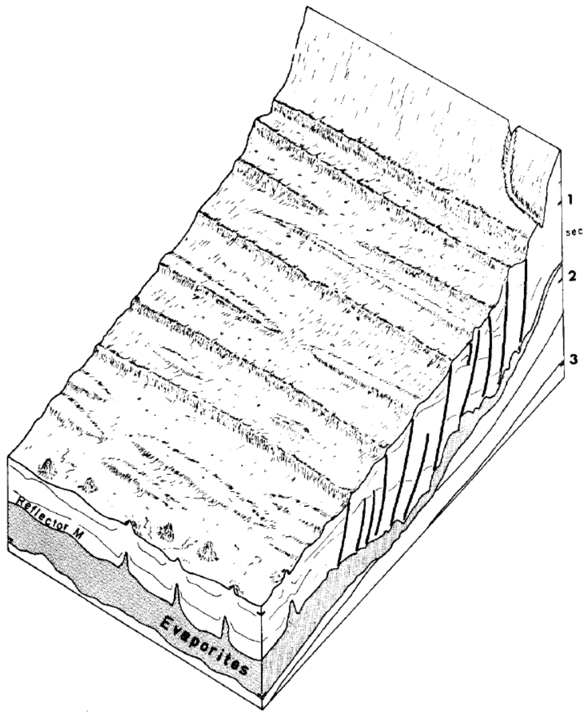

Figure 7: A Diagram showing faults and listric faults rooted at the Messinian evaporites (Almagor & Garfunkel, 1979). Vertical exaggeration = ~ 12 X.

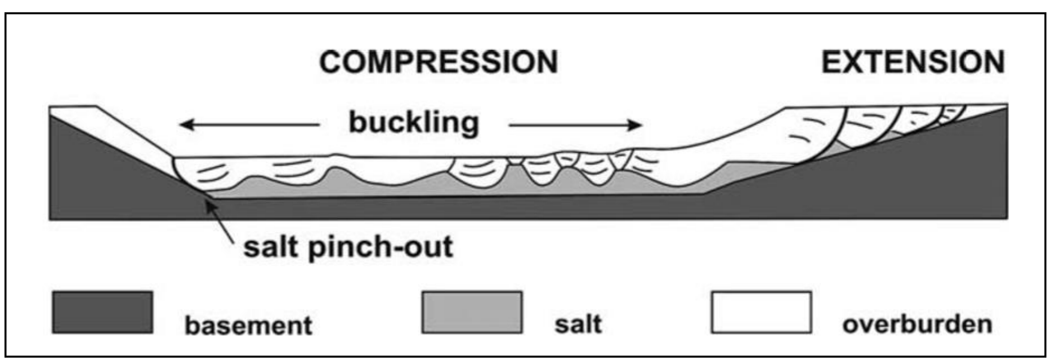

Figure 8: Model of gravity gliding (Letouzey et al., 1995 *in:* Gradmann et al., 2005). Gravity driven faulting above a viscous salt layer on the slope yields extension and basinward movement. This ceases where the salt layer pinches out and the overburden gets buckled and folded, showing a compressional stress regime.

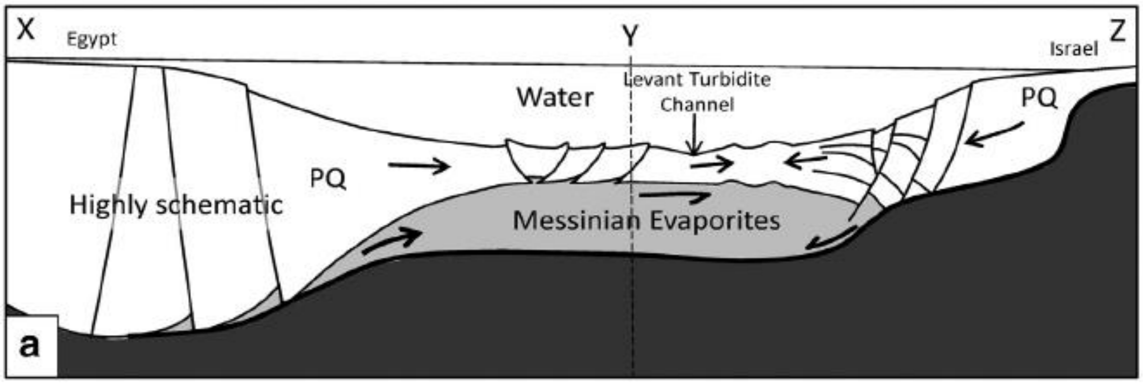

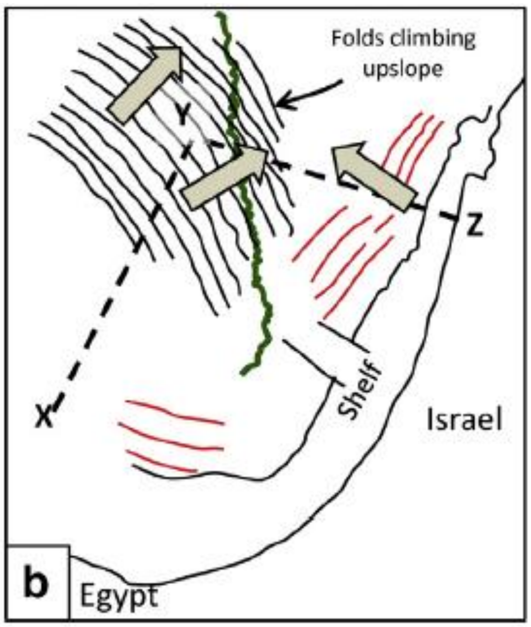

Figure 9: Salt flow and tectonic transport directions in Messinian evaporites and in Plio-Quaternary overburden (PQ), respectively (Gvirzman et al., 2015). (a) Schematic cross-section illustrating how salt is squeezed out by the Nile Cone overburden and flows northeastwards, pushing the Plio-Quaternary overburden up-dip over the Levant continental margin. (b) Observed pattern of the circum-Nile fold system (black lines) spreading over the Levant continental slope (red lines) east of the lowest area marked by the Levant Turbidite Channel (green line).

Here, we present additional observations regarding the faults spatial distribution and comparison with the salt thickness below them, as detailed below.

1.3. This work

In this work, we focus on the shallow, small to medium submarine landslides. These landslides occur along the open slope province off shore Israel, from south to Haifa - to Ashkelon. The nature of these slope failures is not comprehensively understood. Additionally, we examine the properties and distribution of the faults, especially regarding their field relations with the landslides and their spatial relation with the underlying Messinian salt.

New high resolution bathymetric data of the Israeli continental slope (Sade, 2007; Sade et al., 2007; Tibor et al., 2013) (Fig. 2) enable us, for the first time, to comprehensively map these numerous relatively small submarine surface features, in order to better understand their triggering mechanism, as well as the overall slope stability or instability of the area.

2. Goals and Objectives

The objectives of the research are to, first, identify and map the submarine landslides and fault scarps along the continental slope off shore Israel at higher resolution than ever before. Second, to analyze the processes that underlie the formation of the Israeli continental slope landscape, particularly with respect to the general morphology of the continental slope and to the Messinian evaporates underlying the continental margin. Understanding these processes will contribute to the understanding whether the continental slope off Israel is currently stable or unstable, and what are the conditions for future instability. Additionally, this will enable us to provide verification and validation to general geo hazard and earthquake hazard maps.

The above goals are achieved by the following steps:

1. Morphological mapping of the studied area (continental shelf and slope off shore Israel) using a bathymetric map, in particular submarine landslides and fault scarps. We focus on the shallow, small to medium, landslides with size range of 10^{-3} km^2 to 10^1 km^2.
2. Analysis of the nature of landslides (e.g. type, size, water-depth) and examination of statistical trends of position and properties of the landslide populations along the studied area, as well as the size distribution of the landslides. these trends are then compared to other landslide inventories studied around the world.
3. Analysis of crosscutting relations among the different landsliding events and among faulting and landsliding.
4. Creation of Messinian evaporates isopach using seismic cross sections and examination of the connection between the spatial distribution landslides and faults and the salt thickness.

5. Deducing constraints on the driving mechanisms for the submarine landslides and faults.

3. Research Importance

Mapping the small to medium landslides off shore of Israel, in high resolution, continues the previous mapping works of this area (Garfunkel et al., 1979; Almagor and Hall, 1980; Almagor and Hall, 1983; Gvirtzman et al., 2015) and provides a more detailed picture of the sea floor landscape. This enables an improved understanding of the stability of the continental slope, and provides information that can be used as the base for geo hazard analysis and regulations. It is also critical to the evaluation of the landslide and tsunami hazard, and in order to validate hazard models. Further implications are for the energy industry and infrastructure: this information is necessary for planning locations of gas lines and facilities on the seafloor.

4. Methods

4.1. Mapping:

4.1.1. Bathymetric grids

Bathymetric grids were used in order to map and study the submarine continental slope. The grids were made in the framework of the Israel National Bathymetric Survey (NBS), a joint project of the Israel Oceanographic and Limnological Research Institute and the Geological Survey of Israel (Sade, 2007; Sade et al., 2007; Tibor et al., 2013). The resolution is 15 m up to water depth of 700 m, and 50 m between water depths of 700 - 1750 m. The maps were prepared using Global Mapper v13.2 (kindly made available to us by Dr. John K. Hall) and ArcGIS programs.

4.1.2. Landslides

Landslides were manually mapped as polygons. They were defined (similar to McAdoo et al., 2000) as areas of rapid change in slope gradient, with a shape of sub-arcuate head scar and extending sub-parallel sidewalls (Fig. 10). Thus only landslides that are exposed on the surface were mapped. Other properties that were analyzed, in order to identify the landslides, were different roughness of the inner part of the landslide in comparison to its surrounding, as well as rubble deposited at the base of the landslide. We mapped all the landslides in the studied area with areas larger than 0.002 km^2. Where recognized, landslide deposit was included in the landslide area. In places, it could not be identified and thus the mapped landslide area is the minimal area. Additionally, we mapped the scar area for every landslide. Disturbed surfaces which didn't have a clear head scar were not mapped and thus the mapped area is an underestimate of the true total disturbed area. Relevant spatial and bathymetric characteristics of each individual mapped landslide were measured directly using the grids and the mapped polygons. Characteristics of all the individual landslides were summarized in a database. The database (Table S1 in supplementary data) includes the following properties: **Location** of the Landslide, marked by the (global) coordination of the head scar center; **Hierarchy**: We divide the complex landslides to three generations according to their order of failure, based on cross cutting relations. A 'Primary' landslide, the first in the hierarchy, is a failure that occurred on the original continental slope without an evidence of a former landslide on the same place. A 'Secondary' landslide is a failure that took place on the scars of the primary landslide, probably as a result of the over-steepening of the landslide' scar. The deposited material of the secondary landslide is often found within the scar of the primary one. In the same way, a 'Tertiary' landslide is a secondary failure to the secondary landslide, occurring on its over-steepening scar and its deposit is observed within the surface of the secondary landslide. For every primary landslide there can be several secondary landslides; **Size**, measured as the scar and deposit surface area enclosed in the landslide polygon (calculated by the Global Mapper Program); Minimal and maximal elevation measured at the scar head and at the toe, respectively; **Scar height**: the maximum altitude difference on the head scarp perimeter; **Type of landslide**: 'soil slump slide', where deposited material is present at the base of the landslides (Hungr et al., 2014), vs. ‘flow slide’ (Hungr et al., 2014), where the deposited material liquefied and flowed down the slope; The **field relation** of each landslide with the fault scarps, whether a landslide is triggered from the fault scarp, covers the fault scarp or is cut by it.

Slope angles of intact slope around the scars were calculated using the ArcGIS program. A strip of 250 m outside each landslide's scar was marked in a polygon on top of a slope angles map. For each polygon, containing numerous pixels, the program calculated the average value. Then we summarized the frequency of each value for all the landslides together in a histogram.

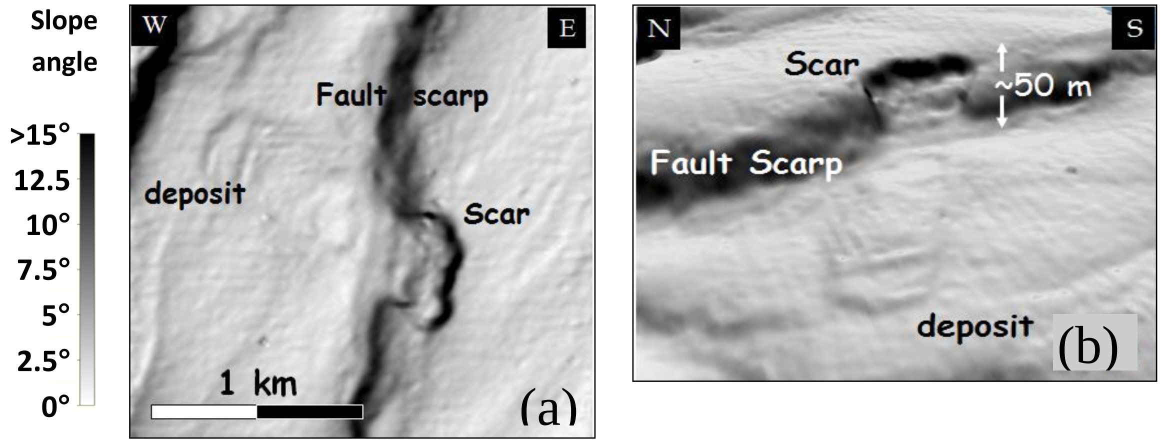

Figure 10: A map view (a) and a perspective view (b) of a simple landslide and a fault scarp (location in Fig. 11). The deposit material below the scar is elevated in comparison to its surrounding.

In addition, the **slope angles** within the landslides were measured for a sample of 47 landslides divided to groups of Northern and Southern landslides, and of Primary, Secondary and Tertiary landslides (Table 1). Three typical angles were measured: Head scarp (the steepest and upper most part of the scar), Deposit (slope material that had been displaced and deposited below the scar) and Toe (the lowest part of the deposited material). Each typical area was enclosed by a polygon containing numerous pixels and a mode (most frequent) value of the slope angle within each polygon was calculated using the Global Mapper program. Then we calculated the average of the modes for each type of areas (Head scars, Deposits and Toes), divided to the groups.

4.1.3. Fault scarps

Faults were manually mapped as polylines. They were defined as lineaments longer than 1 km, which form a step like morphology with a steep slope, up to more than 20° (Fig. 10).

4.2. Statistical analysis

We statistically examined the landslides size distribution following Malamud et al. (2004). There, the probability density function, $p(A_L)$, is defined as Equation 1:

(1) $$p(A_L) = \frac{1}{N_{LT}} \frac{\delta N_L}{\delta A_L}$$

Where N_L is the number of landslides with areas between A_L and $A_L + \delta A_L$, and N_{LT} is the total number of landslides in the inventory. We used the LStats tool developed in the frame of FP7- LAMPRE project (Rossi et al., 2012) to calculate the probability density function of our landslides inventory and compare it to other landslides inventories studied elsewhere.

4.3. Seismic analysis

4.3.1. Seismic cross sections

We used 2D (TGS-NOPEC Geophysical Company L.P) and 3D (Modiin Energy) seismic surveys, acquired for oil and gas exploration, to analyze the subsurface structure of the study area. Seismic material was interpreted using HIS's Kingdom 8.8 software of the seismic interpretation lab of the Geological Survey of Israel. The cross sections are either depth migrated or time migrated. We converted the time migrated sections to depth sections by multiplying the time by the average velocity of seismic waves in each medium. The velocities we used were 1500 m\s in sea water, 1800 m\s in the Plio-Quarternary sediment and 4200 m\s in the Messinian evaporates (following Gardosh and Druckman, 2006). The sections were correlated to wells where these were available. The resolution limitation of the seismic sections enabled us recognize layers whose minimal thickness exceeded 100 m. In places where the salt is thinner, we were not able to determine what its exact thickness was. Where M reflector (which represents the top Messinian) and N reflector (represents the base Messinian) were observed attached to each other, we referred to this location as a place with no salt.

We qualitatively examined structural figures correlated with the bathymetric map, in order to reveal the landslides' deep roots and their structural control, and the extent, structures and roots of the faults.

4.3.2. Isopach map

We prepared a salt isopach (salt thickness) map using the seismic sections, about 30 2D cross sections in TWT (~10 coast parallel cross sections and ~20 coast normal cross sections). We mapped by manually "picking": the bathymetry horizon, top Messinian horizon (M reflector) and base Messinian horizon (N reflector) as well as landslides and faults. Using the Kingdom program we interpolated each mapped horizon to a spatial time map. Then, using the ArcGIS, we calculated an isochron (time difference map) for the Messinian salt by reducing the top Messinian map from the base Messinian map. We converted the isochron to an isopach map by multiplying the average velocity of seismic waves in the Messinian evaporates (4200 m\s according to Gardosh and Druckman, 2006). The isopach map represents the salt thickness in each point.

We analyzed the spatial distribution of the landslides and faults, on top of the isopach map in order to examine their possible correlation. Each landslide or fault, is divided to pixels of 80m x 80m and the value of the isopach map is given to each pixel. Then, the data was summarized by histograms showing the frequency of salt thickness underlying the faults and landslides.

5. Results

5.1. Landslides

5.1.1. Nature of landslides

We mapped 447 small to medium landslides found between water depth of 100 m to 1000 m (Figs. 11 and 12, Table S1 in supplementary data). These landslides are shallow, observed on the current sea-floor, with a sliding plane within the uppermost submarine sediments (Fig. 11). Palmahim disturbance is not included here because it is a large landslide with a sliding plane on top of the Messinian evaporites, 1.5 km below sea-floor (Garfunkel, 1984). The total area of all mapped landslides is about 440 km^2, out of approximately 3500 km^2 (the sea floor area between water depth of 100 m to 1000 m).

Landslides areas (composed of scars and deposits) range from 0.0024 km^2 to 91.4 km^2 (Table S1 in supplementary data). Landslide widths range from 0.05 km to 5.5 km at the scar. Landslides' scars are up to 90 m high. Landslides follow either a ‘simple’ (Fig. 10) or a ‘complex’ (Figs. 13 and 14) nature. Simple landslides are defined as those that show evidence of a single slope-failure event, continuous, almost undisturbed, arc-like scar shape and a well constrained deposit. Complex landslides, on the other hand, are defined as those that show a hierarchical pattern, resulting from sequential, slope-failure events.

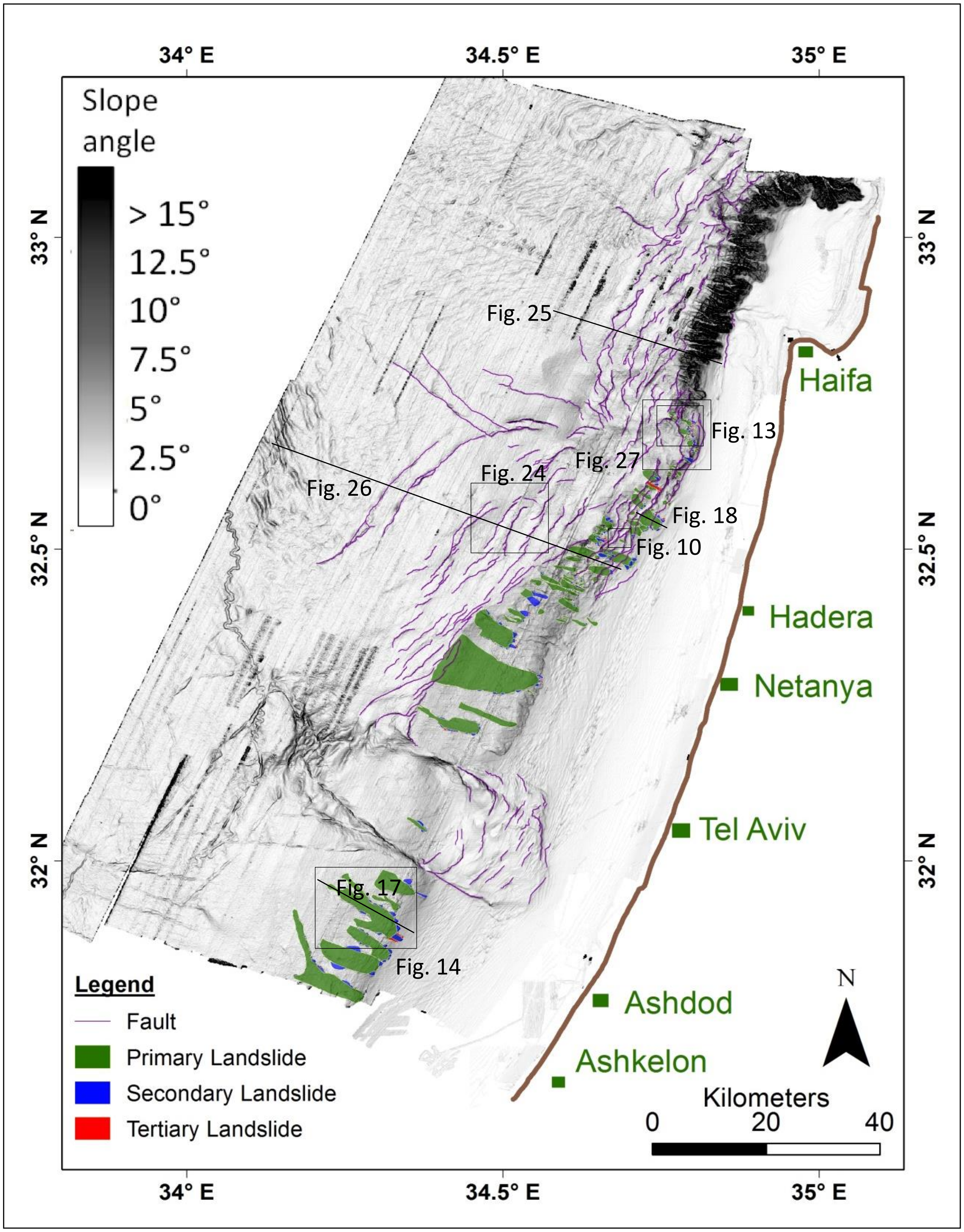

Figure 11: Mapped faults and three generations of landslides in the studied area, shown on top of a slope angle shader.

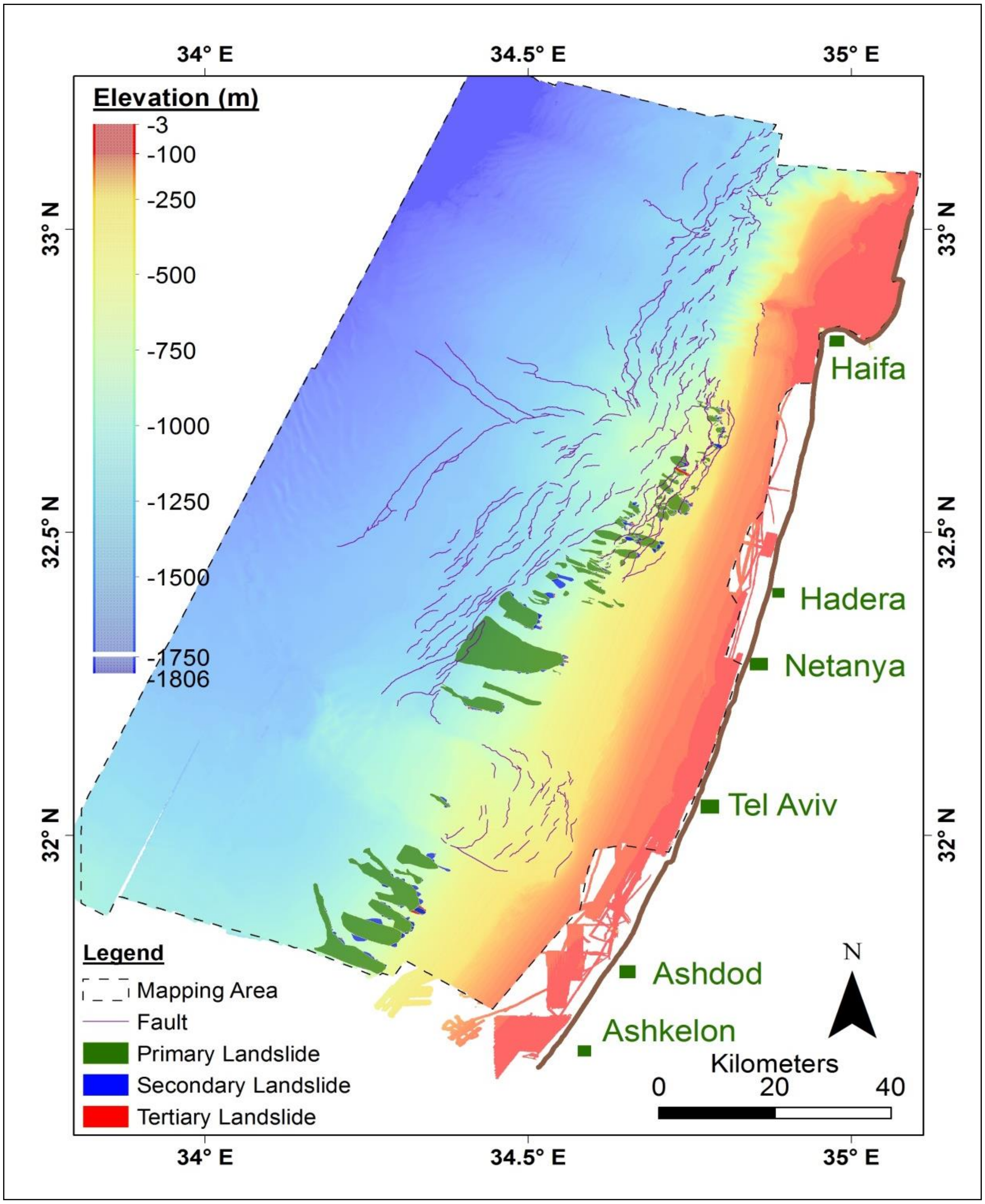

Figure 12: Mapped faults and three generations of landslides in the studied area, shown on top of an elevation map.

These landslides comprise a primary landslide, developed within the intact slope, and a few secondary landslides, developed in the over steepened (>10°) head scars of the primary one.

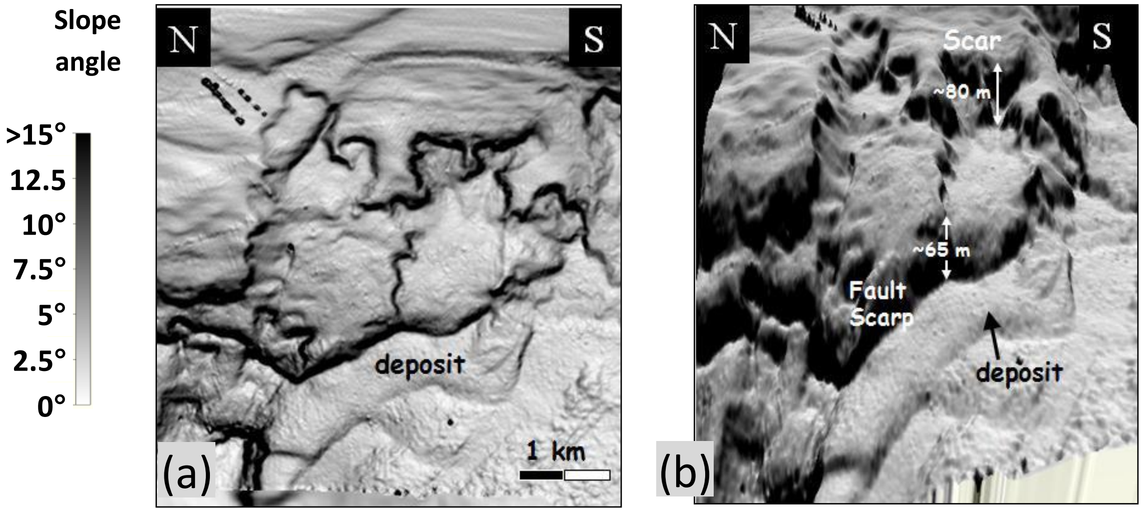

<u>Figure 13:</u> A map view (a) and a perspective view (b) of soil slump slide, characteristic of the northern part of the open slope (location is in Fig. 11).

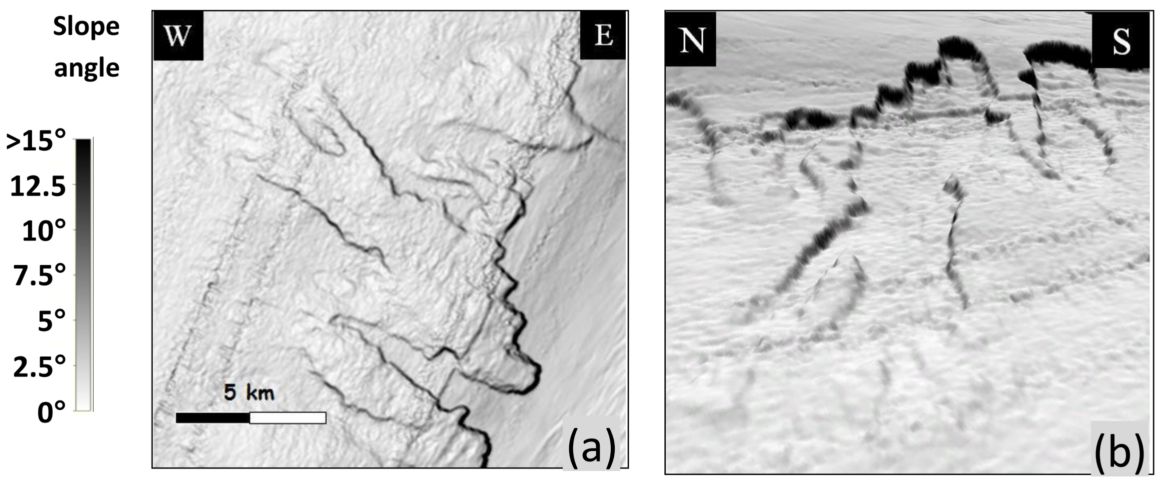

<u>Figures 14:</u> A map view (a) and a perspective view (b) of a flow slide, characteristic of the southern part of the open slope (location is in Fig. 11).

Secondary landslides are usually created in a retrogressive process, where serial sliding causes the migration of the slope failure due to progressive instability processes (Hampton and Lee, 1996). In other words, the over steepening on the scar head often causes more unstable material to fail, making a new scar head up the slope. We divided the complex landslides to three generations according to their order of failure, as was detailed in the methods.

It is more common to find soil slumps (Fig. 13) in the north of the studied area, and flow slides (Fig. 14) in the south. The difference in the landslide nature between north and south will be described and detailed below.

Average slope angles near the landslides were measured in order to examine connection between certain slope angles and slope failures. An average value was calculated from the pixels within a strip of 250 m around each scar. The average value of the slope outside of each scar is represented in the map in Fig 15 and the pixels' frequency of each value for all the landslides together is shown in a histogram in Fig. 16. The slope angels host most of the landslides scar areas are 3˚ to 7˚. Fewer scars areas are located at slope angles of 2˚ and slopes of 7˚ to 9˚.

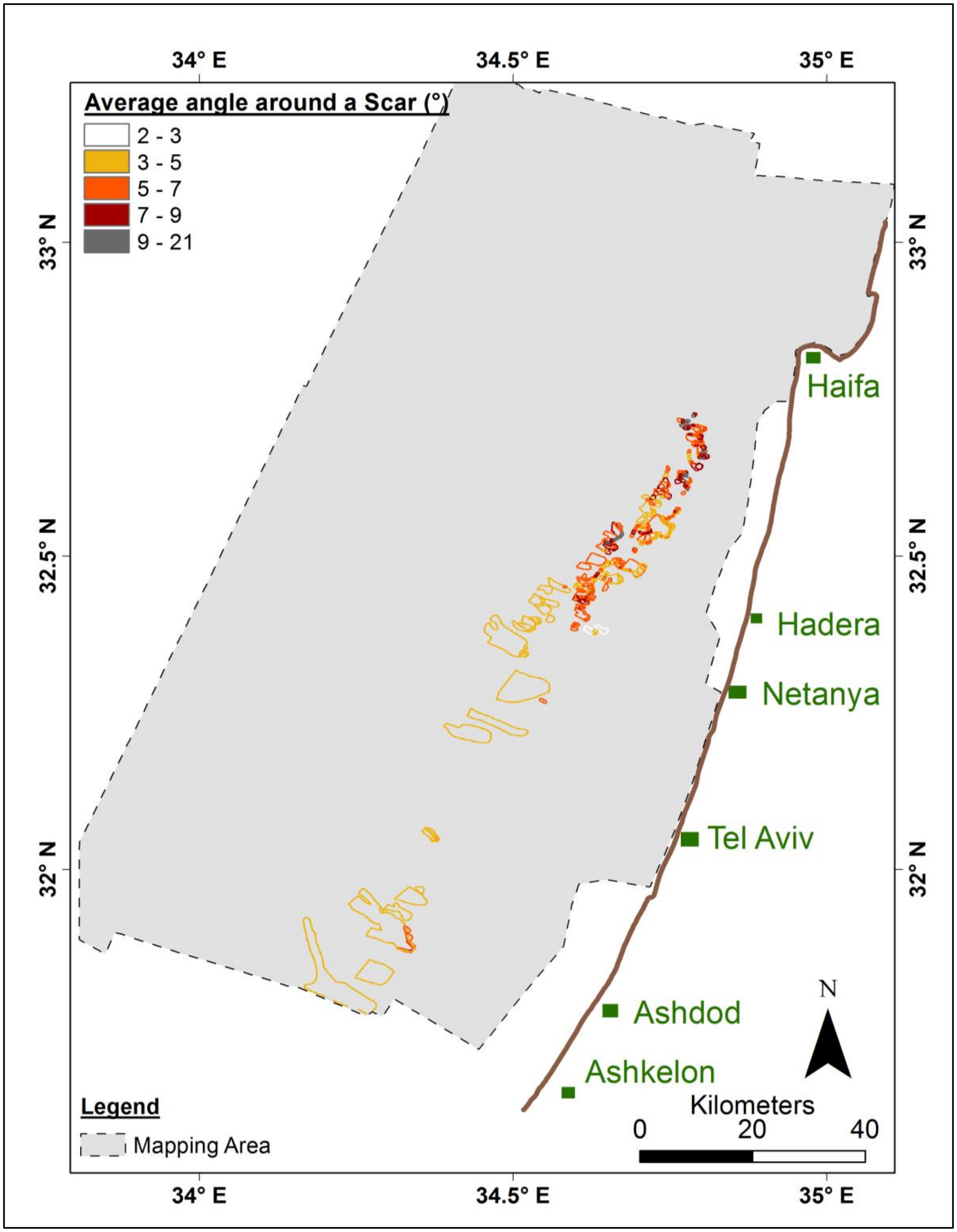

Figure 15: Slope angle around the landslides' scars. The value of each polygon is calculated as the average slope value of all the pixels in a strip of 250 m outside the scar.

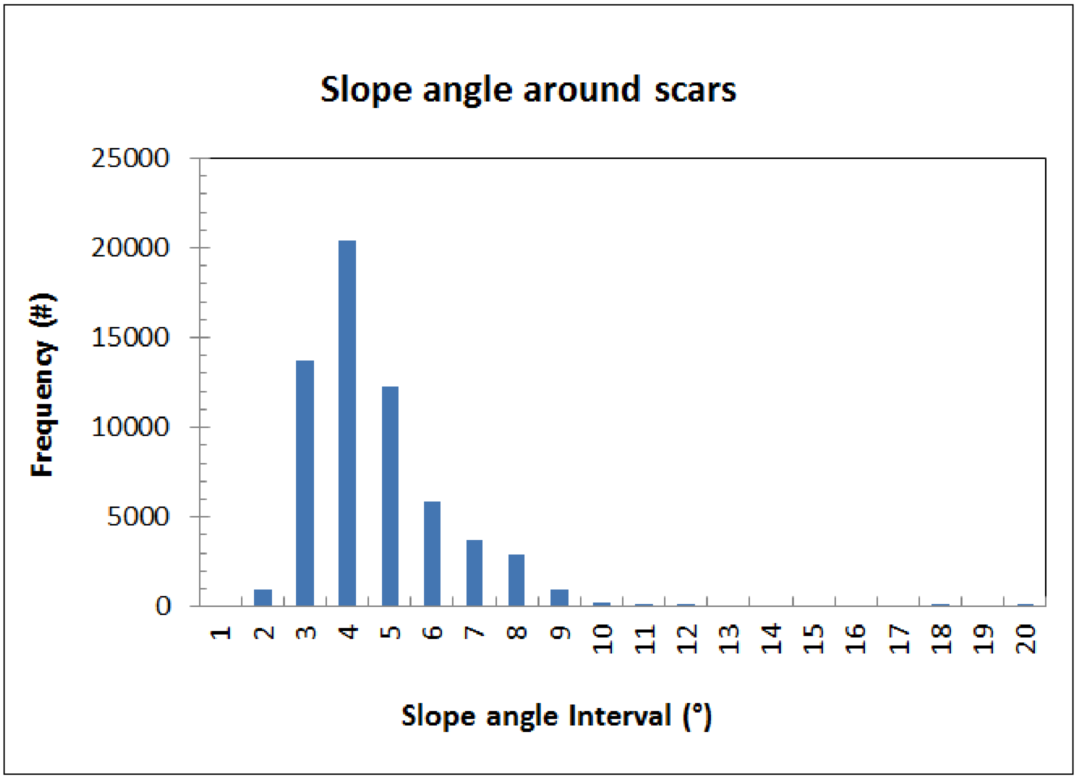

Figure. 16: A histogram that represents the data from the map in Fig. 15. the pixels' frequency of each value of slope outside the scars are summarized for all the polygons together.

Slope angles were measured within 44 selected landslides (Table 1), from both the northern and southern regions of the studied area, and including primary (P), secondary (S) and tertiary (T) landslides. The modes (most frequent values) of slope angles of the (25) northern landslides range between 5° - 17° with an average mode of 11° ± 3°. The 18 southern landslides range in mode values between 9° - 26° with a modes average of 16° ± 4°. Primary, Secondary and Tertiary scar head have similar mode average angles of 13° ± 7°.

Slopes of the deposits have lower angles than the slopes of the scar heads and similar slopes as the angles of the intact slope. for northern landslides deposit angles vary between 2°-6° with an average of 4° ± 2° and for southern deposits between 3°-9° with an average of 6° ± 2°. The slopes of the material at the toe have even lower angles of 1°-2° with an average of 1° ± 1°.

Table 1. Slope angle of the scar-head, deposit and toe of selected landslides. Landslides are grouped according to their location (North vs. South) and hierarchy (primary, P, secondary, S or tertiary, T). n is the number of landslides used for the calculation. Range, average and St. Dev. are the range, average and standard deviation of the slope mode (most frequent values) calculated over n landslides. Details of each selected landslide used in Table 1 appear in Table S1 (Supplementary data).

Description		**n**	**Range (°)**	**Average mode (°)**	**St. Dev. (°)**
Scar Head	All	43	5 – 26	13	4
	North	25	5 -17	11	3
	South	18	9 – 26	16	4
	P	6	5 – 26	14	7
	S	26	7 – 21	13	4
	T	11	7 – 13	12	3
Deposit	All	10	2 – 9	5	2
	North	5	2 – 6	4	2
	South	5	3 – 9	6	2
Toe	All	3	1 – 2	1	1

Scar and deposit (if exists) of landslides in the studied area can be observed also in seismic section (Fig. 17). Not all mapped landslides are observed on the seismic cross sections, apparently because of limited resolution. In the seismic cross sections there is also evidence for buried ancient landslide deposits and other discontinuities in the layers. However here we focus only on the landslides that are exposed on the sea floor.

The landslides' scars recognized using seismic cross sections fit well with the bathymetry (Figs. 17 and 18). Some landslides scars show spatial association with faults. Landslides' deposits create a small elongated chaotic area on the sea floor, elevated from its surrounding (Fig. 17). The sea floor in that part of the landslide is rough and disturbed.

Two appearances of structures are observed in the landslides: (1) Landslides that are disrupted by faults (Fig. 18), where the reflectors inside the landslide can be seen clearly, but are very disturbed - folded and cut - by numerous faults, which are observed below the landslide, and sometimes pass threw it up to the seafloor. The sliding surface of the landslide is usually hard to distinguish; (2) Chaotic Landslides (Fig. 17) with no observed interior structure. The material inside the landslide seems granular and chaotic. This granulation is usually an indication for the process of liquefaction that the sliding material has passed during the sliding (Hungr et al., 2014). The reflectors below the landslide are quite continuous.

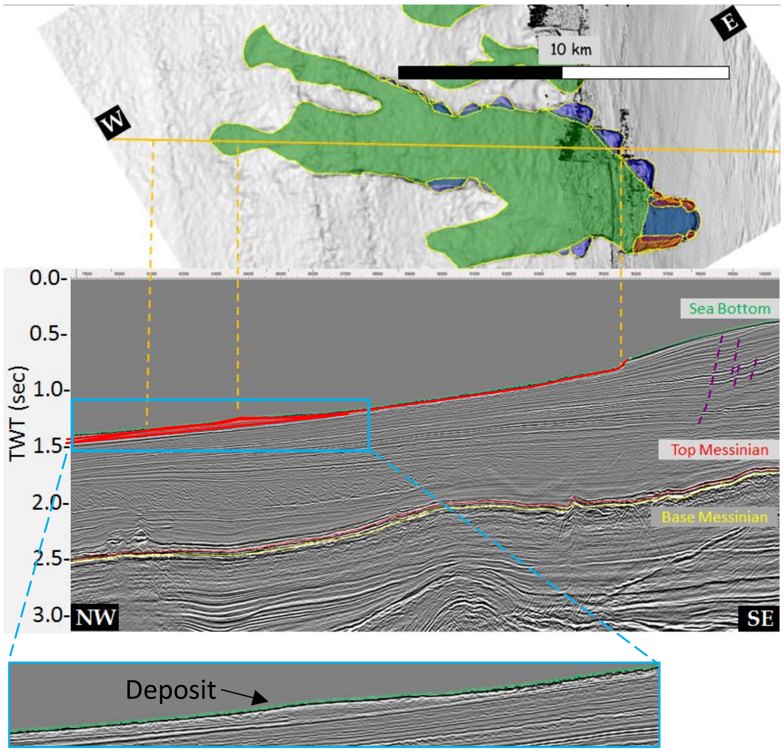

Figure. 17: Southern landslide in map view and in seismic cross section. Its location is in fig. 11. Sea bottom, top Messinian and base Messinian horizons are marked in green, red and yellow respectively. Faults are marked in purple and the landslide with its deposit is marked in red in the seismic section. In the small figure: the material inside the landslide's deposit seems granular and chaotic and it is elevated from the sea floor.

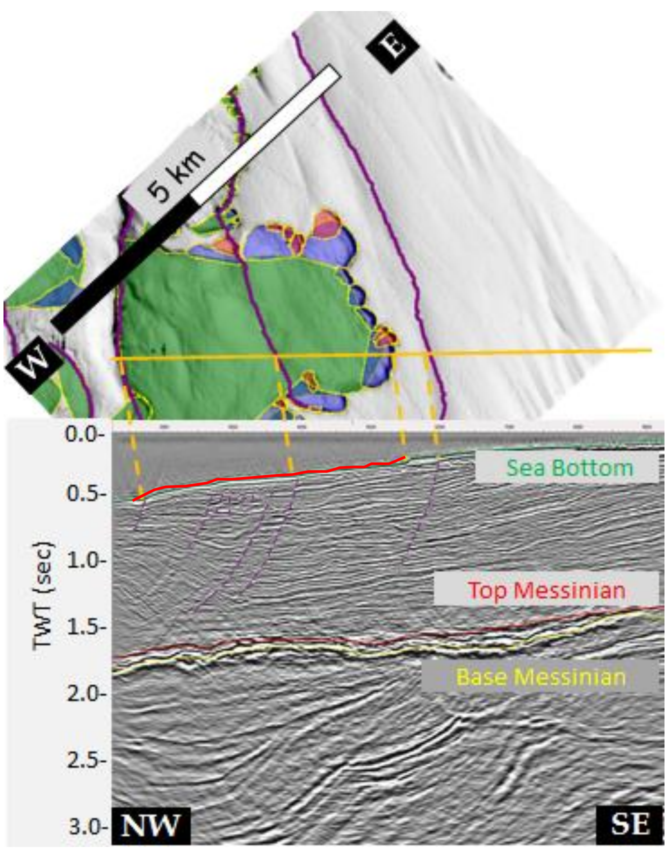

Figure 18: A map view and in a seismic cross section showing a landslide disrupted by faults, typical of the northern part of the studied slope. The landslide location is shown in Fig. 11. Sea bottom, top Messinian and base Messinian horizons are marked in green, red and yellow respectively. Landslide is marked in red in the section. Listric and normal faults are marked in purple in the seismic section. A few of them create a step on the bathymetry (marked in purple in the map view).

5.1.2. Size distribution of the Landslides

Landslides from different generations - primary (complex and simple), secondary and tertiary - comprise 89%, 10% and 1% of the mapped landslides area, respectively (Table S1 supplementary data). Landslides' character changes gradually from north to south, where the transitional zone is around landslide 260, Latitude ~32.45° (Table S1 in supplementary data). Landslides' areas are smaller in the northern section, showing prominent increasing southward (Figs. 12 and 19). This trend is strongest for the primary landslides, because these are the ones been affected by the variation of the regional topography where the secondary landslides are affected by the local slope of the primary landslides scars. The northern landslides (landslide 260 northward) have an average size of ~0.4 km^2 (median: 0.07 km^2) in comparison to southern landslides (landslide 261 southward) with an average size of ~1.9 km^2 (median: 0.1 km^2) (Table S1 in supplementary data). The northern landslides are located at relatively shallow water depths close to the shore-line (starting from ~100 m water depth, 9 km from the shore line). They gradually become deeper and further from the shore-line southward (reaching water depth of ~700 m, 29 km from the shore line) (Figs. 12 and 20).

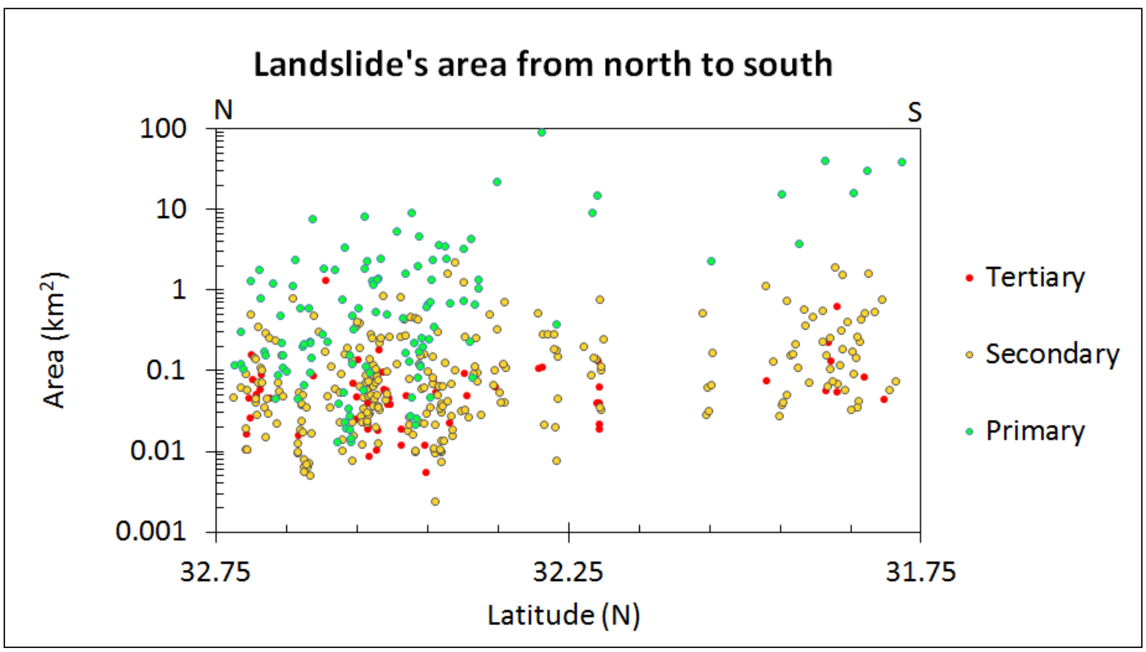

Figure 19: The size (surface area in a map view) of landslides as a function of their location.

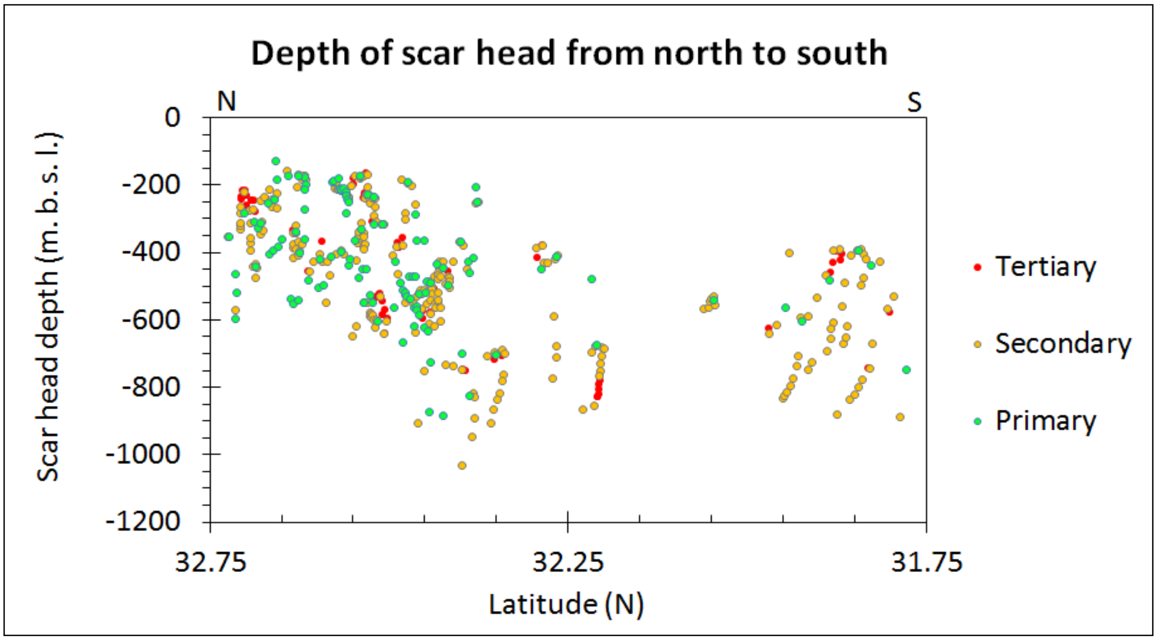

Figure 20: Depth of scar head as a function of landslide locations.

We statistically examined the size distribution of the landslides using the LStat program, for each generation of landslides separately and for the inventory as a whole. All the area distributions are described by an Inverse Gamma trend line (Equation 2).

Equation 2 (Rossi et al., 2012):

$$pdf(\chi|\alpha,\eta,\lambda) = [\frac{\lambda^{(2\alpha)}}{\Gamma(\alpha)}][\left(\frac{1}{\chi+\eta^2}\right)^{(\alpha+1)} \; exp^{-\left(\frac{\lambda^2}{\chi+\eta^2}\right)}] \qquad (2)$$

Where the parameter α controls the slope of the distribution for high values tail, η the slope for low values and λ the position of the maximum of the distribution functions (rollover, r).

Size distribution of primary landslides (with areas between 0.013 km2 to 91.6 km2) is shown in Fig. 21a (Equation 2). The most probable landslide area is 0.3 km^2 and the decay slope of the large landslides (α) is 0.69. Size distribution of secondary landslides (with areas between 0.002 km^2 to 2.2 km^2) is shown in Fig 21b (Equation 2). Most probable landslide size is 0.02 km^2 and the decay slope of the large landslides (α) is 1.03. Size distribution of tertiary landslides (with areas between 0.005 km^2 to 1.3 km^2) is show in Fig 21c (Equation 2). Most probable landslide size is 0.01 km^2 and the decay slope of the large landslides (α) is 1.31. The three generations together construct the whole inventory (Fig. 22, Equation 2) and best fit for comparison of our data to other landslides inventories. Most probable landslide size is 0.016 km^2 and the decay slope of the large landslides (α) is 0.67. The parameters of this distribution are shown in table 2 in the Discussion part.

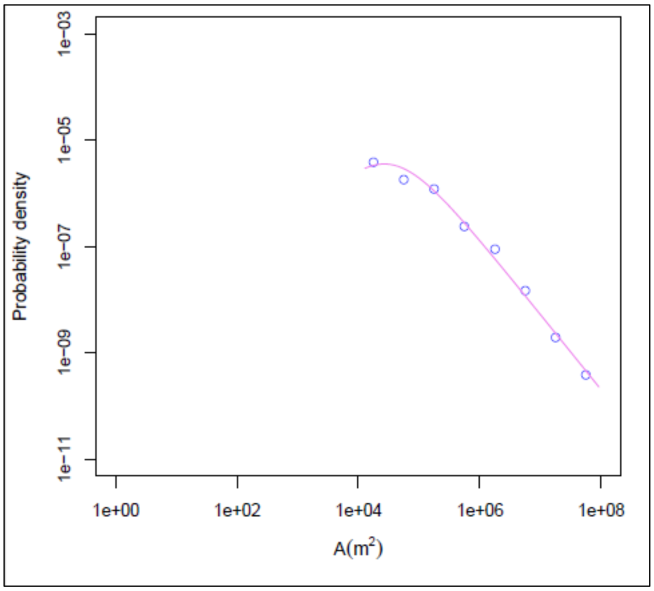

(a)

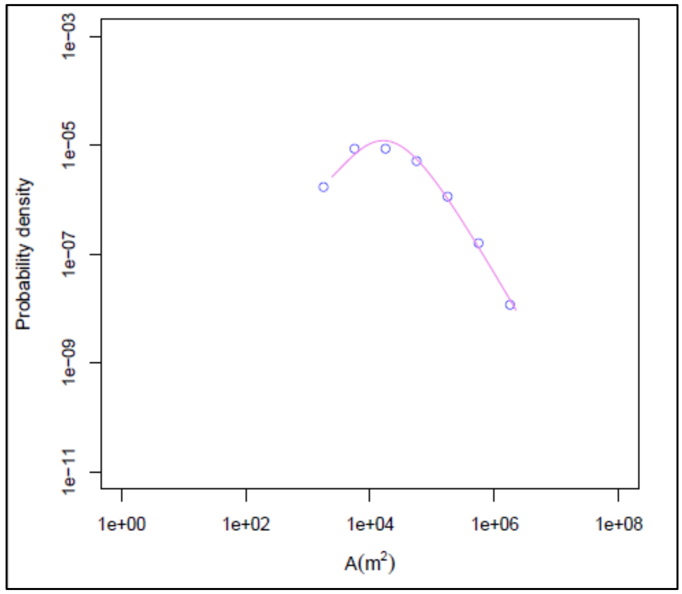

(b)

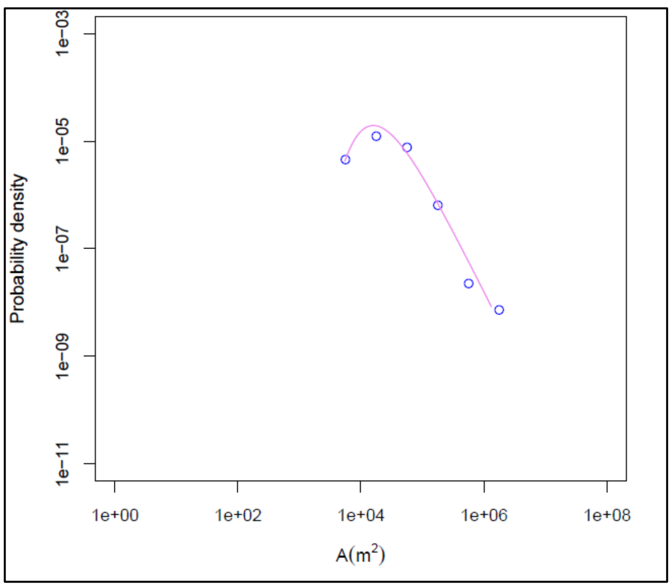

(c)

<u>Figures 21:</u> Landslides' size distribution for each generation, calculated by LStats tool (by Dr. M. Rossi, IRPI-CNR in frame of LAMPRE program). (a) Primary landslides (b) Secondary generation and (c) Tertiary landslides.

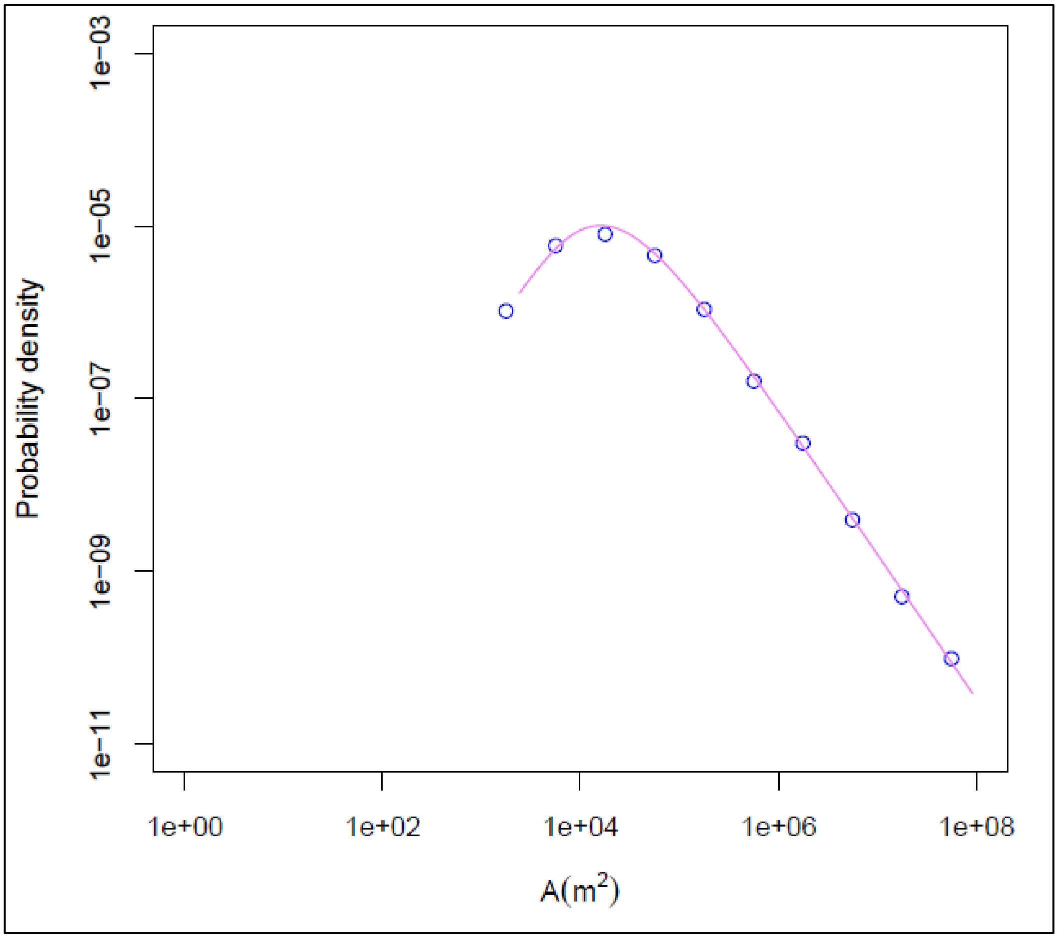

Figure 22: Size distribution of the whole landslides' inventory calculated by LStats tool (by Dr. M. Rossi, IRPI-CNR LAMPRE program). Statistical parameters are presented in Table 2.

5.2. Faults

We mapped elongated step- like features expressed on the sea floor which create a terrace-type morphology that trends generally N – S. These step- like features are interpreted as faults scarps (Almagor and Garfunkel, 1979). The faults scarps are up to 80 m high and are up to 35° steep (Fig. 10). Overall we mapped approximately 1260 km of fault scarps in total, where each individual fault segment is up to 30 kilometers long (Figs. 11 and 12).

We divided the faults into two main groups:

1) Segments sub-parallel to the shoreline. On east-west lines, crossing the entire studied area width, 10 – 15 North - South striking individual fault segments were traced. The offset between parallel faults scarps ranges from less than one to a few kilometers.

The locations of the faults are very variable regarding water depth, distance from the shore-line, location on the continental margin and slope angle of the area there. The faults are divided to five zones from north to south, according to their locations relative to the continental margin (Fig. 23): (a) Off north Israel, at the canyons' zone, the faults are located at the foot of the continental slope, about 20 km from the shore line at water depth 900 m and basinward (Figs. 12 and 23). They are located at slope angle of about 2°; (b) Between off Haifa and off Hadera, near Dor disturbance, the faults appear on the continental slope, starting from a distance of 15 km from the shore line at water depth of 100 m and basinward (Figs. 12 and 23). The slope angle of the undisturbed slope there is up to 6°. Other faults, which are located basinward in that zone are described below; (c) From off Hadera to off Tel Aviv, the faults are located further into the basin, starting from the foot of the slope, 35 km from the shore line at water depth of 1000 m. They occur at slope angle of 2° (Figs. 12 and 23); (d) in Palmahim disturbance the faults form the upper part of the disturbance, appearing on the continental shelf, 13 km from the shore line at water depth of 100 m. They are observed at slope angle of up to 2.5° (Figs. 12 and 23); (e) southern from Palmahim no faults are exposed on the sea floor (Figs 12 and 23).

2) Faults concentric about the Dor disturbance. Up to 8 pairs of faults segments, 3 - 20 km long (Figs. 11 and 12). These faults form a channel- like shape, as their scarps face each other, creating a graben-like structure area in the middle (Fig. 24). Their maximum separation is up to 2 km.

Faults are well observed in the seismic cross sections (Figs. 25 and 26). They displace layers' reflectors, causing discontinuities in the Plio-Quaternary sediments. Above minimal salt thickness (tens to hundreds of meters) where the salt layer is deformed, the faults are rooted at the salt or at the disturbed sediments above it in correlation to the salt's rollers (Figs. 25 and 26). This salt thickness is usually located basinward from the foot of the slope. Under the continental slope and shelf faults usually appear in the post Messinian sediments with no observed underlying salt. More results regarding faults distribution over different salt thicknesses are presented below.

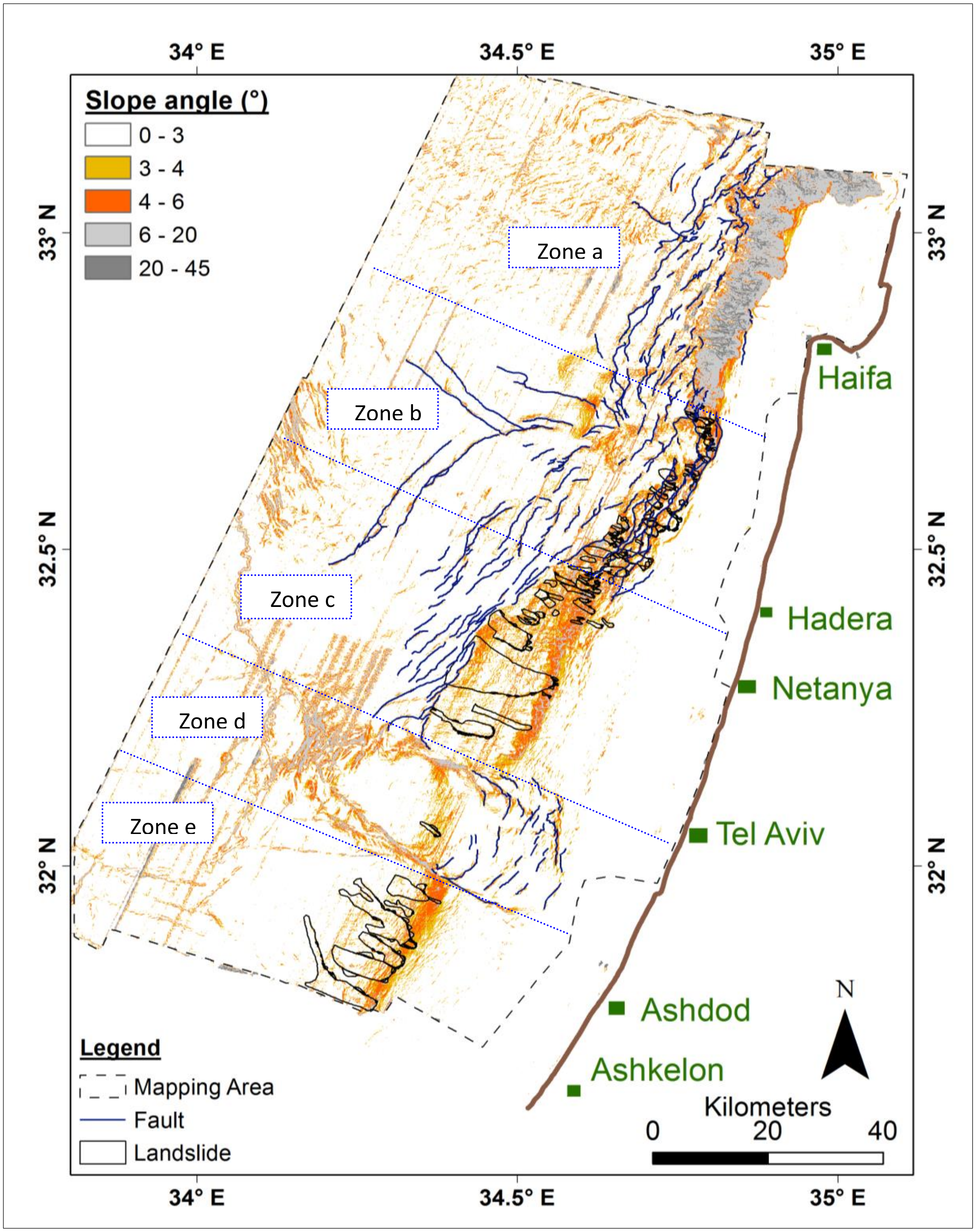

Figure 23: Mapped faults and landslides in the studied area, shown on top of a slope angle map.

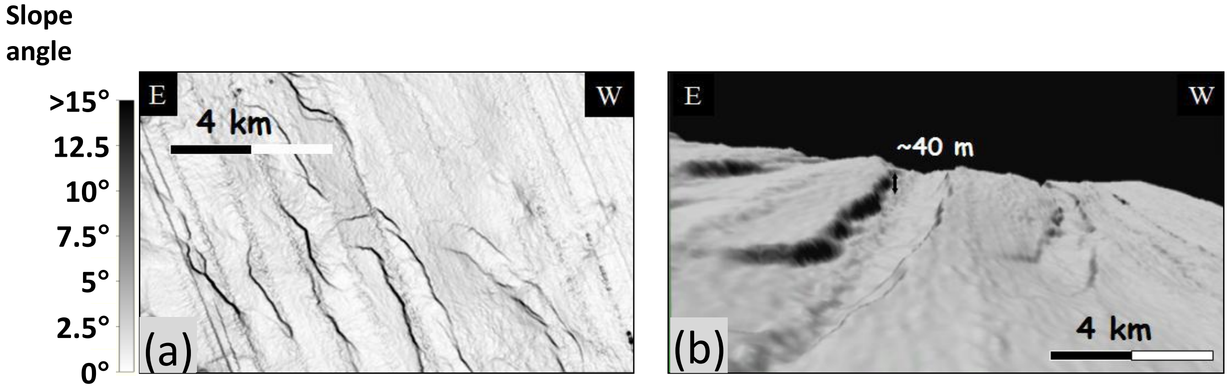

Figures 24: A map view (a) and a perspective view (b) of faults that form a channel like shape (location is in Fig. 11).

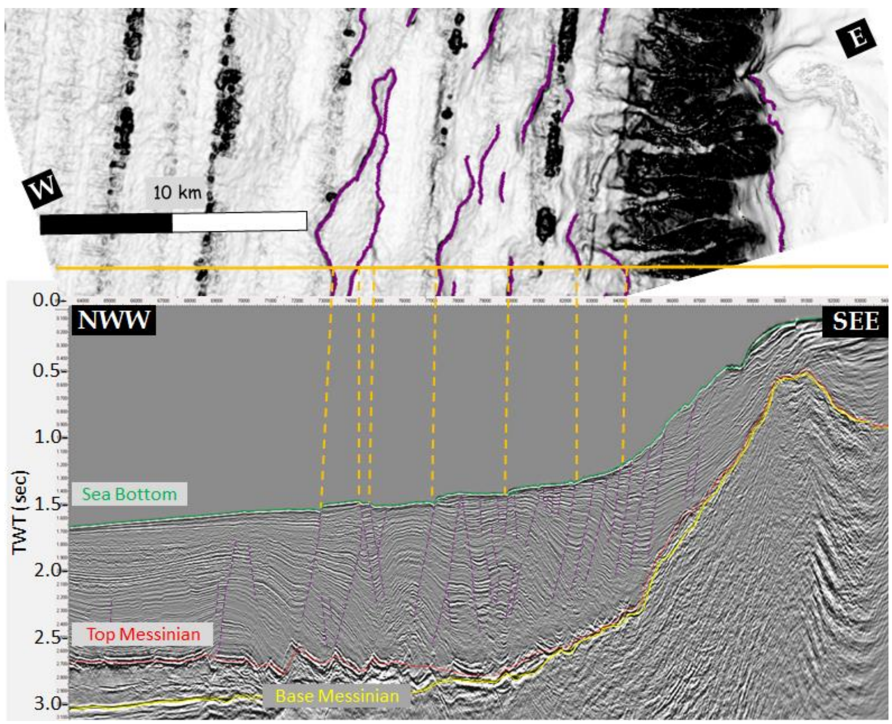

Figure 25: Faults in map view and in seismic cross section are marked in purple (for location see Fig. 11). Sea bottom, top Messinian and base Messinian horizons are marked in green, red and yellow respectively.

Faults observed in the seismic section sections are either expressed on the sea floor, creating step like features, or are covered by continuous reflectors and are not expressed on the surface (blind faults) (Figs. 25 and 26).

The faults were interpreted as syn-sedimentaric growth faults (Garfunkel et al., 1979; Garfunkel, 1984), formed contemporaneously with sedimentation and displace gradually thickening series of sediments (Garfunkel, 1984).

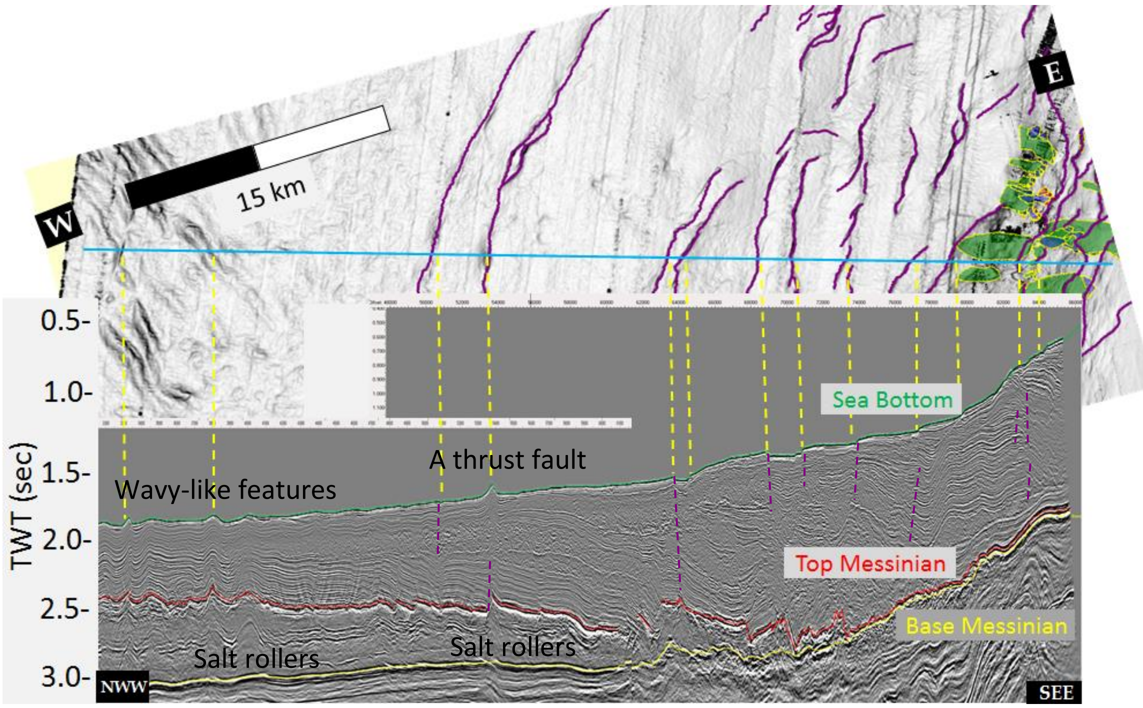

Figure 26: A seismic cross section of the studied area (for location see Fig. 11). Sea bottom, top Messinian and base Messinian horizons are marked in green, red and yellow respectively.

5.3. *Relation between landslides and faults*

Landslide and faults appear together only in zone (b) near Dor disturbance (Fig. 23). In this zone we find complicated cross cutting relations between the landslides and the fault scarps (Fig. 27). Fault scarps both cut landslides and are cut by other landslides. 83 of 447 mapped landslides have cross cutting relations with faults (Table 1 in supplementary data): 54 of these landslides are triggered from fault scarps, 14 of these landslides are cut by faults, 6 of the landslides deposits cover fault scarp. Another 2 both begin from fault scarps and cover other faults, and 7 are both cut by faults and cover other fault scarps.

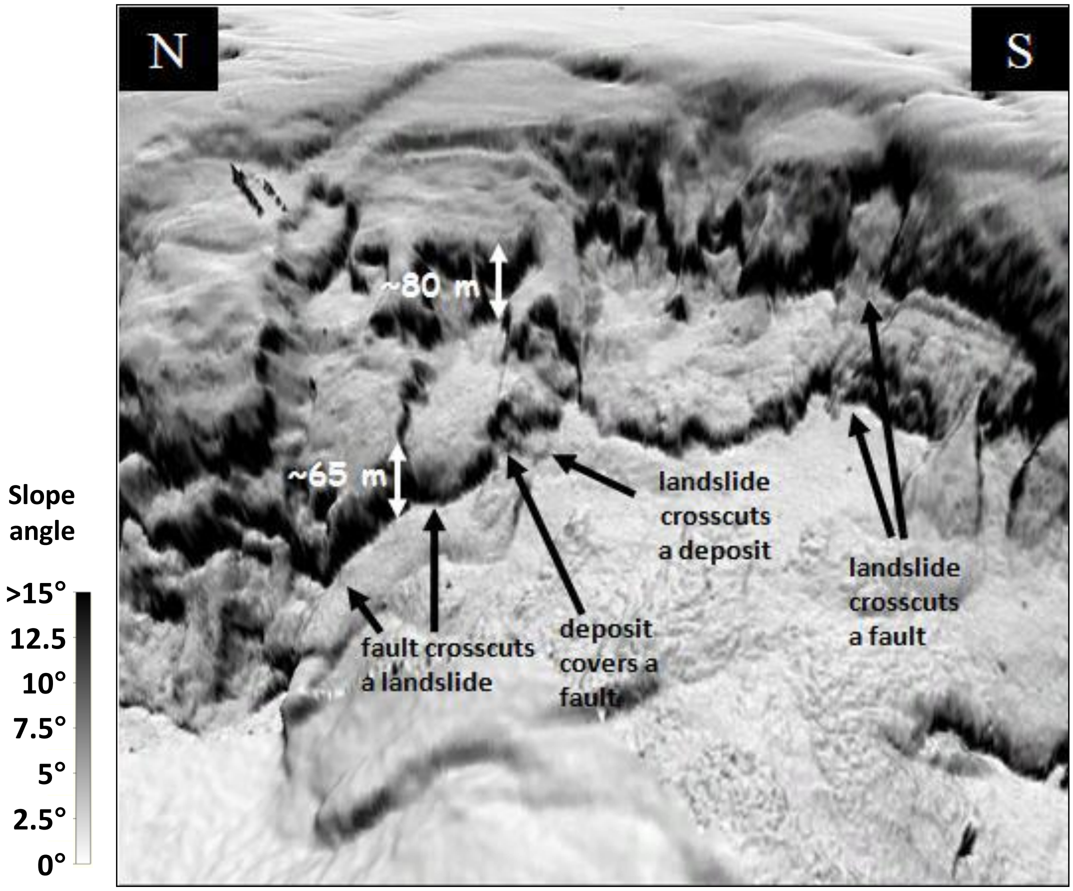

Figure 27: A perspective view showing the complicated cross cutting relations between landslides and faults in the studied area.

Outside of zone (b) landslides and faults do not coincide (Fig. 23): At the north of the studied area (zone a) only faults are observed; off Hadera to off Tel Aviv (zone c) the landslides appear on the continental slope and faults appear basinward; around Palmahim disturbance (zone d) there are only faults that constrain the disturbance, and one landslide basinward; and at the south of the mapping area (zone e) there are only landslides but no faults.

5.4. Messinian Isopach

The isopach map (Fig. 28) shows a gradual increase in Messinian salt thickness basinward: near the shoreline its thickness varies between 0 and 100 m sequence, increasing to up to 300 m under the foot of the continental slope; and up to 1600 m thickness at the westernmost mapping area, 80 km from the shore line. The largest gradient within the westwards salt thickness increase is between salt thickness of 100 m and 500 m. Overall isopach lines are coast parallel (Fig. 28). Two zones deviate from this trend, the Palmahim and the Dor disturbances (Fig. 28). There, hundred meters thick sequences of salt are located laterally near tens meters thick sequences (Fig. 28). The thick sequences are related to pre-Messinian topography (Garfunkel, 1984).

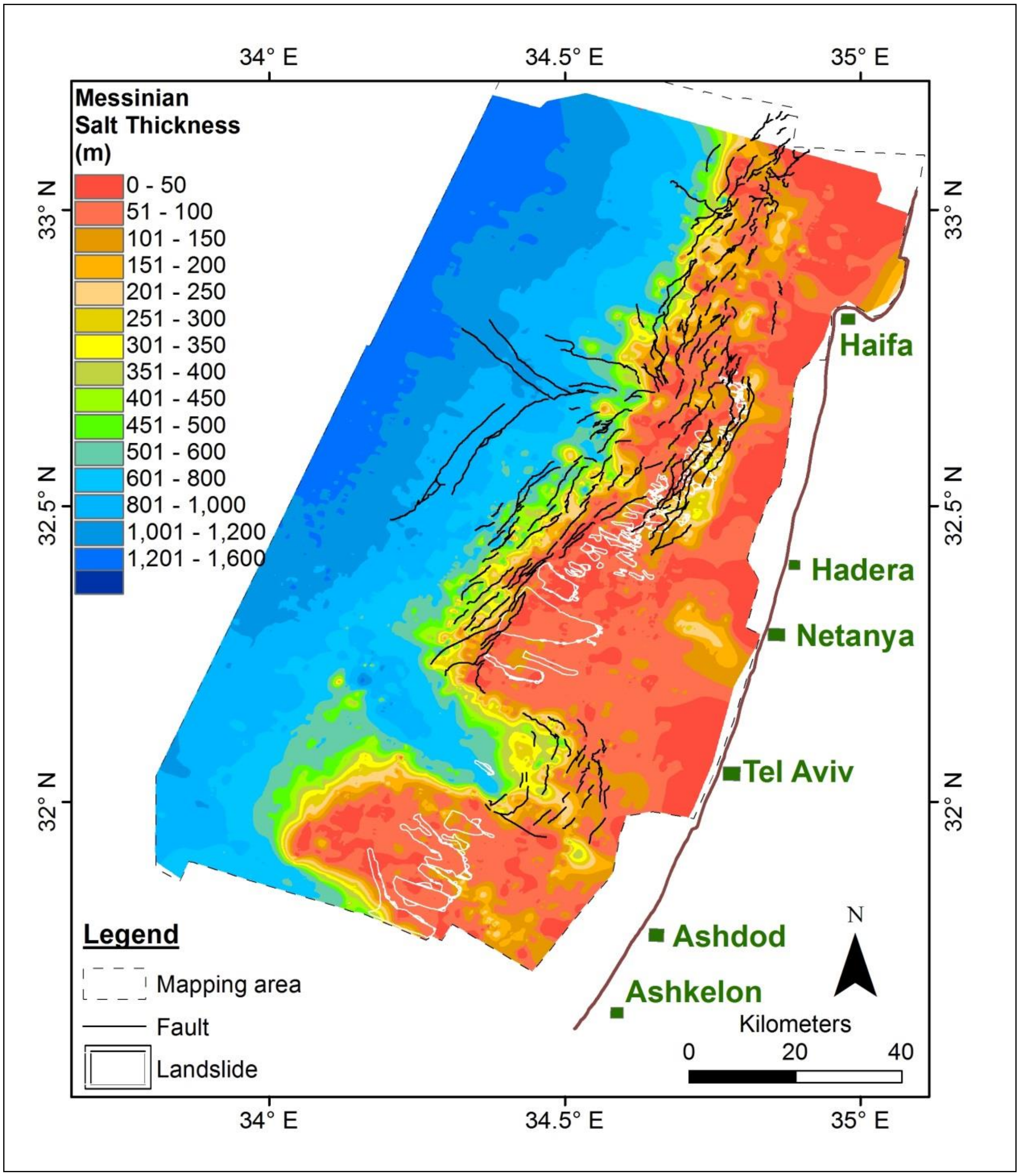

Figure 28: Landslides and faults shown on top of an isopach map of the Messinian salt.

5.4.1. Landslides and faults spatial distribution over the salt isopach

We analyze the spatial relations between the landslides and the fault scarps exposed on the sea floor and the Messinian evaporites buried more than a kilometer below (Figs. 28). Fig 28 shows that the faults mostly coincide with the edge of the salt layer, the region where salt thickness transitions from 0 near the shore to >400 m in the basin. A statistical calculation is made to determine the average salt thickness under each landslide and fault (Figs. 29 and 30). The results for landslides and faults are summarized in Figure 31. Landslides occur above various thicknesses of salt, from 0 to 450 m, most of them between 0 to 150 m thickness (Figs. 29 and 31). Faults are mapped above salt thickness of 0 to 1,200 m, many of them between 100 to 250 m thickness (Figs. 30 and 31). They have a noticeable trend, of coinciding with the 100- 200 m thickness isopach (Fig. 28). This trend is clear especially around Dor and Palmahim disturbances where the thick series of salt are found closer to the shore line (Fig 28). No coast-parallel faults are observed over salt sections thicker than 800 m. The meaning of these trends is discussed in the Discussion section.

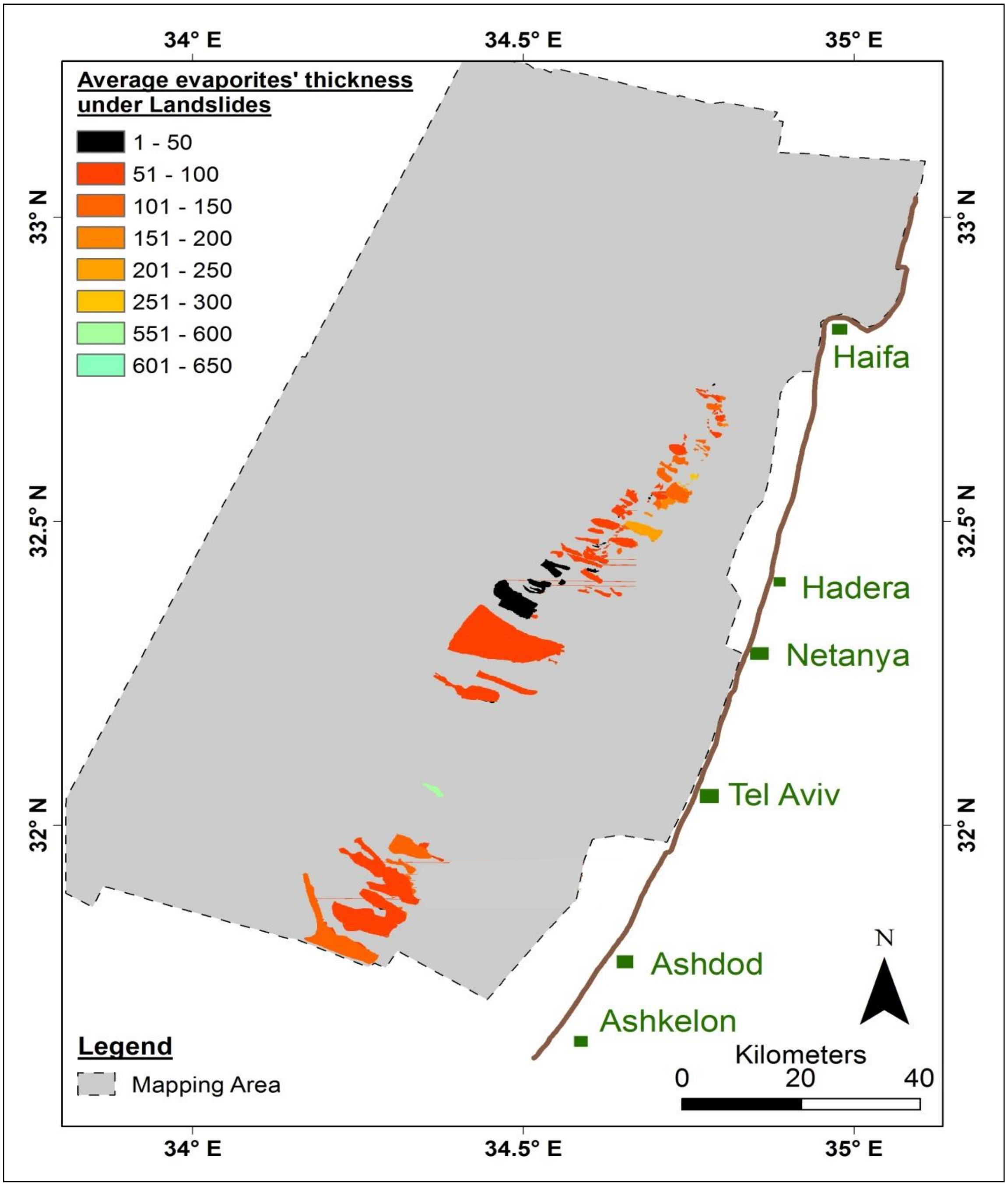

Figure 29: Average salt thickness under the landslides using pixel size of 80 m.

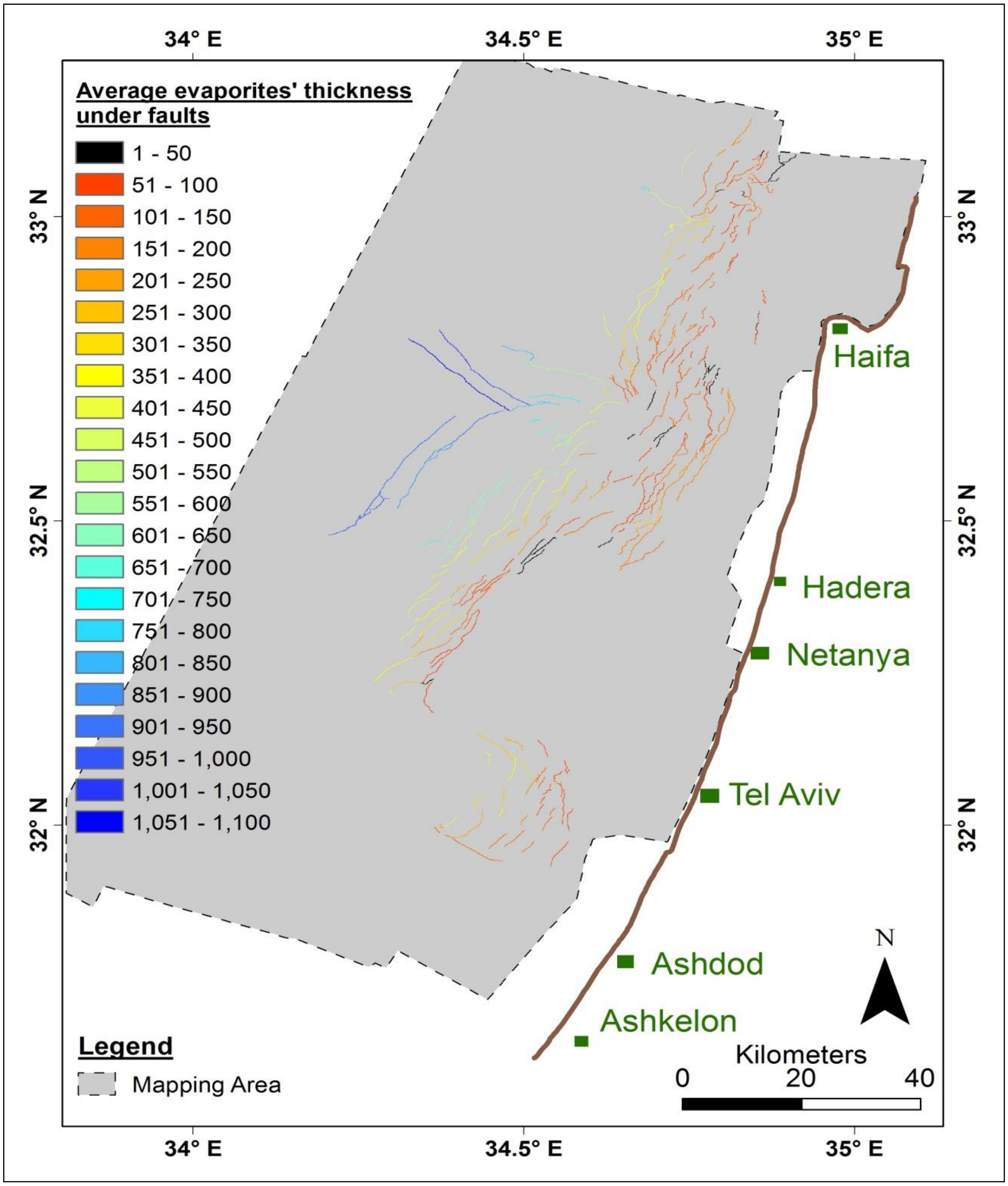

Figure 30: Average salt thickness under the faults using pixel size of 80 m.

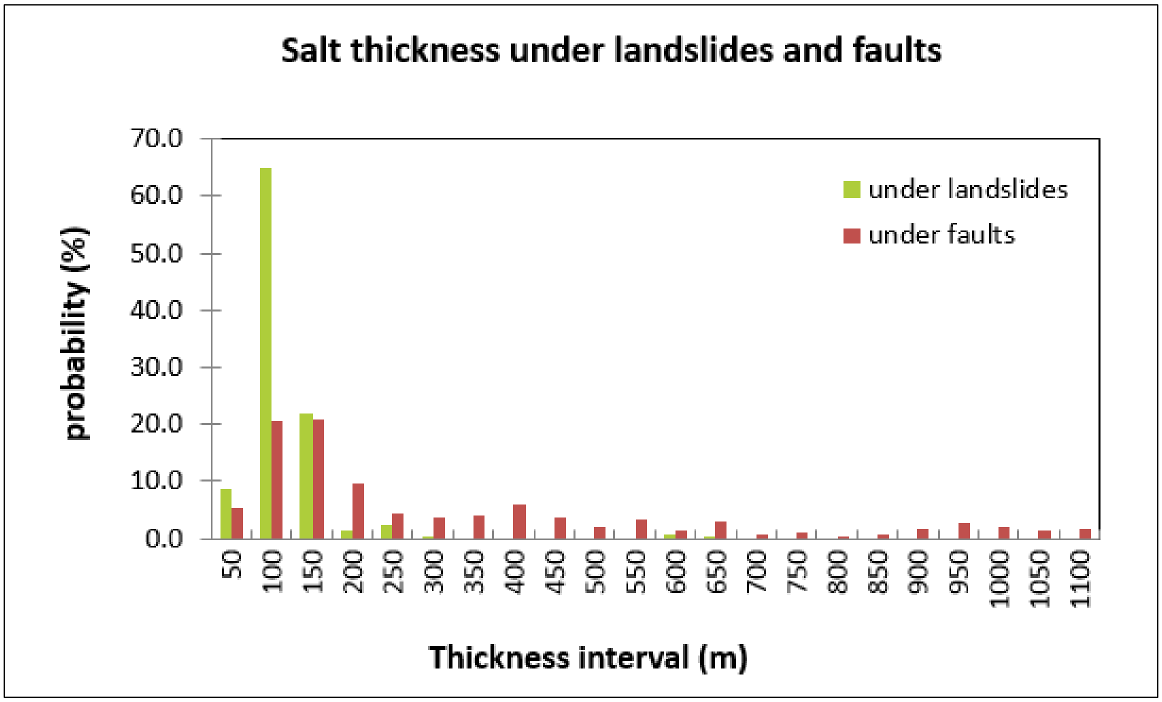

Figure 31: Probability for finding a given salt thickness under landslides and faults.

6. Discussion

Our mapping enables a broad view of the small - medium morphological structures, landslides and faults, that shape the continental shelf and slope off shore Israel. The new insight on the area enables the approval or rejection of the theories that were suggested before, as well as the suggestion of new ideas. In the discussion part we will discuss the mechanisms controlling the development of the studied morphological features. Additionally, we will discuss whether the formation of these structures is still active and what the possible implications of instability are.

6.1. Mechanisms and conditions for formation of landslides and faults

Landslides and faults do not spatially overlap across most of the studied area (Figs. 11, 12 and 23). The only site where they overlap is around Dor disturbance (Fig. 23). Therefore, we eliminate the possibility that one of them is the sole result of the other, as well as the option that the two phenomena were formed by the same mechanism. In continuation we discuss each mechanism separately, relying on our observations.

6.1.1. *Landslides geometry*

We want to better understand the landslides geometry and dimensions in order to assess their potential of occurrence and for geo-hazard estimation. Landslides appear as very shallow geomorphic structures in all our observations. Scars heights reach a maximum of 90 m (Figs. 10, 14 and Table S1 in supplementary data). Also seismic sections show that the landslides are superficial, with very low scars, that are sometimes hard to distinguish (Figs. 17 and 18). Another indication for the landslides thickness is the observed ratio between the landslide thickness (t) and its length (l). This ratio was observed by several authors to fall in the range of 0.02 – 0.15 for areal landslides (Whitehouse, 1983; Hovius et al., 1997; Stark and Guzzetti, 2009; Katz et al. 2014), regardless landslides' size, location and trigger. Here calculate t using the equation of Hovius et al. (1997) where ε (t/l ratio) for submarine landslides is taken as minimal, 0.05, since they tend to be larger and thinner than aerial ones (Hampton, 1996). Our most frequent landslide has the surface area of ~0.016 km^2 ($1.6*10^4$ m^2) thus, the calculated thickness of ~6 m. A reasonable estimation only when the failed material remains rather coherence during the sliding and doesn't totally lose its internal characters. When the failed material disintegrated and flows like mud, t/l ratio is not valid since the landslide is more similar to a flow and extends to a very large area.

6.1.2. *Landslides' mechanism: slope angle*

Unlike the faults, the landslides are located only at the upper most part of the section, apparently not directly affected by the Messinian salt (Figs. 17 and 18). It is also observed that their spatial distribution is not correlated with the salt thickness (Fig. 28). Although there is an apparent correlation between the landslides locations and salt thickness of 100 to 150 m (histogram in fig. 31), this connection is probably made coincidentally by the location of this salt thickness interval below the continental slope.

We now examine the correlation between the landslides scars' location and the nature of the continental slope. As described in the Introduction, the continental slope gradient decreases from north to south, from 35˚ at canyons province in the north to up to ~3˚ at the south of the mapping area (Figs. 2 and 6). Landslides' scars occur in a very narrow angle range of the continental slope, mostly between 3° to 5° (Fig. 23). We further explored this correlation by calculating the average slope angle in a strip of 250 m outside each landslide' scar (Fig.15). The slope angels that host most of the landslides scar areas are 3˚ to 6˚. Fewer scars are located at slope angles of 2˚ and slopes of 7˚ to 9˚ (Figs. 15 and 16). These data are in agreement with other data from different sites around the Mediterranean (Urgeles and Camerlenghi, 2013). Submarine slope instability at 5° or less are also known from many other sites around the globe (Masson et al., 2006 and references there in).

The sediment in the sea can maintain only moderate slopes in comparison to sediment on land (Masson et al., 2006). We examine a few typical angles within 44 selected landslides (Table 1) in order to check the characteristic angles of the submarine sediment, exposed in the scar and in the landslide deposit material. The slope angle at the head scarps ranges between 5°-26°, the deposited material that is close to the headscarp is laid in angles of 2° - 9°, while the deposited material at the toe, more basinward from the scar, is laid in angles of 1°- 3°, similar to those angles in Urgeles and Camerlenghi (2013). There is accordance between the angles of the original slope and the deposited material near the headscarps. Where landslides occur, the deposited material laid in the same angles of the original slope, indicating that the characters of the material dictate its maximum angle for long-term stability (the steepest angle of descent which the material can be piled without slumping) (Fig. 23). The lower angle of the material at the toe represents the angle of the disrupted material, possibly liquefied, which was deposited after its long downslope motion. This dynamic angle is lower than the maximum angle for long-term stability. The higher angles of the headscarps in comparison to the sediment's depositional angle are harder to explain. One possible explanation refers to a consolidation process. Unlike the sediment located on the sea floor, the buried sediment underwent compaction, consolidation and healing processes that probably increased its strength. Headscarps heights are up to 90 m, meaning they reveal sediments from deeper parts of the section. The higher slope angles of the headscarps in comparison to the sea floor slope angles are similar to laboratory rock-mechanical tests on slope material, where angles of internal friction were found to be 15° – 17° (based on consolidated-undrained triaxial compression tests for the Israeli continental slope, Almagor and Wiseman, 1982). Another possible explanation is that the headscarps are in quasi-stable position and they will pass a series of secondary failures (similar to the sequence appears in Figs. 13 and 14) eventually reaching the maximum angle for long-term stability (see also Katz et al., 2014, Figures 4a, b for snapshots from modeling of such a failure sequence). Similar mechanism, where an over-steepened landslide scar reaches stability at the maximum angle for long-term stability via a series of upslope retrogressive failures, was suggested analytically by Utili (2005) and numerically by Utili and Nova (2008).

We conclude that angle of slope approaching the angle of repose is a primary condition for the occurrence of slope failures. Triggers like earthquakes, elevated pore pressure, and fluid seeps can promote this process, as is further discussed below. Where landslides' scars initiate from faults it is reasonable to determine that the over steepening of the slope that was created by the faults made a trigger for the sliding of the material.

6.1.2.1. <u>A continuous process</u>

We use the cross cutting relations between the landslides and faults in order to understand the process of formation of ~450 landslide inventory. Faults in the studied area were observed to be syn-sedimentary and therefore indicate a long geological history. Since faults reveal complicated cross cutting relations with the landslides where they predate and postdate one another, it is reasonable to conclude that the landslides were also formed over long periods of time. This conclusion diminishes the possibility that the whole inventory was formed by a single triggering event like some other inventories in the world (Malamud et al., 2004; Guzzetti et al., 2002). Regarding that, it should be emphasized that while on land small landslides will be eroded in less than 10 years, the submarine erosion is much slower. Even though continuous sedimentation should be also taken into consideration as a factor erasing the submarine landslides, the sedimentation erases the landslides at rates of centimeters per hundreds of years (Hamman et al., 2008; Schilman et al., 2001), very slowly in comparison to erosion processes on land. Therefore, submarine historical inventories (which is the composition of old to recent landslides, as was defined in section 1.1.1.) may appear as event triggered since the erosion is minimal and old landslides almost don't disappear along the years.

6.1.2.2. Is a trigger involved?

After understanding that the critical condition for landslides formation is a minimal angle of the slope, we now discuss whether the process involves a trigger. We mentioned in the Introduction that triggers like earthquake or pore pressure increase can cause slope failures in situation of quasi stability of the slope (Hampton et al., 1996; Masson et al., 2006; Frydman & Talesnick ,1988; Haeussler et al., 2014; McAdoo et al., 2000). The strong seismic accelerations from earthquakes repeatedly imposes dynamic forces, that are added to the large downslope component of the gravitational force (Hampton et al., 1996). Active seismic zones known in the area are the Dead Sea Transfrom, the Carmel fault (Garfunkel et al., 1979) and faults in the Suez Rift area (Garfunkel, 1984). Although the option of earthquake triggering of the slope failures cannot be eliminated (Garfunkel, 1984), the importance of this process is not clear: Urgeles and Camerlenghi (2013) discuss the different landslides sizes in relation to the tectonic activity of the margins where they are located. In their work they examined almost 700 mass-transport deposits and almost 1000 failure scars in 9 different regions in the Mediterranean and the black sea. They suggest the idea that in active margins the deposited sediment has short residence time on the seafloor as it is mobilized in frequent but smaller landslides to the deep sea each time that an earthquake occurs. Conversely, on passive margins, large sedimentary accumulations tend to build up undisturbed, and when some minor perturbation occurs (e.g., relatively small earthquake), this sediment is mobilized in large landslides (Urgeles & Camerlenghi, 2013). Following their work, we can suggest for the Israeli margin the idea that the north part of the studied area is closer to the active seismic zone of northern Israel (Garfunkel et al., 1979; Garfunkel, 1984) and therefore have more frequent triggers, which cause smaller landslides in the north. In contrast, the south part of the studied area is more similar to a passive margin and therefore the sediments there form larger landslides. Other triggers that may cause sliding are over steepening of the slope as a result of faults formation or the sea level raising during deglaciation. A further discussion on the possible triggers appears below.

6.1.2.3. <u>Relative age of the landslides inventory</u>

We follow the statistical examination of several studies in order to compare and analyze our inventory's parameters to other aerial and submarine inventories; by that we want to learn about the characteristics of our inventory, especially regarding its relative age and whether it is still active. Malamud et al. (2004) studied three aerial inventories that are associated with a trigger, as well as 2 recent historical inventories of up to 25 years, and 2 other historical inventories from the last 10 k years. The event- triggered inventories are composed of landslides that were formed as a result of a known event and were mapped immediately following its occurrence. Their landslide areas distribute as an Inverse Gamma (Fig. 32, Equation 3), with the parameters shown in Table 2 (in this chapter). Their three inventories are considered complete inventories since they were mapped only a short time after they were formed and they fit the expected areas distributions trend line (Fig. 32) (Malamud et al., 2004).

<u>Equation 3 (Johnson and Kotz, 1970; Evans et al., 2000)</u>:

(3) $$p(A_L;\rho,a,s) = \frac{1}{a\Gamma(\rho)}\,[\frac{a}{A_L-s}]^{\rho+1}\ \exp[-\frac{a}{A_L-s}]$$

Where A_L is the area of landslide, the parameter ρ primarily controls the power-law decay for medium and large landslide areas, the parameter a primarily controls the location of the maximum probability distribution, the parameter s primarily controls the exponential decay for small landslide areas. Γ(ρ) is the gamma function of ρ (Malamud et al., 2005).

For large values of A_L, the Inverse-Gamma distribution given in Equation 3 can be approximated by <u>Equation 4 (Malamud et al., 2004)</u>:

(4) $$p(A_L) \approx \frac{1}{a\Gamma(\rho)}\,[\frac{a}{A_L}]^{\rho+1}$$

The tail of the probability distribution for large landslide areas is a power-law (a ‘fat-tailed’ distribution) with exponent −(ρ + 1) (Malamud et al., 2004).

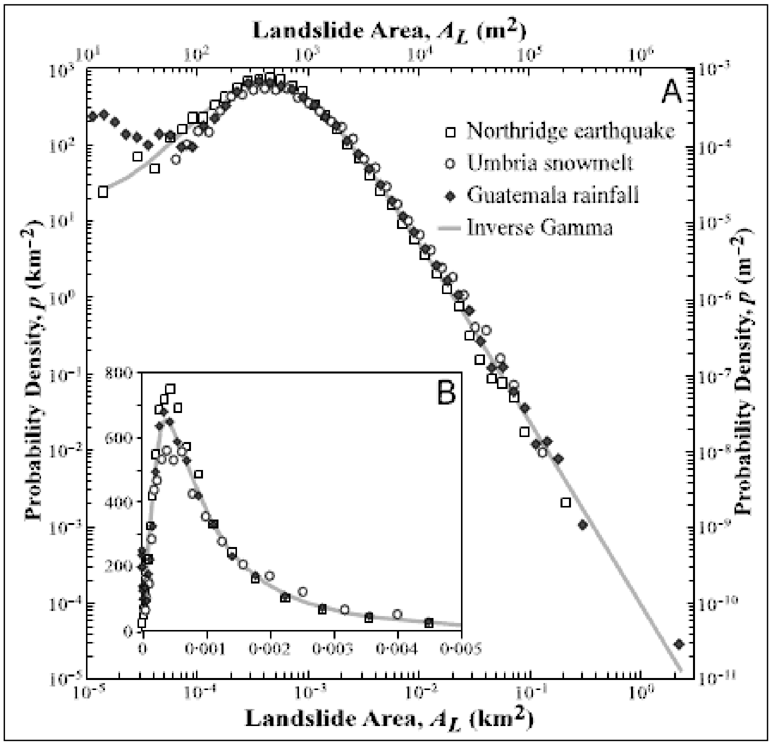

Figure 32: Landslide probability densities p as function of landslide area A_L, for three landslide inventories which are considered complete inventories (Malamud et al., 2004). Also included is the best fit three-parameter inverse-gamma distribution. The parameters of the distribution are shown in Table 2 at the discussion section.

According to Malamud et al. (2004) an inventory is complete if it distributes as an inverse gamma and contains the left tail of the distribution with the expected slope, expressing the existence of all the small scale landslides. Their assumption is that over time the small scale landslides are erased from the inventory because of erosion and other aerial activities, or their boundaries become indistinct and harder to identify. In that case the distribution will either lack its left tail (Fig. 5 in Malamud et al., 2004) or there will be less small landslides than expected for the large landslides' amplitude, thus the distribution will deviate from its expected shape (Fig. 6 in Malamud et al., 2004). Submarine landslides have a better preservation potential because they are exposed to less erosion than on land (Urgeles and Camerlenghi, 2013). Nevertheless, taking into consideration the sedimentation, the small landslides are expected to be erased over time also in submarine inventories, and therefore we consider Malamud's et al. (2004) theory valid for submarine inventories too. Malamud et al. (2004) suggest that using their function, every inventory can be checked regarding its completeness and in the case it's not, the small landslides can be restored from the function.

Our inventory, composed of the three generations of landslides together, distributes as an Inverse Gamma distribution (Fig 22 and Table 2). Referring only to one of the generations separately we get only a part of the Inverse Gamma distribution. The primary landslides' curve has only the right tail but lacks the rollover imposed by the small landslides (Fig. 21a). The secondary (Fig. 21b) and tertiary (Fig. 21c) landslides' curves have the rollover of the small and middle landslides, but lack the right tail of the large landslides. Only the three generations together construct the whole inventory. That means that the landslides are related to the same population, where the large landslides are primary landslides which are formed as a result of the external conditions and the small landslides are secondary and tertiary ones that are developed because of the large ones.

Guzzetti et al. (2002) studied two aerial landslides inventories: one was triggered by an event and one historical composed of very old, old and recent landslides. Like Malamud et al. (2004) they claim that every inventory, an event triggered or historical one, complete or lack the small landslides, distributes as a power law function in its right tail (middle and large landslides), within the range of sizes they checked (10^{-3} km^2 to 4 km^2). The difference is in the roll over: while in complete inventories the roll over is considered real, in incomplete inventories it is considered an artifact, because there is no a good record of the small landslides (Guzzetti et al., 2002). Guzzetti et al. (2002) present two inventories: Data Set B, which is considered complete, since it was mapped a short time after its occurrence and the area distribution of its landslides fits the expected trend line and; Data Set A, which is considered not complete and lack the small landslides (Fig. 33).

Urgeles and Camerlenghi (2013) represent data of submarine landslides. Their parameters are more relevant to us than the other works because submarine landslides differ from aerial ones in basic criteria such as sizes and erosion processes. Nevertheless, Urgeles and Camerlenghi (2013) examined significantly larger landslides than our landslides, spread on the whole Mediterranean (their landslides range from 10^2 km^2 to ~10^5 km^2 in comparison to our inventory: 10^{-3} km^2 to ~10^1 km^2). Thus, we won't compare their absolute landslides' sizes but only the parameters of the distribution.

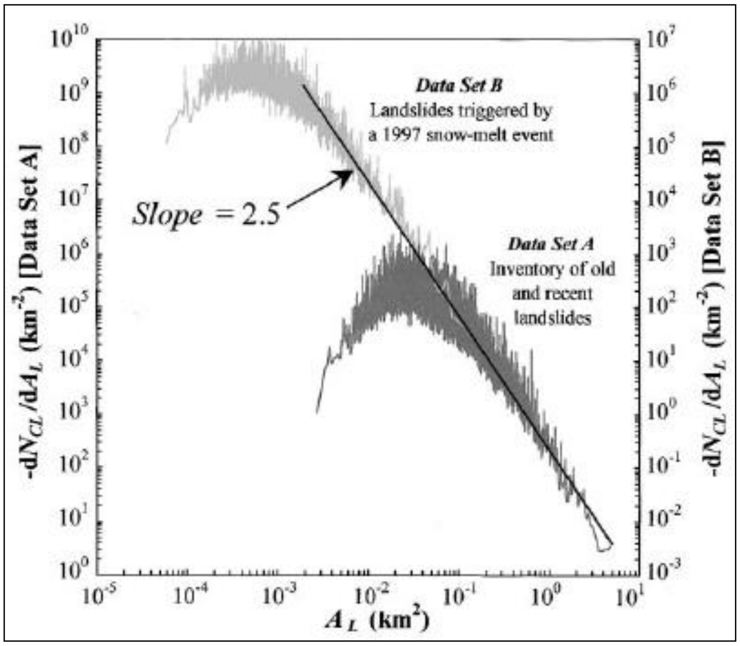

Figure 33: Landslides frequency-dN_{CL}/dA_L as a function of landslide area A_L for landslides at central Italy (Guzzetti et al., 2002).

An old and recent landslides inventory (Data set A, which is lack small landslides) and an inventory of landslides triggered by a rapid snow melting (Data set B, which is considered complete). The parameters of the distribution are shown in Table 2 at the discussion section.

Our whole inventory (composed of the three generations together) distributes as an Inverse Gamma function (Fig. 22 and Table 2), similarly to the complete inventories that we mentioned (Figs. 32, 33 and Table 2). Additionally, the parameters are comparable to the parameters expected for a submarine inventory, as it is explained below. These agreements are important in approving that our mapping was quite accurate, consistent and included at least the significant part of the landslides. This conclusion has a great importance concerning validation of our work and relaying on our mapping for further implications.

Another understanding from the comparison is regarding its relative age. Under the conditions of continuously sedimentation (an issue that is discussed in section 6.3.1.), the fact that the inventory includes the sufficient amount of small landslides for a complete inventory indicates that the inventory is relatively young and probably still active. This conclusion has an importance for future implications as it is discussed in the Conclusions section. In the Implications to geo-hazard (section 6.3) we use sedimentation rates to estimate the inventory's age. In Table 2 we compare the parameters of our whole inventory distribution with those of previous works.

Table 2: Comparison of statistical parameters between our landslide's inventory and other inventories in the world.

Variable description	This work	Urgeles and Camerlenghi (2013)	Guzzetti et al. (2002)		Malamud et al. (2004)
	Submarine	Submarine	Subaerial		Subaerial
Max landslide area	91.4 km^2	~131,000 km^2	4 km^2		Three inventories: 0.259 km^2 0.156 km^2 3.87 km^2
Range	$2.4*10^{-3}$ km^2 to 91.4 km^2	230 km^2 to ~131,000 km^2	Data set A (historical): $3*10^{-2}$ km^2 to 4 km^2 Data set B (triggered): 10^{-3} km^2 to 0.1 km^2		-
Mean landslide area	~1 $\mathbf{km^2}$	(Median): 19.1 km^2	Data set B (Average): ~0.1 km^2		Three inventories (respectively): 2.14 $x10^{-3}$ km^2 3.01 $x10^{-3}$ km^2 3.07 $x10^{-3}$ km^2
Power-law decay exponent for medium and large values in the distribution. called α in equ. (2) and ρ in equ. (3)	**0.67**	**0.8**	Data set A (historical) **1.5**	Data set B (triggered) **1.5**	**1.4**
The parameter primarily controls the location of the maximum probability distribution. called λ^2 in equ. (2) and a in equ. (3)	**~ $3.3*10^{-2}$km^2**	-	Data set A (historical): **$2*10^{-2}$ km^2**	Data set B (triggered): **$6*10^{-4}$ km^2**	**$1.28*10^{-3}$km^2**
Exponential rollover for small values in the distribution. called $-(\eta^2)$ in equ. (2) and s in equ. (3)	**$-3.58*10^{-3}$km^2**	-	-	-	**$-1.32*10^{-4}$km^2**

A few differences are observed when comparing our size distribution statistics with the one of the subaerial inventories (Malamud et al., 2004; Guzzetti et al., 2002). First, the landslide areas are significantly larger in our inventory (range, mean and max landslides area in Table 2). Second, the power law decay, which expresses the frequency of the large landslides in relation to the medium landslides is less steep in our inventory – $-(\rho+1) = (-1.67)$ than in the subaerial inventories $-(\rho+1) = (-2.4)$ or (-2.5). The other submarine inventory (Urgeles and Camerlenghi, 2013) shows close parameter to ours $-(\rho+1) = (-1.8)$) (Table 2). The difference in power laws between areal and subareal slides, indicates that in submarine inventories there are more large-sized landslides relative to medium ones in comparison to subaerial inventories. It is important to keep in mind that we discuss landslides sizes in terms of areas, and there may not be a difference in landslides' volumes. In other words, the difference in landslides sizes and power law decay between submarine and subareal inventories may indicate different physical processes of flow and deposition, rather than a difference in the amount of displaced material. In that case the volume distribution, it is expected to be similar for submarine and subareal inventories. A larger deposition area underwater is indeed expected since in the sea the transformation of the original mass from the failure location downslope involves fragmentation, reduction in friction during the sliding, possibly pore pressure increase and other processes that significantly reduce the strength of the soil mass to remolded shear (Locat & Lee, 2000 and references there in). As a result, the failed material can spread over larger areas and result in landslides with larger surface area. In several cases, this mass may show flow structures characteristic of debris flow processes (Masson, 2006), a phenomena that also increases the landslides' area sizes in submarine inventories.

6.1.2.4. A power law size distribution: optional models

A few authors tried to explain why medium and large landslides consistently satisfy power-law (fractal) frequency-area statistics (Guzzetti et al., 2002 and references there in; Katz & Aharonov, 2006). Two approaches were taken: one is a statistical method, explaining the landslides' size distribution by the model of Self Organized Critically (SOC), and the other one is a mechanical explanation. We review the two approaches here.

Bak et al. (1987), numerically modeled a sand-pile using a constant input of grains from above, in order to explain the power law distribution of landslides. Using simple system stability rules for slope failure the output of numerical grains was observed to occur in an avalanche style failure with a power law frequency magnitude relation. This spontaneous emergence of power law avalanche sizes in a homogeneous system was termed by Bak et al. (1987), as self organized criticality (SOC). However, A simple explanation invoking sandpile model was not sufficient because noncumulative power-law exponent for subareal landslides is $\beta = 2.5 \pm 0.5$ (Equation 5) whereas the noncumulative power-law exponent for the sandpile model avalanches is $\beta \sim 1.0$ (Guzzetti et al., 2002).

Equation 5 (Guzzetti et al., 2002):

(5) $$N_E = C' A_E^{-\beta}$$

where N_E is the (noncumulative) number of slip events with area A_E, the number of blocks that participate in the event, and C' and β are constants. One idea was to explain that difference by combining slope stability analysis with self-affine topography and soil-moisture content, which gave a power-law noncumulative frequency-area distribution with $\beta = 2.6$ (Equation 5, Pelletier et al., 1997). Another attempt was to use a numerical model combining slope stability and mass movement (Hergarten and Neugebauer, 1998), which gave an exponent of $\beta \sim 2.1$ (Equation 5, Guzzetti et al., 2002). However, there is a real question if these models are realistic in terms of governing physics (Guzzetti et al., 2002). In addition, these models don’t predict a rollover as observed in nature.

Katz and Aharonov (2006) ruled out the SOC model for explanation of power law distribution in landslides, not only because these models fail to reproduce the slope of the observed power law, but also because models that produce power law distributions (cellular-automaton, forest-fires, spring-blocks) use stability rules that are physically inconsistent with processes occurring in natural slope failures. In other words, since we observed connection between different properties of landslides, such as thickness, area and volume (Whitehouse, 1983; Hovius et al., 1997; Stark and Guzzetti, 2009; Katz et al. 2014), we cannot treat their sizes distribution merely as statistically determined, but have to consider physical mechanism to explain our observations (Katz and Aharonov, 2006). The mechanism proposed by Katz and Aharonov (2006), distinguishes between two parts of the size distribution. The first is the roll-over, which represents the small landslides with characteristic size. These landslides are formed at the homogenous unconsolidated environment that is formed at the upper part of the section. There, the thickness of the landslides is limited to the thickness of the homogenous environment, and as a result the area of the landslides is limited as well. The second part is power law part of the distribution that represents the large landslides. These landslides are formed at the rock mass below the unconsolidated sediment, a heterogenic environment due to bedding, layers and fractures located within it. The nature of the landslide size distribution is controlled by the heterogeneity. The heterogeneity in nature arises due to pre-existing fractures, variable water content, variability in material properties and the natural variability in mechanical properties of sedimentary sequences (Katz and Aharonov, 2006), and due to variable topography (Frattini and Crosta, 2013). Since we consider landslides as mechanical structures, we tend to accept the mechanical model as a better explanation for their size distribution. Thus the most frequent landslide thickness has a mechanical meaning. Possibly below this depth the sediments are stronger because of more compaction and therefore they require stronger triggering in order to fail.

The suggested mechanism is one example for the formation of this distribution, and other models can be acceptable too. This question can be further referred to in future research.

We showed before that our landslides' inventory has been created over a long period of time, as it is composed of several phases of failures and the landslides have complicated cross cutting relations with the syn-sedimentary faults. Its sizes distribution, of an Inverse Gamma can be either controlled by events like earthquakes that took place over the years, or be a result of a continuous long process of failures only as a result of the slope angle. Since the failures are determined by the pre-existing conditions of instability, we cannot determine from the distribution whether a trigger was involved in the process, a question that will remain for further research.

6.1.2.5. Landslides' mechanism summary

From the information we observed and discussed until now, we demonstrated that the slope angle is the most significant factor influencing the landslides location. Our landslides' inventory shown to have formed over a long period of time and not after a single event, although it is possible that triggers such as earthquakes or elevation of pore pressure were also involved in the process. We suggest to explain the size distribution of the landslides by a mechanical model and not by a statistical model. The inventory is a complete inventory as the size distribution of its landslides is in agreement with other complete inventories in the world, meaning it is probably still active. Another evidence for the continued activity are the cross cutting relations of the landslides with the syn-sedimentary still active faults. Thus, we determine that the mechanism of the landslides' formation is still active and the area is not stable and is likely to pass further slope failures in the future.

6.1.3. Faults mechanism

Faults are observed in the bathymetry map as elongated structures, rupturing the sea floor, and in the seismic sections as syn-sedimentary faults displacing the Plio-Quarternary sediments. In this section we will discuss the controlling factors on faulting and suggest a mechanism determining their spatial distribution.

Unlike landslides, which correspond to certain slope angles (Fig 23), the faults occur over various slope angles: rupturing the shelf edge, the continental slope, and further basinward (Fig. 23). In addition, faults are observed at various water depths, from ~100 m to ~1600 m (Fig. 12). Thus, faulting mechanism seems not to be controlled by any superficial factor. From previous works we learn that these faults are not interpreted as tectonic faults either, as they have no deep roots (Almagor and Garfunkel, 1979; Gradman et al., 2005; Gvirzman et al., 2015).

6.1.3.1. A salt tectonics process

Similar to Garfunkel and Almagor (1984), we observe that the faults are thin-skinned features, rooted at the Messinian evaporites (Figs. 25 and 26) or at the disturbed sediments above it (Figs. 26 eastern part). The faults are correlated with a minimal salt thickness of less than 100 m (Fig. 28), and thus the faults are formed in a salt tectonics process. In the salt layer we observe salt rollers (similar to Gradmann et al., 2005) (Figs.

25 and 26 eastern part). Above these rollers at the basinal part of the seiemic sections we observe that the sediments are folded, expressed on the sea floor as wavy patterns, or they are thrust faulted, expressed on the sea floor as eastward tilted steps (Fig. 26 western part). We interpret our observations following the salt tectonics process that was detailed in the Introduction section. The sliding of the sediments basinward on top of the salt result in formation of an extensional zone at the upper part of the continental shelf and slope, expressed by normal faults. Basinward, there is a compressional region, where the thick salt sections make pressure-induced plastic structures such as rollers. The sedimentary overburden above these deformations passes compression too, as the sediments of the slope are pressed at the sediments of the deeper parts of the basin. This is expressed by folds and thrust faults which influence also the bathymetry.

We observe that the faults are correlated to Messinian evaporites' minimal thickness of less than 100 m (Fig. 28, 31). The agreement between the faults and <100m thickness of the Messinian salt may indicate that the presence of a minimal thickness of salt in the section is a primary factor in the mechanism of the faults, as it is discussed in continuation.

6.1.3.2. Faults formation mechanism

Two possible mechanisms can explain the observed phenomena:

The first mechanism is active salt flow (Gvirzman et al., 2015 and references therein). The thick sequences, of up to 2 km of sedimentary overburden, overlying hundreds of meters of salt rocks (Almagor & Garfunkel, 1979; Garfunkel & Almagor, 1984), provide the potential to instability (Ginzburg et al., 1975; Garfunkel, 1984). The proximity to the continental slope and shelf initiates motion (Humphris, 1978; Martin; 1978 both in: Gradmann et al., 2005) due to either gravity on a slope (Garfunkel, 1984) or differential loading (Hudec & Jackson, 2007). The salt flows basinward, as the overburden promotes its movement, gradually sliding toward the basin. The removal of the salt from parts of the section was also mentioned before (Gradmann et al., 2005 and references there in) and is further discussed below.

From our observation that the faults are rooted in or above the deformations of the salt (Figs. 25 and 26) we conclude that the salt and the overlying sedimentary are mechanically coupled. That means that the salt "drags" the sediments with it basinward.

According to that we find unreasonable the claim that over thin sections of salt, the salt acts as a lubricant, making the sediments above it slide basinward (Hudec & Jackson, 2007). Considering the salt role in the proposed mechanism of faults formation, it is understood why a critical minimum thickness of salt is needed in order to create the process (Garfunkel, 1984). Very thin salt section may not act plastically under the pressure of the overburden. Another option is that the process will start normally, but will be stopped shortly afterwards because of lack of salt.

The correlation of the faults with the minimal salt thickness can be differently explained. The salt thickness may not be a factor in the process, but a result of the process. The suggestion is that the salt was originally deposited further east than its current location. With time and progression of the process, it was squeezed out and changed its thickness, pushed by the sediments from under the shelf and slope-basinward. That can explain the presence of faults above places with minimal or no salt thickness under them, a phenomena that is observed both in seismic sections (Figs. 17, 25 and 26) and in isopach map (Fig. 28: faults over 0- 50 m thickness). The interpretation should then be different: faults are observed over a minimal salt thickness not because this is the critical thickness needed to create faults, but because the process of faults formation is accompanied by the thinning of the salt due to its ejection out basinward.

The second mechanism proposes that the removal of the salt from the subsurface creates a depletion of material from the section and therefore causes instabilities and faulting. Similar process was described in the formation of sinkholes near the Dead Sea (Abelson et al., 2003). There, the dissolution of a buried salt layer by fresh groundwater due to the drop of the Dead Sea and the associated groundwater levels causes gradual land subsidence and the formation of young fault systems (Abelson et al., 2003). Other processes that exhibit similar mechanism deal with the depletion of other materials rather than salt. One example is a study on a collapse of caldera after magma is extracted (Acocella, 2007). A model of sediments and silicon exhibits the phenomena, that after the fluid is extracted from the subsurface, the missing matter induces compaction and related faults in overlying layers (Acocella, 2007). Another analogue is from gas and oil fields. Extraction of the hydrocarbon from a reservoir in the subsurface creates compaction in overlying layers and normal faulting (Segall and Fitzgerald, 1998). In our studied area, without the mechanical support of the salt, the sediments directly above it fail in the form of faults. Hudec and Jackson (2007) explain the lack of salt by a combination of creep flow and dissolution, a process that causes the top and bottom contacts of the salt to merge, forming a salt weld. Since the failure happens above places where the salt was removed, we observe the faulting above the edge of the depleting layer, where it pinches out, there the depletion is maximal. Similar process is depicted by Segall and Fitzgerald (1998): when the depleted reservoir is located in an extensional environment, normal faults develop on the flanks of the field as a result of fluid withdrawal from its center (Fig. 34). Garfunkel (1984) explains that having the sediment already in the state of gravitational instability or very close to that state, faults activity will trigger basinward sliding, thus the faults will be normal, tilted toward the basin. According to that mechanism, a minimal salt thickness is correlated with the faults location, because this certain thickness is the pinch out, the edge of the salt layer. With time and progressing of the process, the salt movement basinward causes the migration of the pinch out toward the basin. Then new depletion zone, which will be located more basinward, will create new faults above it. Thus, we expect to find that the faults become younger as we move basinward. The proposed mechanism can explain the occurrence of faults above sections with no salt under them, a phenomena that is observed both in seismic sections (Figs. 17, 26 and 27) and in isopach map (Fig. 28: faults over 0- 50 m thickness). In the past these sediments were located above the edge of the salt layer, what caused their faulting. Later the salt migrated from there basinward.

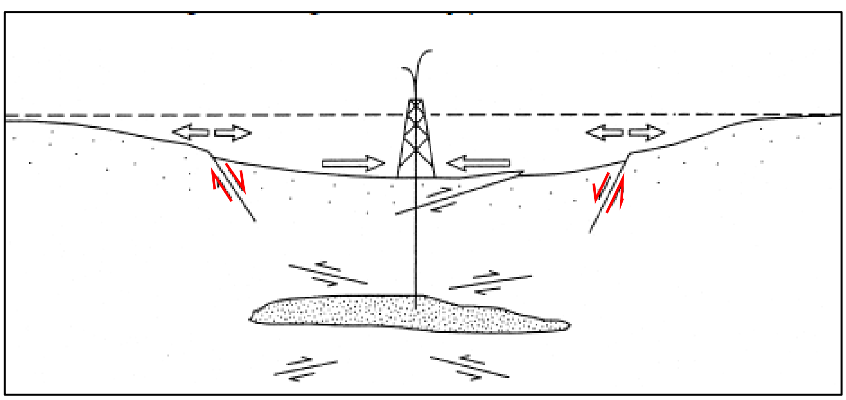

Figure 34: Summary of observed faulting associated with fluid withdrawal from a hydrocarbon reservoir (Segall and Fitzgerald, 1998). Open arrows indicate horizontal strain. Normal faults develop on the edges of the field as a result of fluid withdrawal from its center.

We believe that the two proposed mechanisms function together, where the salt flows basinward as a result of the gravitation and overburden pressure, causing instabilities in the sediments above it as a result of the reduction of the mechanical support under the.

Our ideas can be examined in a future research and modeling. Since we know the thickness of the sedimentary overburden and the salt and can check the physical properties of both these rocks, we can produce the process in both real and theoretical models. By that we can examine its progress and properties, such as flowage velocity of the salt, formation of the faults, including their formation order and rates and the influence of different inclination and overburden thickness. We can get additional data from dating the faults in the seismic sections. By that we can examine whether they are indeed progressing basinward as expected.

6.2. Implication to geo-hazard

6.2.1. Dating

Much work has been attempted around the world to constrain the time of occurrence of submarine landslides (Lee, 2009 and reference there in; Urlaub et al., 2013), either directly estimated using the numerical age of the pre or post sliding sediments (Normark et al., 2004) or by using the thickness of the post sliding sediment and the estimated sedimentation rates (Prior et al., 1986).

The timing of the studied landslides, and the question whether they are still active are important questions. This section provides a first estimate for a general age constraint, using the relief of the small submarine landslides in the studied area and the local sedimentation rates. The thickness (t) of a landslide with a mapped area (A) of less than 0.1 km^2 (242 such landslides were mapped, Fig. 11) is expected to be ~15 m ($t = \varepsilon \times \sqrt{A}$, where $\varepsilon = 0.05 \pm 0.02$ on land; Hovius et al., 1997). Mechanical constraints on the geometry of landslides do not allow the head scar to exceed significantly this thickness. Sedimentation rates calculated for the studied area are evaluated to range between a few tens centimeters per 1000 years (e.g. Hamman et al., 2008) and up to a meter per 1000 years (Schilman et al., 2001). Using sedimentation rates of between 0.5 m and 1 meter per 1000 years, we calculate that a scar relief of 15 meters will be half filled by sedimentation in ~7,000 years for high sedimentation rates to ~14,000 years for low sedimentation rates, at which point we won't be able to resolve it anymore with our current vertical resolution. Thus, we suggest that the small to medium landslides mapped in the studied area are less than 14,000 years old assuming the slowest sedimentation rates, and are constrained to be younger than 7,000 years old if we assume sedimentation occurs rapidly at 1 m per 1000 years. These ages constraint also overlaps with landslide age estimates presented in Camerlenghi et al. (2010), who conclude that the vast majority of the landslides in the Mediterranean continental margins have occurred between 20 and 10 ka b.p. and therefore they coincidence very well with the last major global climatic change, corresponding to the deglaciation following the last glacial maximum.

In this framework, it should be noted that the sedimentation regime is changed during the last 60 years since the Nile River stopped being the main source to the sediments of the slope and shelf off Israel (Almogi-Labin et al., 2012). This change started after the building of several dams on the river, the last one of which is the Aswan dam. The dams stop almost completely fine sediments derived from Ethiopia source from entering the Mediterranean through the Nile. The drastic reduction of the sediment supply causes rapid and continuous withdrawal of the Nile delta, which is the main source of sediments in our area today (Zviely et al., 2007 and references there in). Nevertheless, this change has no expression in our data, since it took place only recently. The building of the Aswan Dam forced the currents to take sand from the Nile Delta coast, and led to significant erosion in this area (Zviely et al., 2007). The sand taken from the Delta coast, however, has compensated for the reduction of Nile River sand and prevented sand shortages further up the Nile littoral cell coastline (Zviely et al., 2007). The reduction is expected to ultimately affect the Israeli coast only within approximately 400 years (Rohrlich and Goldsmith, 1984). Nevertheless, it should be taken into consideration in future forecasts, as detailed in the Conclusions section.

7. Conclusions and prognosis to the future

In this work we mapped and studied the small and medium features which morphologically form the bathymetry, in order to determine the mechanism controlling them and conclude about the current and future stability of the sea floor. We first mapped on the bathymetry all the landslides and faults in the study area. We examined their properties, spatial distribution and cross cutting relations. For the landslides we used statistical tools in order to compare them to other inventories. In addition, we observed both landslides and faults in seismic sections and examined their spatial distribution on top of a map of the Messinian evaporites thickness.

From all our observations and calculations we conclude that faults and landslides are created and controlled by different mechanisms. In the studied area, landslides are developed over a critical slope angle. It seems that the whole landslides inventory has been formed over a long continuous process, and therefore it fits the definition of historical inventory. Faults in the studied area are formed in a salt tectonics process, where the salt and overlying sedimentary sequence gradually slide basinward. The salt seems to be active in the process. The faults are formed probably during the depletion of the salt from the underground, possibly as a result of the weakening of the mechanical support under them. Landslides and faults seem to be contemporaneous and their mechanisms of formations are probably still active.

It is still not clear whether the landsliding took place following triggers, like earthquakes (Almagor and Wiseman, 1977, 1982; Frydman and Talesnick, 1988) or changes in sea level, or occurred only as a result of the continuous sedimentation and creation of critical slope angles on the slope. Both the landslides and faults formation mechanisms are not totally clear yet.

Considering the instability of the continental shelf and slope, it seems that placing gas lines and other infrastructure on the seafloor is currently quite problematic. It is hard to find a path from the basin to the shore line on the continental slope that is not disturbed either by landslides or by faults.

It is likely that the significant reduction in sedimentation rates due to the dams that were built on the Nile River will reduce the formation of the landslides in the future. The places that are currently instable may fail, but new instability as a result of further sedimentation will decline. On the other hand, the coverage of the landslides will be also reduced significantly and the seafloor will stay in a similar form. This is a process that is expected to begin only when the delta of the Nile stops supplying sediments to our region, and until then the process is expected to continue.

Regarding the faults, we expect that the process will continue without a change despite the change in sedimentation, because their formation is dependent on relatively deep processes which are attributed from the salt. Nevertheless, since the sedimentary overburden is one of the main factors in the process, the reduction in sedimentation may reduce the rate of the faults formation.

Our work may and should be taken as a case study for the instability of the continental slope and shelf around the Mediterranean. Most of the mapping works which were made in the Mediterranean, and in other locations around the world (e.g. Camerlenghi et al., 2010; Hu¨hnerbach & Masson, 2004; Masson et al., 2006) studied large scale structures. Our study enables a new and better comprehension about the stability question of the region, considering the small scale structures. Our conclusions should be taken into consideration also regarding tsunami hazard, associated with the occurrence of submarine slope failures in the Mediterranean, whose vulnerability is extremely high due to the large coastal population. Further studies on similar regions around the Mediterranean, as well as additional study of our region will shed more light on the processes that shape the continental slope and shelf and on the instability of these regions.

8. Acknowledgements

Ministry of Science and Technology, Israel

Neev Center for geoinformatics in the Hebrew University institute

Zohar Gvirtsman, Yonatan Elfassi

9. References

Abelson, M., Baer, G., Shtivelman, V., Wachs, D., Raz, E., Crouvi, O. and Yechieli, Y. ,2003. Collapse sinkholes and radar interferometry reveal neotectonics concealed within the Dead Sea basin. *Geophysical Research Letters*, v. 30, p. 1-52.

Acocella, V., 2007. Understanding caldera structure and development: An overview of analogue models compared to natural calderas. Earth-Science Reviews v. 85, p. 125–160.

Almagor, G., 1980. Halokinetic Deep-Seated Slumping on the Mediterranean Slope of Northern Sinai and Southern Israel, *Marine Geotechnology*, v. 4, No. 1, p. 83-105.

Almagor, G., 1984. Salt-controlled slumping on the Mediterranean slope of central Israel, *Marine Geophysical Researches* v. 6, p. 227-243.

Almagor, G. and Garfunkel, Z., 1979, Submarine slumping on the continental margin of Israel and northern Sinai, *AAPG Bulletin*. v.63, p. 324-340.

Almagor, G. and Hall, J.K., 1980. Morphology of the continental margin of northern Israel and southern Lebanon *Isr. J. Earth-Sci.*, v. 29, p. 245–259.

Almagor, G., Hall, J.K., 1983. Morphology of the continental margin off north-central Israel. *Israel Journal of Earth Sciences* v. 32, p. 75–82.

Almagor, G. and Wiseman, G., 1977. Analysis of submarine slumping in the continental slope off southern Israel. *Mar. Geotechnol.*, v. 2, p. 349-388.

Almagor, G. and Wiseman, G., 1982. Submarine Slumping and Mass Movements on the Continental Slope of Israel. Marine Slides and Other Mass Movements, *NATO Conference Series*, v. 6, p. 95-128.

Almogi-Labin, A., Calvo, R., R., Elyashiv, H., Amit, R., Harlavan, Y. and Herut, B., 2012. Sediment Characterization of the Israeli Mediterranean Shelf (10-100 m). *Report GSI/27/2012*.

Bak, P., Tang, C. and Wiesenfeld, K., 1987. Self organized criticality: an explanation of 1/f noise, *Physical Review Letters* v. 59, p. 381–384 *in*: Katz, O. and Aharonov, E., 2006. Landslides in vibrating sand box: What controls types of slope failure and frequency magnitude relations? *Earth and Planetary Science Letters*, v. 247, p. 280–294.

Baudon, C. and Cartwright, J., 2008. Early stage evolution of growth faults: 3D seismic insights from the Levant Basin, Eastern Mediterranean, *Journal of Structural Geology* v. 30, p. 888–898

Berndt, C., Costa, S., Canals, M., Camerlenghi, A., De Mol, B., Saunders, M., 2012. Repeated slope failure linked to fluid migration: The Ana submarine landslide complex, Eivissa Channel, Western Mediterranean Sea, *Earth and Planetary Science Letters* 319–320, p. 65–74.

Birkeland, P.W., 1999. Soils and Geomorphology, *Oxford University Press*, 430 p.

Bünz, S., Mienert, J., Bryn, P., Berg, K., 2005. Fluid flow impact on slope failure from 3D seismic data: a case study in the Storegga Slide. *Basin Res.* v. 17, p. 109 – 122. doi:10.1111/j.1365-2117.2005.00256.x

Camerlenghi, A., Urgeles, R., and Fantoni, L., 2010. A Database on Submarine Landslides of the Mediterranean Sea. *Submarine Mass Movements and Their Consequences, Advances in Natural and Technological Hazards Research*. *Springer Science and Business Media B.V*. v. 28 p. 503 – 513.

Cartwright, J.A., Jackson, M.P.A., 2008. Initiation of gravitational collapse of an evaporite basin margin: the Messinian saline giant, Levant Basin, eastern Mediterranean. *Geological Society of America Bulletin* v. 120, p. 399–413.

Carlson, P. R., Holocene slump on continental shelf off Malaspina Glacier, Gulf of Alaska. *AAPG Bull*. v. 62, p. 2412- 2426, 1978 *in*: Hampton, M.A., Lee, H.J. and Locat, J., 1996, Submarine landslides. *Reviews of Geophysics*. v. 34, p. 33–59.

Cazes, C. A., 2004. Overlap zones, growth faults and sedimentation: using high resolution gravity data, Livingston parish, LA. A Thesis Submitted to the Graduate Faculty of the Louisiana State University and Agricultural and Mechanical College in partial fulfillment of the requirements for the degree of Master of Science.

Crandell, D. R., Miller, C. D., Christiansen, R. L., Glicken, H. X. and Newhall C. G., 1984. Catastrophic debris avalanche from an ancestral Mount Shasta volcano, California, Geology of the Upper Cretaceous Hornbrook Formation, Oregon and California, p. 197-201, Soc. of Econ. Paleontol. and Mineral., Tulsa, Okla., *in*: Hampton, M.A., Lee, H.J. and Locat, J., 1996, Submarine landslides. *Reviews of Geophysics*, v. 34, p. 33–59.

Crans, W., Mandl, G. & Haremboure, J., 1980. On the theory of growth faulting: a geomechanical delta model based on gravity sliding. *Journal of Petroleum Geology*, v. 2, p. 265-307.

Dingle, R. V., 1977. The anatomy of a large submarine slump on a sheared continental margin (southeast Africa), *J. Geol. Soc. London*, v. 134, p. 293-310 in: Hampton, M.A., Lee, H.J. and Locat, J., 1996, Submarine landslides. Reviews of Geophysics, v. 34, p. 33–59.

Eckel, E. B., 1958, landslides and engineering practice, *Spec. Rep* v. 29, p. 1-5.

Eliashiv, H. and Kruvi, O., 2015. Unpublished data.

Evans, G., Morgan, P., Evans, W. E., Evans, T. R. and Woodside, J. M. (1978). Faulting and halokinetics in the northeastern Mediterranean between Cyprus and Turkey. *Geology*, v. 6(7), p. 392-396.

Evans, M., Hastings N, Peacock JB. 2000. Statistical Distributions (3rd edn). John Wiley: New York. *In:* Malamud, B.D., Turcotte, D.L., Guzzetti F., Reichenbach P., 2004. Landslide inventories and their statistical properties, *Earth Surf. Process. Landf.* v. 29, p. 687-711.

Frattini, P. and Crosta, G.B., 2013. The role of material properties and landscape morphology on landslide size distributions, *Earth and Planetary Science Letters*, v. 361, p. 310-319.

Frey-Martinez, J., Cartwright, J.A., Hall, B., 2005. 3D seismic interpretation of slump complexes: examples from the continental margin of Israel. *Basin Research* v. 17, p. 83–108.

Frydman S. and Talesnick M., 1988, Analysis of seismically triggered slides off Israel, Environ. *Geol. Water Sci.* v. 11, p. 21–26.

Galloway W.E., 1986. Growth Faults and Fault-Related Structures of Prograding Terrigenous Clastic Continental Margins Gulf Coast. *Association of Geological Societies Transactions* v. 36, p. 121-128.

Gardosh, M. A. and Druckman, Y., 2006. Seismic stratigraphy, structure and tectonic evolution of the Levantine Basin offshore Israel. *Geological Society, London, Special Publications*, v. 260, p. 201-227.

Garfunkel, Z., 1984, Large-scale submarine rotational slumps and growth faults in the eastern Mediterranean, *Marine Geology*, v. 55, p. 305–324.

Garfunkel, Z. and Almagor, G., 1984, Geology and structure of the continental margin off northern Israel and the adjacent part of the Levantine Basin, *Marine Geology*, v. 62, p. 105-131.

Garfunkel, Z., Arad, A., and Almagor, G., 1977, Palmahim disturbance and similar structures offshore Israel, Unpubl. *Rep., submitted to the Isr. Elec. Corp*. 74 p.

Garfunkel, Z., Arad, A. and AImagor, G., 1979. The palmahim disturbance and its regional setting. *GSI Bull*. 72.

Gibbs, A. D., 1983. Balanced cross-section construction from seismic sections in areas of extensional tectonics, *Journal of Structural Geology*, v. 5, No. 2, p. 153-160.

Ginzburg, A., Cohen, S. S., Hay-Roe, H. and Rosenzweig, A., 1975, Geology of Mediterranean shelf of Israel, *AAPG Bulletin*, v. 59, p. 2142-2160.

Gradmann, S., Hübschera, C., Ben-Avraham, Z., Gajewskia, D. and Netzebanda, G., 2005, Salt tectonics off northern Israel. *Marine and Petroleum Geology* v. 22, p. 597–611.

Guzzetti, F., Malamud, B. D., Turcotte, D. L., Reichenbach, P., 2002. Power-law correlations of landslide areas in central Italy, *Earth and Planetary Science Letters* v. 195 p. 169-183.

Gvirtzman, G. and Buchbinder, B., 1976. The late tertiary of the coastal plain and continental shelf of Israel and its bearing on the history of the eastern Mediterranean Oil Research Division. *Geological Survey of Israel*, p. 1195- 1222.

Gvirtzman, Z., Reshef, M., Buch-Leviatan, O., Groves-Gidney, G., Karcz, Z., Makovsky, Y. and Ben-Avraham, Z, 2015. Bathymetry of the Levant basin: interaction of salt-tectonics and surficial mass movements, *Marine Geology* v. 360, p. 25–39.

Haeussler, P. J., Parsons, T., Finlayson, D. P., Hart, P., Chaytor, J. D., Ryan, H., Lee, H., Labay, K., Peterson, A., and Liberty, L., 2014, New Imaging of Submarine Landslides from the 1964 Earthquake Near Whittier, Alaska, and a Comparison to Failures in Other Alaskan Fjords. *Submarine Mass Movements and Their Consequences. Springer international publishing Switzerland*, p. 361-370.

Hamann, Y., Ehrmann,W., Schmiedl, G., Kruger, S., Stuut, J.B., Kuhnt, T., 2008. Sedimentation processes in the Eastern Mediterranean Sea during the Late Glacial and Holocene revealed by end-member modeling of the terrigenous fraction in marine sediments. *Mar. Geol*. v. 248, p. 97–114.

Hampton, M.A., Lee, H.J. and Locat, J., 1996, Submarine landslides. *Reviews of Geophysics*, v. 34, p. 33–59.

Hjelstuen, B. O. and Brendryen, J., 2014, Submarine Mass Movements and Trigger Mechanisms in Byfjorden, Western Norway, *Submarine Mass Movements and Their Consequences. Springer international publishing Switzerland*, p. 351-359.

Hovius, N., Stark, C.P. and Allen, P.A., 1997. Sediment flux from a mountain belt derived by landslide mapping. *Geology*, v. 25 no. 3, p. 231–234

Hsu¨, K.J., Cita, M.B., Ryan, W.B.F., 1973. The origin of the Mediterranean Evaporites. *In*: Ryan, W.B.F., Hsu¨, K.J. (Eds.), *Init. Repts. DSDP, 13. US Govt. Printing Office*, Washington, DC, p. 1203–1232.

Hsu¨, K.J., Monadert, L., Bernoulli, D., Cita, B.C., Erickson, A., Garrison, R.E., et al., 1978. History of the Mediterranean Salinity Crisis. *In*: Hsu¨, K.J., Montadert, L. (Eds.), *Init. Repts. DSDP, 42 I. US Govt. Printing Office*, Washington, DC, p. 1053–1078.

Hudec, M. R. and Jackson, M. P.A, 2007. Terra infirma: Understanding salt tectonics, *Earth-Science Reviews*, v. 82 p. 1–28.

Huhnerbach V., and Masson D.G., 2004. Landslides in the North Atlantic and its adjacent seas: an analysis of their morphology, setting and behaviour. *Marine Geology* v. 213, p. 343– 362.

Humphris Jr., C.C., 1978. Salt movements on continental slope, northern Gulf of Mexico. *American Association of Petroleum Geologists Studies in Geology*, 7, 69-85 *in*: Netzeband, G. L., 2006, The Levantine Basin – a seismic investigation of the crustal structure and the evolution of the Messinian evaporates, *a Thesis Submitted to the Graduate Faculty of Geosciences of Hamburg University for the degree of Doctorate of Nature Science.*

Hungr , O., Leroueil, S. and Picarelli, L., 2014. The Varnes classification of landslide types, an update, *Landslides*, v. 11, p.167–194. Springer-Verlag Berlin Heidelberg

Johnson N.L. and Kotz S. 1970. *Continuous Univariate Distribution.* Houghton Mifflin: Boston. *In*: Malamud, B.D., Turcotte, D.L., Guzzetti F., Reichenbach P., 2004. Landslide inventories and their statistical properties, *Earth Surf. Process. Landf.* v. 29, p. 687-711.

Katz, O. and Aharonov, E., 2006. Landslides in vibrating sand box: What controls types of slope failure and frequency magnitude relations? *Earth and Planetary Science Letters*, v. 247, p. 280–294.

Katz, O., Morgan, J.K., Aharonov, E. and Dugan, B., 2014. Controls on the size and geometry of landslides: Insights from discrete element numerical simulations. *Geomorphology*, v. 220, p. 104-113.

Katz, O., Reuven, E., Aharonov, E., 2015. Submarine landslides and fault scarps along the eastern Mediterranean Israeli continental-slope. *Marine Geology* v. 369 p. 100–115.

Kehle, R.O., 1988. The origin of salt structures B.C. Schreiber (Ed.), Evaporites and Hydrocarbons, *Columbia University Press,* New York, p. 345–404.

Lee, H. J., 2009. Timing of occurrence of large submarine landslides on the Atlantic Ocean margin. *Marine Geology*, v. 264, p. 53–64.

Lee, S. H., Bahk, J. J., Kim, H. J., Kim, G. Y., Kim, S. P., Jeong, S. W., and Park, S. S., 2014, Contrasting Development of the Latest Quaternary Slope Failures and Mass-Transport Deposits in the Ulleung Basin, East Sea (Japan Sea), in: *Submarine Mass Movements and Their Consequences.* Springer international publishing Switzerland, p. 403-412.

Letouzey, J., B. Colletta, R. Vially, and J. C. Chermette, 1995. Evolution of salt-related structures in compressional settings, in: Gradmann, S., Hübschera, C., Ben-Avraham, Z., Gajewskia, D. and Netzebanda, G., 2005, Salt tectonics off northern Israel, *Marine and Petroleum Geology* v. 22, p. 597–611.

Malamud, B.D., Turcotte, D.L., Guzzetti F., Reichenbach P., 2004. Landslide inventories and their statistical properties, *Earth Surf. Process. Landf*. v. 29, p. 687-711.

Mart, Y. and Ryan, W., 2007. The Levant slumps and the Phoenician structures: collapse features along the continental margin of the southeastern Mediterranean Sea. *Marine Geophysical Research* 28, 297–307.

Martin, R.G., 1978. Northern and eastern gulf of Mexico continental margin: Stratigraphic and structural framework. Framework, facies, and oil trapping characteristics of the upper continental margin. *American Association of Petroleum Geologists Studies in Geology*, v. 7, p. 21-42 *in:* Netzeband, G. L., 2006, The Levantine Basin – a seismic investigation of the crustal structure and the evolution of the Messinian evaporates, a Thesis Submitted to the Graduate Faculty of Geosciences of Hamburg University for the degree of Doctorate of Nature Science.

Mascle, J., Sardou, O., Loncke, L., Migeon, S., Caméra, L., & Gaullier, V. (2006). Morphostructure of the Egyptian continental margin: insights from swath bathymetry surveys. *Marine Geophysical Researches*, v. 27(1), p. 49-59.

Masson, D. G., Harbitz, C. B., Wynn, R. B., Redersen, G. P and L"Vholt, F., 2006. Submarine landslides: processes, triggers and hazard prediction, *Phil. Trans. R. Soc. A*, v. 364, p. 2009–2039.

McAdoo, B.G., Pratson, L.F. and Orange D.L., 2000, Submarine landslide geomorphology, US continental slope, *Marine Geology,* v. 169, p. 103–136.

McAdoo, B.G. and Watts, P., 2004. Tsunami hazard from submarine landslides on the Oregon continental slope, *Marine Geology,* v. 203, p. 235-245.

McClay, R., 1990. Extensional fault systems in sedimentary basins: a review of analogue model studies, *Marine and Petroleum Geology*. p. 206-233.

McClay, K.R. and Scott, A.D., 1991. Experimental models of hangingwall deformation in ramp-flat listric extensional fault systems. *Tectonophysics*, v. 188 p. 85-96.

Micallef, A., Berndt, C., Masson, D.G. and Stow D. A.V, 2008. Scale invariant characteristics of the Storegga Slide and implications for large-scale submarine mass movements. *Marine Geology*, v. 247, p. 46–60.

Modiin Energy, 'Yam Hadera' 3D survey.

Netzeband, G. L., 2006, The Levantine Basin – a seismic investigation of the crustal structure and the evolution of the Messinian evaporates, a Thesis Submitted to the Graduate Faculty of Geosciences of Hamburg University for the degree of Doctorate of Nature Science.

Normark, W.R., McGann, M., Sliter, R., 2004. Age of Palos Verdes submarine debris avalanche, southern California. *Mar. Geol*. v. 203, p. 247–259.

Prior, D. B., and Coleman, J. M., 1978. Disintegrative retrogressive landslides on very-low-angle subaqueous slopes, Mississippi delta, *Mar. Geotechnol.*, v. 3, p. 37-60 *in*: Hampton, M.A., Lee, H.J. and Locat, J., 1996, Submarine landslides. *Reviews of Geophysics*, v. 34, p. 33–59.

Prior, D.B., Doyle, E.H., Neurauter, T., 1986. The Currituck slide, Mid-Atlantic continental slope—revisited. *Mar. Geol*. v. 73, p. 25–45.

Rohrlich, V., Goldsmith, V., 1984. Sediment transport along the southeast Mediterranean: a geological perspective. *Geo Mar. Lett.* v. 4, p. 99–103 *in*: Zviely, D., Kit, E. and Klein, M., 2007. Longshore sand transport estimates along the Mediterranean coast of Israel in the Holocene. *Marine Geology*, v. 238, p. 61–73.

Rossi, M., Cardinali, M., Fiorucci, F., Marchesini I., Mondini, A.C., Santangelo, M., Ghosh, S., Riguer, D.E.L., Lahousse, T., Chang, K.T. and Guzzetti, F., 2012. A tool for the estimation of the distribution of landslide area in R, *Geophysical Research Abstracts* v. 14, EGU2012-9438-1, EGU General Assembly.

Sade R., 2007, Morphology and acoustic backscatter of the northern Israel continental margin based on high resolution multibeam sonar. MSc. Thesis 95 p., Tel Aviv University.

Sade R., Hall J.K., Amit, G., Golan, A., Gur-Arieh, L. and Tibor, G., 2007, The Israel national bathymetric survey – a new look at the seafloor of Israel. *Israel Journal Earth Sciences*, v. 55, p. 185-187.

Schilman, B., Bar-Matthews, M., Almogi-Labin, A., and Luz, B., 2001. Global climate instability re£ected by Eastern Mediterranean marine records during the late Holocene. *Palaeogeography, Palaeoclimatology, Palaeoecology* v. 176, p. 157 – 176.

Schuster, R. L. and Krizek R. J., 1978, Landslides- Analysis and Control, *Spec. Rep*. v. 176, Transportation and Road Research Board, *National Academy of Science, Washington D. C.*, p. 1-10.

Segall, P. and Fitzgerald, S.D., 1998. A note on induced stress changes in hydrocarbon and geothermal reservoirs. *Tectonophysics* v. 289, p. 117–128.

Shelton, J.W., 1984, Listric normal faults: An illustrated summary: *American Association of Petroleum Geologists Bulletin*, v. 68, p. 801-815.

Stark C.P. and Guzzetti, F., 2009. Landslide rupture and the probability distribution of mobilized debris volumes. *Journal of Geophysical Research* v. 144, doi:10.1029/2008JF001008.

Sultan, N., P. Cochonat, J. P. Foucher, and J. Mienert, 2004. Effect of gas hydrate melting on seafloor slope stability, *Mar. Geol.*, v. 231, p. 379–401, doi:10.1016/j.margeo.2004.10.015. Tibor, G., Sade R., Sade H. Hall J.K., 2013, Data collection and processing of multibeam data from the deep water offshore Israel. *IOLR report* H-31/2013.

Sultan, N., M. Voisset, T. Marsset, A. M. Vernant, E. Cauquil, J. L. Colliat, and V. Curinier, 2007. Detection of free gas and gas hydrate based on 3D seismic data and cone penetration testing: An example from the Nigerian Continental Slope, *Mar. Geol*., v. 240(1–4), p. 235–255, doi:10.1016/j.margeo.2007.02.012. *in*: Budillon, F., Cesarano, M., Conforti, A., Pappone, G., Di Martino, G., and Pelosi, N, 2014, Recurrent Superficial Sediment Failure and Deep Gravitational Deformation in a Pleistocene Slope Marine Succession: The Poseidonia Slide (Salerno Bay, Tyrrhenian Sea), *in*: Submarine Mass Movements and Their Consequences. Springer international publishing Switzerland, p. 273-283.

Talling, P. J., Wynn, R. B., Masson, D. G., Frenz, M., Cronin, B. T., Schiebel, R., Akhmetzhanov, A. M., Dallmeier-Tiessen, S., Benetti, S., Weaver, P. P. E., Georgiopoulou, A., Zu ¨hlsdorff C. and Amy L. A., 2007. Onset of submarine debris flow deposition far from original giant landslide, Nature, v. 450, p. 541- 544.

TGS-NOPEC Geophysical Company L.P Geophysical Company L.P, 2001

Tibor, G., Sade, R., Sade, H., Hall, J.K., 2013. Data collection and processing of multibeam data from the deep water offshore Israel. *IOLR report* H-31/2013.

Trusheim, F., 1987. Halokinesis, Structural Geology and Tectonics Encyclopedia of Earth Science, p. 324-332.

Urgeles, R. and Camerlenghi, A., 2013. Submarine landslides of theMediterranean Sea: Triggermechanisms, dynamics, and frequency-magnitude distribution. *Journal of geophysical research: Earth Surface*, v. 118, p. 2600–2618, doi:10.1002/2013JF002720

Urlaub, M., Talling, P.J., Masson, D.G., 2013. Timing and frequency of large submarine landslides: implications for understanding triggers and future geohazard. *Quat. Sci. Rev*. v. 72, p. 63–82.

Utili, S., 2005. An analytical relationship for weathering induced slope retrogression: a benchmark. *Ital. Geotech. J*. v. 39, p. 9–30.

Utili, S. and Nova R., 2008. DEM analysis of bonded granular geomaterials *Int. J. Numer. Anal. Meth. Geomech.* v. 32, p. 1997–2031. DOI: 10.1002/nag

Whitehouse, I.E., 1983. Distribution of large rock avalanche deposits in the central Southern Alps, New Zealand. N. Z. J. *Geol. Geophys*. v. 26, p. 271-279.

Zviely, D., Kit, E. and Klein, M., 2007. Longshore sand transport estimates along the Mediterranean coast of Israel in the Holocene. *Marine Geology, v.* 238, p. 61–73.

10. supplementary data

Table S1 in supplementary data

The properties of each mapped landslide are summarized here. In ‘Section’ we defined ‘N’ for northern landslide and ‘S’ for southern landslide. For Type we defined ‘SL’ for Slump and ‘F’ for Flow slide

Number	Coordinates				Section	Area	Hierarchy	Scar Head	Toe	Scar Height	Type
	Lat (N)	Long (E)	UTM (N)	UTM (E)		(km^2)		Elevation(m)	Elevation(m)	(m)	
1	32° 43' 25.1009"	34° 47' 24.6523"	3622024	667700	N	0.119	P	-352.4	-416.9	24	SL
2	32° 43' 31.5946"	34° 47' 28.5922"	3622225	667799	N	0.046	S	-353.93	-404.91	17	SL
3	32° 42' 53.3147"	34° 46' 48.5876"	3621029	666778	N	0.12	P	-463.1	-573.7	26	SL
4	32° 42' 52.7167"	34° 46' 13.7744"	3620995	665872	N	0.3017	P	-597	-682.1	15	SL
5	32° 42' 54.4655"	34° 46' 17.0237"	3621051	665955	N	0.0609	S	-570.8	-619.56	6	SL
6	32° 42' 44.9108"	34° 46' 37.0233"	3620765	666481	N	0.1059	P	-517.416	-583.04	23	SL
7	32° 42' 6.2417"	34° 47' 55.1412"	3619608	668535	N	1.275	P	-282.7	-565.4	23	SL
8	32° 42' 29.8388"	34° 47' 15.2694"	3620318	667485	N	0.0193	S	-332.29	-366.85	14	SL
9	32° 42' 28.8110"	34° 47' 22.2372"	3620289	667667	N	0.0106	S	-319.27	-339.68	10	SL
10	32° 42' 24.7838"	34° 47' 26.4496"	3620167	667778	N	0.0105	S	-312.32	-338.85	12	SL
11	32° 42' 27.5888"	34° 47' 42.7783"	3620260	668202	N	0.091	S	-283.67	-333.44	9	SL
12	32° 42' 23.6216"	34° 47' 48.6887"	3620141	668358	N	0.0584	S	-266.45	-310.94	16	SL
13	32° 42' 5.4808"	34° 48' 22.9937"	3619597	669261	N	0.508	S	-220.41	-304.43	26	SL
14	32° 42' 23.5001"	34° 48' 6.4130"	3620145	668820	N	0.0159	T	-244.1	-255.39	9	SL
15	32° 42' 17.7771"	34° 48' 14.5853"	3619972	669035	N	0.0101	T	-233.7	-248.66	7	SL
16	32° 42' 13.2366"	34° 48' 25.7853"	3619837	669329	N	0.045	T	-217	-243.27	12	SL
17	32° 42' 1.4564"	34° 48' 22.7509"	3619473	669257	N	0.0255	T	-218.5	-242.07	16	SL
18	32° 41' 56.6216"	34° 48' 17.8886"	3619322	669133	N	0.1575	T	-229.9	-306.38	11	SL
19	32° 41' 44.2706"	34° 47' 59.7204"	3618934	668666	N	0.1437	S	-275.65	-322.07	16	SL

Number	Coordinates				Section	Area	Hierarchy	Scar Head	Toe	Scar Height	Type
	Lat (N)	Long (E)	UTM (N)	UTM (E)		(km^2)		Elevation(m)	Elevation(m)	(m)	
20	32° 41' 54.2909"	34° 48' 3.3398"	3619244	668755	N	0.0772	T	-261.1	-298.25	23	SL
21	32° 42' 12.5579"	34° 46' 48.4413"	3619774	666795	N	0.802	P	-443.6	-673.5	9	SL
22	32° 42' 25.6691"	34° 46' 51.0494"	3620178	666856	N	0.0706	S	-441.19	-502.89	25	SL
23	32° 42' 10.5425"	34° 46' 49.7402"	3619712	666830	N	0.109	S	-432.95	-526.91	9	SL
24	32° 42' 4.9013"	34° 46' 42.6054"	3619535	666647	N	0.1009	S	-446.14	-520.57	20	SL
25	32° 42' 7.9512"	34° 46' 28.6204"	3619623	666281	N	0.0704	S	-475.8	-545.76	17	SL
26	32° 41' 18.5814"	34° 47' 46.1133"	3618136	668325	N	1.761	P	-308.9	-471.1	26	SL
27	32° 41' 38.3528"	34° 46' 55.8525"	3618723	667006	N	0.03999	S	-394.44	-423.45	14	SL
28	32° 41' 38.5360"	34° 47' 10.5486"	3618735	667388	N	0.0449	S	-371.58	-399.18	10	SL
29	32° 41' 33.0013"	34° 47' 21.1612"	3618570	667668	N	0.0286	S	-357.92	-384.08	14	SL
30	32° 41' 37.9016"	34° 47' 36.6731"	3618727	668069	N	0.1404	S	-312.08	-368.34	25	SL
31	32° 41' 26.5998"	34° 47' 59.1670"	3618389	668661	N	0.3461	S	-272.55	-364.02	25	SL
32	32° 41' 32.1825"	34° 47' 52.4919"	3618558	668484	N	0.0485	T	-248.18	-470.65	27	SL
33	32° 41' 29.9243"	34° 48' 4.0419"	3618494	668786	N	0.0494	T	-248.18	-470.65	31	SL
34	32° 41' 14.2627"	34° 48' 1.6576"	3618010	668732	N	0.0569	T	-248.18	-470.65	36	SL
35	32° 40' 45.8785"	34° 48' 11.3530"	3617140	668999	N	0.2915	S	-248.13	-370.53	29	SL
36	32° 41' 8.7500"	34° 47' 59.5879"	3617840	668681	N	0.0898	T	-279.6	-340.23	31	SL
37	32° 40' 56.2314"	34° 47' 29.2938"	3617441	667898	N	0.175	P	-329.3	-408.7	16	SL
38	32° 40' 54.5472"	34° 47' 31.1560"	3617390	667948	N	0.0351	S	-331.67	-367.86	12	SL
39	32° 40' 47.3337"	34° 47' 28.8999"	3617166	667893	N	0.015	S	-344.86	-367.18	18	SL
40	32° 40' 46.2304"	34° 47' 39.7555"	3617137	668176	N	0.155	P	-312.4	-403.6	12	SL
41	32° 40' 40.5191"	34° 47' 42.1420"	3616962	668241	N	0.0447	S	-308.01	-354.35	33	SL
42	32° 40' 34.1634"	34° 47' 35.1050"	3616764	668061	N	0.0299	S	-334.54	-379.22	33	SL
43	32° 40' 9.9401"	34° 48' 14.6284"	3616035	669104	N	1.204	P	-252.1	-369.8	23	SL
44	32° 40' 29.2982"	34° 48' 16.0169"	3616632	669130	N	0.2508	S	-236.68	-322.37	33	SL
45	32° 40' 24.6404"	34° 48' 22.4468"	3616491	669299	N	0.045	T	-242.3	-292.8	26	SL

Number	Lat (N)	Long (E)	Coordinates UTM (N)	UTM (E)	Section	Area (km^2)	Hierarchy	Scar Head Elevation(m)	Toe Elevation(m)	Scar Height (m)	Type
46	32° 40' 0.5218"	34° 48' 26.8678"	3615750	669427	N	0.2373	S	-212.28	-321.14	30	SL
47	32° 39' 51.6920"	34° 48' 11.7368"	3615472	669038	N	0.0226	S	-243.43	-300.37	16	SL
48	32° 39' 32.9515"	34° 48' 8.4681"	3614893	668962	N	0.4844	P	-241.2	-337.4	32	SL
49	32° 39' 45.7998"	34° 47' 58.4061"	3615284	668694	N	0.0712	S	-264.57	-321.9	30	SL
50	32° 39' 38.7984"	34° 48' 6.5719"	3615072	668910	N	0.0563	S	-243.98	-306.03	26	SL
51	32° 39' 24.6587"	34° 48' 7.7143"	3614637	668947	N	0.1566	S	-222.71	-331.92	40	SL
52	32° 39' 20.7361"	34° 47' 54.2124"	3614510	668597	N	0.0489	S	-269.91	-322.13	16	SL
53	32° 39' 27.7435"	34° 48' 39.0334"	3614746	669761	N	0.224	P	-129.521	-238.637	13	SL
54	32° 39' 21.1262"	34° 48' 23.0053"	3614535	669347	N	0.154	P	-185.168	-252.868	11	SL
55	32° 39' 58.8178"	34° 46' 53.8188"	3615657	667004	N	0.0449	P	-404.3	-429.7	18	SL
56	32° 39' 43.7732"	34° 46' 53.2765"	3615193	666998	N	0.0893	P	-394.4	-430.9	20	SL
57	32° 39' 16.7215"	34° 46' 56.2039"	3614361	667088	N	0.1078	P	-384	-420.5	17	SL
58	32° 38' 58.1384"	34° 47' 8.5415"	3613794	667419	N	0.0982	P	-359.7	-401.6	26	SL
59	32° 38' 26.6381"	34° 47' 58.5101"	3612846	668738	N	1.108	P	-171.4	-399.6	42	SL
60	32° 38' 29.7369"	34° 48' 1.5972"	3612943	668816	N	0.785	S	-156.96	-396.96	35	SL
61	32° 37' 51.0943"	34° 46' 33.2355"	3611714	666534	N	0.588	P	-339.9	-469.6	30	SL
62	32° 38' 3.1706"	34° 45' 59.0803"	3612071	665637	N	0.0095	S	-416.23	-443.65	18	SL
63	32° 38' 2.1132"	34° 46' 18.5093"	3612047	666144	N	0.0127	S	-385.71	-403.54	16	SL
64	32° 38' 0.7253"	34° 46' 25.3117"	3612007	666322	N	0.0098	S	-375.66	-397.88	20	SL
65	32° 37' 59.7984"	34° 46' 35.6969"	3611983	666593	N	0.0543	S	-343.01	-393.76	30	SL
66	32° 37' 58.4336"	34° 46' 38.3232"	3611942	666663	N	0.0156	T	-335.15	-361.59	22	SL
67	32° 37' 50.0068"	34° 46' 33.8515"	3611681	666550	N	0.0184	S	-343.77	-380.42	43	SL
68	32° 37' 45.6530"	34° 46' 36.5883"	3611548	666624	N	0.0371	S	-320.53	-382.76	16	SL
69	32° 37' 38.3713"	34° 46' 22.9679"	3611318	666273	N	0.0174	S	-369.25	-394.07	21	SL
70	32° 37' 46.6880"	34° 46' 4.7466"	3611566	665794	N	0.0242	S	-389.13	-426.39	6	SL
71	32° 37' 4.9205"	34° 46' 58.7075"	3610303	667221	N	0.591	P	-174.6	-316.6	8	SL

Number	Lat (N)	Long (E)	Coordinates UTM (N)	UTM (E)	Section	Area (km^2)	Hierarchy	Scar Head Elevation(m)	Toe Elevation(m)	Scar Height (m)	Type
72	32° 37' 17.1325"	34° 46' 58.3057"	3610679	667205	N	0.0069	S	-181.99	-193.86	8	SL
73	32° 37' 11.3707"	34° 46' 59.0285"	3610502	667226	N	0.0064	S	-177.58	-189.61	8	SL
74	32° 37' 6.6999"	34° 47' 0.0305"	3610359	667255	N	0.0072	S	-173.12	-185.43	11	SL
75	32° 37' 3.5443"	34° 46' 58.4867"	3610261	667216	N	0.0051	S	-173.74	-184.8	7	SL
76	32° 36' 56.4537"	34° 46' 48.6240"	3610038	666963	N	0.0166	S	-184.23	-210.48	17	SL
77	32° 37' 30.3385"	34° 45' 59.6311"	3611060	665669	N	0.0654	P	-402.2	-460.1	9	SL
78	32° 37' 34.3823"	34° 45' 57.9292"	3611184	665622	N	0.0064	S	-410.34	-430.98	8	SL
79	32° 37' 31.9827"	34° 46' 0.6233"	3611111	665694	N	0.0079	S	-398.72	-426.97	6	SL
80	32° 37' 29.1106"	34° 45' 59.2538"	3611022	665659	N	0.0056	S	-398.13	-423.15	13	SL
81	32° 37' 3.4318"	34° 46' 23.5799"	3610242	666307	N	0.2269	P	-272.5	-452.3	14	SL
82	32° 37' 18.2270"	34° 46' 1.8865"	3610688	665734	N	0.0068	S	-375.74	-397.45	11	SL
83	32° 36' 56.0809"	34° 46' 39.1853"	3610022	666717	N	0.1438	P	-199.8	-277.8	13	SL
84	32° 37' 3.1283"	34° 45' 56.9501"	3610221	665613	N	0.2206	P	-362.1	-447.5	21	SL
85	32° 36' 37.1941"	34° 46' 44.2883"	3609443	666860	N	0.2012	P	-173.2	-256.2	15	SL
86	32° 36' 43.0769"	34° 46' 32.2382"	3609619	666543	N	0.0396	S	-204.92	-256.24	24	SL
87	32° 36' 36.8526"	34° 46' 48.0308"	3609434	666958	N	0.0509	S	-169.42	-200.19	8	SL
88	32° 36' 22.4331"	34° 46' 43.8639"	3608988	666856	N	0.0353	S	-172.79	-209.71	20	SL
89	32° 36' 3.6518"	34° 46' 22.3394"	3608400	666305	N	0.0944	P	-213.2	-266.7	24	SL
90	32° 38' 15.5696"	34° 44' 53.7370"	3612425	663928	N	2.348	P	-538.4	-582.3	30	SL
91	32° 38' 4.2065"	34° 44' 46.3164"	3612072	663741	N	0.04523	P	-553.801	-580	12	SL
92	32° 37' 33.3128"	34° 44' 42.3467"	3611119	663653	N	0.2167	P	-542.2	-593.6	34	SL
93	32° 36' 47.7200"	34° 44' 47.6273"	3609717	663814	N	7.563	P	-482.9	-646.4	47	SL
94	32° 36' 42.1039"	34° 44' 51.7404"	3609545	663924	N	0.4823	S	-458.32	-584.31	40	SL
95	32° 36' 44.6546"	34° 44' 56.5835"	3609626	664049	N	0.086	T	-455.5	-529.25	33	SL
96	32° 35' 50.9470"	34° 44' 43.5245"	3607966	663735	N	1.862	P	-418	-616.8	13	SL
97	32° 36' 16.9218"	34° 44' 44.3113"	3608767	663743	N	0.3072	S	-425.45	-535.48	20	SL

Number	Coordinates				Section	Area	Hierarchy	Scar Head	Toe	Scar Height	Type
	Lat (N)	Long (E)	UTM (N)	UTM (E)		(km^2)		Elevation(m)	Elevation(m)	(m)	
98	32° 35' 45.8678"	34° 44' 47.1040"	3607811	663831	N	0.1745	S	-406.44	-437.9	16	SL
99	32° 35' 37.0631"	34° 45' 0.2301"	3607546	664178	N	1.319	T	-368.44	-615.34	43	SL
100	32° 35' 33.8745"	34° 44' 22.5408"	3607432	663197	N	0.0477	S	-426.18	-458.89	8	SL
101	32° 35' 55.2667"	34° 43' 50.9831"	3608077	662363	N	0.285	P	-503.34	-609.6	15	SL
102	32° 35' 29.9899"	34° 43' 31.2508"	3607290	661862	N	0.2271	P	-495.754	-551.297	20	SL
103	32° 34' 53.8968"	34° 44' 3.1744"	3606192	662712	N	1.804	P	-411	-639.7	13	SL
104	32° 35' 10.7979"	34° 43' 59.5589"	3606711	662609	N	0.1115	S	-428.66	-471.84	8	SL
105	32° 34' 56.5642"	34° 43' 16.4955"	3606254	661493	N	0.0603	S	-467.8	-514.9	7	SL
106	32° 35' 16.8775"	34° 42' 51.1803"	3606869	660823	N	0.0349	S	-550.32	-602.67	1	SL
107	32° 34' 3.7876"	34° 43' 32.0623"	3604636	661926	N	3.393	P	-396.2	-618.6	10	SL
108	32° 34' 24.0501"	34° 43' 30.1033"	3605259	661865	N	0.0919	S	-405.29	-440.08	10	SL
109	32° 34' 3.2883"	34° 43' 32.5780"	3604620	661939	N	0.1582	S	-392.51	-436.21	8	SL
110	32° 33' 48.1153"	34° 43' 6.2148"	3604142	661259	N	0.1948	S	-406.36	-456.25	3	SL
111	32° 34' 44.1203"	34° 45' 56.3755"	3605940	665669	N	0.01286	P	-190.9	-212.4	11	SL
112	32° 34' 35.8918"	34° 45' 55.5029"	3605686	665650	N	0.03959	P	-188	-226.9	11	SL
113	32° 34' 15.7553"	34° 45' 51.7243"	3605064	665562	N	0.753	P	-180.9	-280.3	25	SL
114	32° 34' 30.3736"	34° 45' 44.6675"	3605511	665370	N	0.0541	S	-208.7	-247 m	20	SL
115	32° 34' 28.7585"	34° 45' 55.0481"	3605466	665642	N	0.0227	S	-190.6	-212.37	14	SL
116	32° 34' 18.0216"	34° 45' 37.6806"	3605128	665195	N	0.0103	S	-213.63	-238.57	9	SL
117	32° 34' 14.0042"	34° 45' 33.1764"	3605002	665079	N	0.0138	S	-212.38	-243.52	20	SL
118	32° 34' 8.7445"	34° 45' 31.9730"	3604839	665050	N	0.0537	P	-208.5	-247.3	15	SL
119	32° 34' 4.0282"	34° 45' 26.3660"	3604692	664907	N	0.02317	P	-216.4	-244.4	22	SL
120	32° 33' 59.7619"	34° 45' 23.8842"	3604559	664844	N	0.01954	P	-214.1	-240.3	17	SL
121	32° 33' 46.2553"	34° 45' 19.2851"	3604141	664731	N	0.03405	P	-210.7	-241.2	14	SL
122	32° 33' 38.6620"	34° 45' 6.0967"	3603902	664391	N	0.0189	P	-221.7	-247.3	11	SL
123	32° 33' 38.0686"	34° 44' 59.7398"	3603881	664225	N	0.02744	P	-231.6	-255.4	11	SL

Number	Coordinates Lat (N)	Long (E)	UTM (N)	UTM (E)	Section	Area (km^2)	Hierarchy	Scar Head Elevation(m)	Toe Elevation(m)	Scar Height (m)	Type
124	32° 33' 33.8039"	34° 44' 52.8931"	3603747	664049	N	0.01323	P	-231.9	-255.5	14	SL
125	32° 33' 30.4719"	34° 44' 44.8542"	3603641	663841	N	0.01447	P	-241.9	-268.3	17	SL
126	32° 33' 24.1005"	34° 44' 41.4755"	3603443	663756	N	0.1211	P	-249.5	-284.2	10	SL
127	32° 33' 28.4271"	34° 44' 45.0378"	3603578	663847	N	0.0231	S	-233.78	-264.28	15	SL
128	32° 33' 22.8118"	34° 44' 43.4885"	3603404	663809	N	0.0078	S	-234.35	-257.51	19	SL
129	32° 33' 21.4399"	34° 44' 35.9859"	3603359	663614	N	0.0156	S	-246	-267.44	10	SL
130	32° 33' 38.4688"	34° 44' 14.7529"	3603874	663052	N	0.1554	P	-283.1	-316	10	SL
131	32° 32' 24.4243"	34° 45' 3.4544"	3601614	664360	N	8.156	P	-172	-401.2	23	SL
132	32° 33' 23.0921"	34° 44' 21.2629"	3603403	663229	N	0.1365	S	-239.4	-284.1	7	SL
133	32° 33' 19.7045"	34° 44' 32.5526"	3603304	663526	N	0.0684	T	-237.75	-271.07	20	SL
134	32° 33' 9.1769" N	34° 44' 55.5064"	3602989	664130	N	0.3471	S	-201.28	-242.58	9	SL
135	32° 33' 9.8427"	34° 44' 56.7331"	3603010	664161	N	0.0236	T	-207.14	-223.83	15	SL
136	32° 33' 3.6098"	34° 45' 0.3738"	3602820	664259	N	0.0247	T	-200.98	-225.39	8	SL
137	32° 32' 58.9070"	34° 45' 1.0582"	3602675	664280	N	0.0461	T	-196.86	-229.27	12	SL
138	32° 32' 49.7276"	34° 45' 20.3258"	3602401	664787	N	0.386	S	-174.14	-226.12	19	SL
139	32° 32' 55.9079"	34° 45' 21.5803"	3602592	664816	N	0.135	T	-178.44	-204.49	15	SL
140	32° 32' 28.9875"	34° 45' 5.2293"	3601756	664404	N	0.04601	S	-180.32	-208.66	23	SL
141	32° 32' 19.0764"	34° 45' 4.9115"	3601450	664400	N	0.0703	S	-177.03	-209.77	14	SL
142	32° 32' 8.3131"	34° 44' 59.9166"	3601117	664275	N	0.0568	S	-173.76	-211.32	20	SL
143	32° 31' 48.6969"	34° 44' 52.5604"	3600509	664093	N	0.2878	S	-170.59	-217.11	12	SL
144	32° 32' 0.6223"	34° 44' 59.9576"	3600880	664280	N	0.0223	T	-170.94	-204.64	15	SL
145	32° 31' 54.7742"	34° 45' 0.2859"	3600700	664292	N	0.046	T	-166.87	-204.9	21	SL
146	32° 31' 46.2692"	34° 44' 12.7322"	3600418	663055	N	0.2592	S	-206.58	-257.87	15	SL
147	32° 32' 2.6527"	34° 44' 10.2313"	3600921	662982	N	0.0385	T	-224.28	-246.11	10	SL
148	32° 31' 54.7127"	34° 44' 1.6840"	3600673	662763	N	0.0085	T	-227.01	-239.17	8	SL
149	32° 32' 1.3363"	34° 43' 55.9569"	3600874	662610	N	0.0184	T	-233.29	-251.63	9	SL

Number	Coordinates				Section	Area	Hierarchy	Scar Head	Toe	Scar Height	Type
	Lat (N)	Long (E)	UTM (N)	UTM (E)		(km^2)		Elevation(m)	Elevation(m)	(m)	
150	32° 32' 0.0956"	34° 43' 45.7708"	3600832	662345	N	0.1406	S	-238.13	-274.9	10	SL
151	32° 32' 5.3099"	34° 43' 50.2879"	3600994	662460	N	0.0209	T	-238.48	-265.51	12	SL
152	32° 31' 45.2927"	34° 43' 45.0457"	3600376	662334	N	1.275	P	-228.2	-343.3	13	SL
153	32° 31' 54.9580"	34° 43' 53.5605"	3600677	662551	N	0.0295	S	-227.49	-243.3	4	SL
154	32° 31' 41.7097"	34° 43' 42.0295"	3600264	662257	N	0.066	S	-228.74	-259.45	8	SL
155	32° 31' 39.0150"	34° 43' 31.7513"	3600177	661990	N	0.0878	S	-235.61	-265.86	7	SL
156	32° 31' 37.9173"	34° 43' 24.0625"	3600140	661790	N	0.0636	S	-241.42	-269.48	13	SL
157	32° 31' 13.5174"	34° 43' 3.8582"	3599380	661275	N	1.376	P	-235.8	-370.9	16	SL
158	32° 31' 35.8881"	34° 43' 10.4317"	3600071	661435	N	0.0361	S	-254.33	-280.52	14	SL
159	32° 31' 23.2121"	34° 43' 9.0376"	3599681	661405	N	0.0201	S	-238.61	-258.04	10	SL
160	32° 31' 15.2784"	34° 43' 6.0049"	3599435	661330	N	0.0124	S	-234.7	-252.24	8	SL
161	32° 31' 8.4431"	34° 42' 57.6539"	3599221	661115	N	0.0327	S	-237.95	-271.51	13	SL
162	32° 31' 11.2233"	34° 42' 47.1017"	3599302	660839	N	0.0364	S	-263.22	-303.86	9	SL
163	32° 31' 15.2526"	34° 42' 38.0532"	3599422	660601	N	0.0356	S	-288.99	-317.93	11	SL
164	32° 31' 17.7390"	34° 42' 23.2887"	3599493	660214	N	1.356	P	-316.3	-420.5	12	SL
165	32° 31' 4.7710"	34° 42' 17.7350"	3599091	660076	N	0.2231	S	-310.18	-346.94	10	SL
166	32° 31' 19.9050"	34° 42' 30.6196"	3599563	660404	N	0.0101	T	-308.99	-337.63	23	SL
167	32° 31' 11.1107"	34° 42' 26.9271"	3599290	660312	N	0.0182	T	-305.07	-335.11	24	SL
168	32° 33' 22.7518"	34° 42' 30.1431"	3603346	660331	N	0.4743	P	-437.449	-501.244	12	SL
169	32° 33' 18.2174"	34° 42' 42.9286"	3603211	660667	N	0.3309	P	-420.536	-446.598	10	SL
170	32° 32' 52.4015"	34° 42' 58.9978"	3602423	661099	N	0.598	P	-363.1	-525.4	25	SL
171	32° 32' 19.9729"	34° 43' 7.1876"	3601428	661329	N	1.816	P	-332.1	-528.6	20	SL
172	32° 32' 45.4642"	34° 42' 24.3096"	3602195	660197	N	0.0638	S	-421.69	-471.24	8	SL
173	32° 32' 41.0201"	34° 42' 49.4124"	3602069	660854	N	0.0272	S	-370.57	-402.16	10	SL
174	32° 32' 37.5787"	34° 42' 54.4058"	3601965	660986	N	0.0121	S	-359.65	-378.66	13	SL
175	32° 32' 33.8867"	34° 43' 1.0627"	3601854	661162	N	0.0232	S	-350.44	-372.83	8	SL

Number	Coordinates				Section	Area	Hierarchy	Scar Head	Toe	Scar Height	Type
	Lat (N)	Long (E)	UTM (N)	UTM (E)		(km^2)		Elevation(m)	Elevation(m)	(m)	
176	32° 32' 30.0218"	34° 43' 7.0165"	3601737	661319	N	0.0343	S	-337.58	-369.08	9	SL
177	32° 32' 18.9749"	34° 43' 11.4879"	3601399	661441	N	0.0872	S	-312.9	-367.17	16	SL
178	32° 32' 9.9742"	34° 42' 52.6016"	3601114	660953	N	0.0225	S	-340.92	-369.62	20	SL
179	32° 32' 7.8072"	34° 42' 43.1276"	3601043	660707	N	0.0237	S	-352.24	-399.7	29	SL
180	32° 32' 6.9144"	34° 42' 34.4911"	3601012	660482	N	0.0237	S	-380.58	-406.46	13	SL
181	32° 32' 5.8177"	34° 42' 29.0220"	3600976	660340	N	0.0288	S	-382.63	-412.72	21	SL
182	32° 32' 2.3883"	34° 42' 22.8584"	3600868	660181	N	0.0488	S	-374.08	-414.28	26	SL
183	32° 32' 8.3754"	34° 42' 13.1322"	3601048	659924	N	0.0304	S	-391.8	-431	6	SL
184	32° 32' 31.3832"	34° 41' 43.5467"	3601744	659141	N	0.0575	P	-473.2	-522.6	29	SL
185	32° 32' 14.3500"	34° 41' 33.9635"	3601216	658899	N	0.1141	P	-448.1	-509.3	12	SL
186	32° 31' 56.8433"	34° 41' 29.0765"	3600675	658780	N	0.0941	P	-448.8	-498.5	7	SL
187	32° 32' 6.7577"	34° 40' 26.9767"	3600954	657156	N	2.284	P	-548.4	-750.2	32	SL
188	32° 33' 0.9084"	34° 40' 9.7667"	3602615	656680	N	0.4101	S	-646.89	-750.2	17	SL
189	32° 32' 47.1264"	34° 40' 21.1830"	3602195	656985	N	0.1888	S	-619.29	-686.76	11	SL
190	32° 32' 4.9396" N	34° 40' 28.5344"	3600899	657197	N	0.0736	S	-549.15	-620.14	33	SL
191	32° 31' 47.8670"	34° 40' 17.0786"	3600368	656906	N	0.0498	S	-549.1	-576.71	11	SL
192	32° 31' 37.3854"	34° 39' 54.2537"	3600036	656316	N	1.176	P	-526.3	-776.5	40	SL
193	32° 31' 36.6226"	34° 39' 55.3004"	3600013	656344	N	0.1178	S	-576.98	-643.25	17	SL
194	32° 31' 33.8874"	34° 39' 46.9403"	3599926	656127	N	0.0451	S	-587.82	-628.89	13	SL
195	32° 31' 28.2765"	34° 39' 40.8257"	3599750	655970	N	0.1071	S	-580.54	-647.55	20	SL
196	32° 31' 28.5504"	34° 39' 30.5817"	3599755	655703	N	0.0716	S	-592.63	-648.09	6	SL
197	32° 31' 22.9130"	34° 39' 24.0510"	3599578	655535	N	0.536	P	-550.2	-778.5	40	SL
198	32° 31' 22.0762"	34° 39' 28.4046"	3599554	655649	N	0.0848	S	-586.94	-647.25	35	SL
199	32° 31' 16.2814"	34° 39' 22.6522"	3599373	655502	N	0.0506	S	-598.55	-660.46	25	SL
200	32° 30' 57.7723"	34° 39' 15.9069"	3598801	655334	N	2.49	P	-605	-793.3	16	SL
201	32° 31' 12.5507"	34° 39' 12.1300"	3599254	655229	N	0.0772	S	-621.66	-713.54	20	SL

Number	Lat (N)	Long (E)	UTM (N)	UTM (E)	Section	Area (km^2)	Hierarchy	Scar Head Elevation(m)	Toe Elevation(m)	Scar Height (m)	Type
			Coordinates								
202	32° 31' 3.0582"	34° 39' 17.5161"	3598964	655374	N	0.2545	S	-599.41	-769.31	25	SL
203	32° 30' 46.0713"	34° 39' 55.1874"	3598456	656365	N	0.852	S	-531.76	-719.39	38	SL
204	32° 31' 4.8532"	34° 39' 46.2393"	3599031	656122	N	0.1767	T	-533.86	-607.93	39	SL
205	32° 30' 50.4945"	34° 39' 55.8289"	3598593	656380	N	0.094	T	-527.52	-590.75	39	SL
206	32° 30' 42.4140"	34° 39' 57.0235"	3598344	656415	N	0.0568	T	-523.21	-576.04	26	SL
207	32° 30' 35.2181"	34° 39' 41.5506"	3598117	656014	N	0.053	T	-543.23	-583.31	15	SL
208	32° 30' 13.2790"	34° 39' 13.9349"	3597430	655304	N	0.2662	S	-605.43	-678.76	14	SL
209	32° 30' 29.0916"	34° 39' 15.4282"	3597917	655336	N	0.0548	T	-585.72	-636.57	29	SL
210	32° 30' 17.8594"	34° 39' 19.7233"	3597573	655453	N	0.0454	T	-569.58	-628.93	35	SL
211	32° 30' 9.8248"	34° 39' 6.8066"	3597320	655120	N	0.0374	T	-595.35	-629.01	6	SL
212	32° 30' 25.6444"	34° 38' 49.0619"	3597800	654649	N	0.0975	S	-642.34	-680.7	17	SL
213	32° 30' 19.5626"	34° 38' 41.6596"	3597610	654459	N	0.0379	T	-639.7	-669.32	3	SL
214	32° 30' 30.0746"	34° 41' 44.4939"	3598009	659225	N	0.4945	P	-317.4	-410.2	12	SL
215	32° 30' 35.7446"	34° 41' 45.4380"	3598184	659247	N	0.0434	S	-315.68	-352.94	14	SL
216	32° 30' 25.4528"	34° 41' 43.9645"	3597866	659214	N	0.0519	S	-315.47	-350.82	13	SL
217	32° 28' 24.2661"	34° 42' 21.2246"	3594149	660246	N	9.036	P	-189.3	-551	50	SL
218	32° 28' 59.1110"	34° 42' 42.1668"	3595231	660775	N	0.427	S	-183.08	-247.68	8	SL
219	32° 28' 26.3359"	34° 42' 18.7803"	3594212	660181	N	0.4682	S	-195.47	-251.88	17	SL
220	32° 28' 6.1718"	34° 41' 57.8658"	3593582	659645	N	0.4449	S	-203.99	-268.87	25	SL
221	32° 28' 35.3564"	34° 41' 3.9772"	3594459	658224	N	0.0261	S	-283.7	-310.75	19	SL
222	32° 28' 36.0436"	34° 40' 43.5669"	3594472	657691	N	0.0802	S	-303.03	-328.7	9	SL
223	32° 29' 32.1126"	34° 40' 13.0969"	3596186	656868	N	1.351	P	-428.6	-560.8	11	SL
224	32° 29' 39.0656"	34° 40' 16.6086"	3596401	656956	N	0.1202	S	-406.92	-452.69	8	SL
225	32° 29' 19.9691"	34° 40' 35.7326"	3595821	657465	N	0.2661	S	-381.16	-472.18	13	SL
226	32° 29' 15.8015"	34° 40' 35.6553"	3595693	657465	N	0.0118	T	-372.56	-396.13	21	SL
227	32° 29' 12.0398"	34° 40' 23.8798"	3595572	657159	N	0.0183	T	-386.72	-414.85	22	SL

Number	Coordinates Lat (N)	Long (E)	UTM (N)	UTM (E)	Section	Area (km^2)	Hierarchy	Scar Head Elevation(m)	Toe Elevation(m)	Scar Height (m)	Type
228	32° 28' 53.6871"	34° 40' 18.4253"	3595005	657026	N	0.269	S	-378.66	-479.88	26	SL
229	32° 28' 48.0868"	34° 40' 21.5549"	3594833	657110	N	0.0476	T	-355.43	-409.44	21	SL
230	32° 29' 16.4431"	34° 39' 54.7544"	3595696	656397	N	0.807	S	-464.52	-552.39	16	SL
231	32° 29' 4.8607"	34° 39' 8.0747"	3595320	655184	N	0.4486	P	-487.9	-565.5	35	SL
232	32° 28' 52.4895"	34° 38' 42.7844"	3594929	654530	N	0.1679	P	-510.4	-549.9	25	SL
233	32° 28' 37.0825"	34° 38' 35.1868"	3594451	654339	N	0.1322	P	-519.2	-580	20	SL
234	32° 28' 40.8711"	34° 38' 26.0564"	3594564	654098	N	0.0178	S	-549.53	-564.15	5	SL
235	32° 28' 35.6249"	34° 38' 34.4027"	3594406	654319	N	0.0216	S	-527.63	-549	7	SL
236	32° 28' 29.1165"	34° 38' 32.0118"	3594205	654260	N	0.02713	P	-529.6	-542.7	7	SL
237	32° 29' 36.0705"	34° 38' 48.5233"	3596273	654659	N	5.396	P	-562.592	-864.008	15	SL
238	32° 28' 51.1234"	34° 37' 20.0195"	3594854	652370	N	1.624	P	-665.458	-825.778	44	SL
239	32° 28' 20.6462"	34° 39' 1.6196"	3593956	655036	N	0.04742	P	-470.9	-505.4	12	SL
240	32° 28' 2.7351"	34° 38' 49.9825"	3593400	654741	N	0.02132	P	-472.9	-500.7	9	SL
241	32° 27' 48.8458"	34° 38' 44.7395"	3592970	654611	N	0.0833	P	-470.7	-512.6	19	SL
242	32° 27' 38.6406"	34° 39' 21.5274"	3592670	655576	N	0.1168	P	-365.8	-422.2	33	SL
243	32° 27' 45.0740"	34° 40' 12.6316"	3592889	656908	N	4.607	P	-287.582	-546.626	10	SL
244	32° 27' 48.3899"	34° 40' 25.7020"	3592997	657247	N	0.4279	S	-258.308	-335.355	10	SL
245	32° 28' 10.8243"	34° 38' 2.2868"	3593630	653492	N	0.2192	P	-539	-600.6	26	SL
246	32° 28' 16.7816"	34° 38' 8.4221"	3593815	653650	N	0.0159	S	-536.77	-563.65	18	SL
247	32° 28' 4.3254"	34° 37' 58.3621"	3593428	653393	N	0.0098	S	-542.39	-570.31	11	SL
248	32° 28' 0.4911"	34° 37' 54.4259"	3593308	653292	N	0.0102	S	-550.24	-576.33	16	SL
249	32° 27' 54.4174"	34° 37' 47.5736"	3593118	653116	N	0.02582	P	-561.9	-590.3	22	SL
250	32° 27' 43.5419"	34° 37' 27.9332"	3592776	652608	N	0.1716	P	-561.4	-590.8	12	SL
251	32° 27' 27.1960"	34° 37' 39.9958"	3592277	652931	N	0.2012	P	-523.3	-553.8	16	SL
252	32° 27' 41.1508"	34° 37' 54.1089"	3592712	653293	N	0.0231	S	-530	-549.05	10	SL
253	32° 27' 30.8939"	34° 37' 45.5791"	3592393	653075	N	0.0598	S	-517.85	-553.44	15	SL

Number	Lat (N)	Long (E)	Coordinates UTM (N)	UTM (E)	Section	Area (km^2)	Hierarchy	Scar Head Elevation(m)	Toe Elevation(m)	Scar Height (m)	Type
254	32° 27' 20.0756"	34° 37' 37.1223"	3592057	652859	N	0.0623	S	-513.33	-546.44	14	SL
255	32° 27' 16.4015"	34° 37' 28.7118"	3591940	652641	N	0.0223	S	-524.32	-551.33	13	SL
256	32° 27' 52.0663"	34° 36' 55.3911"	3593025	651754	N	1.995	P	-619.5	-889	60	SL
257	32° 27' 45.8910"	34° 36' 49.0970"	3592833	651593	N	0.1224	S	-637.89	-725.47	10	SL
258	32° 27' 40.9057"	34° 37' 12.8998"	3592688	652217	N	0.1133	P	-571.8	-665.6	17	SL
259	32° 27' 30.5145"	34° 36' 57.3161"	3592362	651815	N	0.2594	P	-587	-709.2	17	SL
260	32° 27' 0.8056" N	34° 39' 0.4239"	3591497	655043	N	0.657	P	-365.789	-434.275	24	SL
261	32° 26' 49.0540"	34° 37' 43.0621"	3591104	653029	S	0.04661	P	-486.3	-534.2	11	SL
262	32° 26' 55.3498"	34° 37' 33.9171"	3591294	652787	S	0.2429	P	-518.9	-575.1	13	SL
263	32° 27' 3.0771" N	34° 37' 33.6372"	3591532	652776	S	0.0978	S	-511.65	-573.95	19	SL
264	32° 26' 48.1420"	34° 37' 21.6802"	3591067	652471	S	0.0356	S	-551.27	-573.54	8	SL
265	32° 26' 31.4275"	34° 37' 39.8557"	3590559	652953	S	0.3449	P	-490.4	-560.6	7	SL
266	32° 26' 36.9185"	34° 37' 40.8487"	3590729	652977	S	0.0701	S	-484.93	-532.63	15	SL
267	32° 26' 29.5429"	34° 37' 34.3166"	3590499	652809	S	0.0106	S	-505.52	-522.54	8	SL
268	32° 26' 24.7668"	34° 37' 28.7759"	3590350	652667	S	0.0213	S	-499.9	-524.33	8	SL
269	32° 26' 23.2169"	34° 37' 21.2008"	3590299	652470	S	0.0094	S	-509.52	-528.47	7	SL
270	32° 26' 23.6736"	34° 37' 16.4975"	3590311	652347	S	0.0024	S	-522.13	-531.9	4	SL
271	32° 26' 29.2053"	34° 37' 7.6517"	3590478	652113	S	0.0108	S	-542.05	-551.63	4	SL
272	32° 27' 4.4451"	34° 36' 46.6065"	3591555	651547	S	0.623	P	-622	-750.2	8	SL
273	32° 27' 16.5696"	34° 37' 6.9913"	3591937	652074	S	0.1587	S	-567.47	-651.63	15	SL
274	32° 27' 12.1699"	34° 37' 3.8723"	3591800	651994	S	0.0119	T	-573.43	-597.93	18	SL
275	32° 27' 8.6329"	34° 36' 54.4047"	3591687	651749	S	0.0054	T	-597	-614.45	9	SL
276	32° 26' 46.0578"	34° 36' 33.5186"	3590984	651214	S	0.699	P	-633.3	-750.2	15	SL
277	32° 26' 32.6226"	34° 36' 48.7735"	3590576	651619	S	0.1507	S	-582.91	-653.84	21	SL
278	32° 26' 31.1556"	34° 36' 43.8023"	3590529	651489	S	0.0709	T	-579.27	-621.11	25	F
279	32° 26' 36.3083"	34° 36' 27.7920"	3590681	651069	S	0.0831	S	-613.04	-663.77	22	SL

Number	Lat (N)	Long (E)	Coordinates UTM (N)	UTM (E)	Section	Area (km^2)	Hierarchy	Scar Head Elevation(m)	Toe Elevation(m)	Scar Height (m)	Type
280	32° 26' 1.6839"	34° 37' 47.1832"	3589646	653159	S	3.564	P	-435.9	-750.2	13	SL
281	32° 26' 11.6181"	34° 37' 34.8367"	3589947	652831	S	0.3054	S	-471	-579.28	10	SL
282	32° 26' 12.5760"	34° 37' 12.8601"	3589968	652257	S	0.0536	T	-508.11	-546.79	15	F
283	32° 25' 47.8313"	34° 37' 38.0123"	3589216	652926	S	0.0386	S	-425.76	-448.65	14	SL
284	32° 25' 49.2807"	34° 37' 18.4227"	3589253	652413	S	0.0099	S	-447.67	-473.99	18	SL
285	32° 25' 51.3046"	34° 37' 11.7637"	3589313	652238	S	0.0306	S	-460.58	-485.44	12	SL
286	32° 25' 52.7769"	34° 37' 6.3484"	3589356	652096	S	0.0074	S	-467.87	-488.94	12	SL
287	32° 25' 54.4746"	34° 37' 2.0203"	3589406	651982	S	0.0345	S	-479.61	-523.54	8	SL
288	32° 26' 5.1793"	34° 36' 44.7707"	3589729	651527	S	0.0631	S	-547.33	-575.88	14	SL
289	32° 26' 35.1177"	34° 35' 25.4006"	3590620	649440	S	2.383	P	-726.827	-956.5 m	12	SL
290	32° 27' 35.6656"	34° 33' 50.4759"	3592448	646934	S	0.1541	S	-905.963	-954.02	15	F
291	32° 27' 3.9406"	34° 35' 0.7422"	3591498	648783	S	0.02994	S	-750.2 m	-801.414	15	F
292	32° 26' 40.5885"	34° 33' 39.7464"	3590748	646679	S	1.34	P	-871.952	-972.213	14	SL
293	32° 25' 30.1237"	34° 37' 7.6452"	3588659	652141	S	3.463	P	-444.7	-867.3	8	F
294	32° 26' 10.1362"	34° 36' 3.3585"	3589866	650443	S	0.0495	S	-618.08	-667.11	39	F
295	32° 26' 4.0434" N	34° 36' 24.0151"	3589686	650985	S	0.065	S	-563.54	-621.72	12	F
296	32° 25' 57.1382"	34° 36' 34.6382"	3589478	651266	S	0.0101	S	-545.88	-578.15	4	F
297	32° 25' 53.9265"	34° 36' 39.7037"	3589381	651400	S	0.0105	S	-542.04	-560.74	5	F
298	32° 25' 52.7897"	34° 36' 46.2940"	3589348	651572	S	0.0134	S	-520.91	-547.44	3	F
299	32° 25' 44.4168"	34° 37' 5.6278"	3589098	652081	S	0.036	S	-470.74	-507.78	17	F
300	32° 25' 30.6585"	34° 37' 13.5623"	3588678	652295	S	0.1275	S	-425.8	-474.32	9	F
301	32° 25' 39.7559"	34° 36' 23.2426"	3588938	650976	S	0.0135	S	-561.83	-585.6	2	F
302	32° 25' 43.3946"	34° 36' 2.7479"	3589042	650439	S	0.0642	S	-604.34	-654.65	5	F
303	32° 25' 4.5480"	34° 36' 38.7770"	3587860	651398	S	0.68	P	-496.1	-626.2	5	F
304	32° 25' 17.7062"	34° 36' 37.2461"	3588264	651352	S	0.0426	S	-493.47	-541.54	4	F
305	32° 25' 1.6642" N	34° 36' 47.8004"	3587774	651636	S	0.0686	S	-472.65	-510.72	12	F

Number	Coordinates				Section	Area	Hierarchy	Scar Head	Toe	Scar Height	Type
	Lat (N)	Long (E)	UTM (N)	UTM (E)		(km^2)		Elevation(m)	Elevation(m)	(m)	
306	32° 25' 3.0176"	34° 36' 52.8394"	3587818	651767	S	0.0226	T	-457.3	-480.92	9	F
307	32° 24' 56.8895"	34° 36' 41.0289"	3587625	651461	S	0.0273	S	-474.58	-508.3	8	F
308	32° 24' 54.8168"	34° 36' 34.1464"	3587558	651282	S	0.0158	S	-487.65	-512.23	5	F
309	32° 24' 54.1799"	34° 36' 25.8566"	3587535	651066	S	0.0185	S	-504.21	-532.92	8	F
310	32° 23' 59.6051"	34° 37' 12.3590"	3585873	652306	S	3.3	P	-368.7	-729.1	11	F
311	32° 24' 37.7027"	34° 36' 50.0431"	3587037	651705	S	0.1	S	-426.86	-477.67	13	F
312	32° 24' 7.2399" N	34° 37' 15.8170"	3586109	652393	S	0.032	S	-367.3	-385.95	9	F
313	32° 23' 48.2609"	34° 36' 58.3641"	3585518	651946	S	0.033	S	-378.56	-396.89	12	F
314	32° 25' 26.4882"	34° 32' 51.7438"	3588448	645458	S	2.44	P	-884.751	-972.595	14	F
315	32° 25' 16.1212"	34° 34' 17.1346"	3588161	647693	S	1.618	S	-733.057	-915.828	21	F
316	32° 24' 39.1314"	34° 33' 26.5023"	3587002	646387	S	2.229	S	-735.456	-923.096	17	F
317	32° 23' 22.1300"	34° 36' 15.6512"	3584696	650842	S	0.2301	P	-427.5	-514	5	F
318	32° 23' 30.5571"	34° 36' 7.6941"	3584953	650630	S	0.0263	S	-449.17	-473.61	6	F
319	32° 23' 14.1393"	34° 35' 49.2727"	3584440	650156	S	0.0821	P	-461.4	-499.8	8	F
320	32° 22' 57.6558"	34° 36' 4.5535"	3583938	650563	S	0.656	P	-417.2	-576.6	5	F
321	32° 22' 37.6424"	34° 37' 56.8207"	3583366	653506	S	1.346	P	-249.7	-377.3	12	F
322	32° 22' 47.1438"	34° 38' 0.6088"	3583661	653601	S	0.0961	S	-252.34	-288.81	11	F
323	32° 22' 30.9982"	34° 37' 53.1686"	3583160	653414	S	0.0283	S	-250.8	-279.44	15	F
324	32° 22' 42.8500"	34° 38' 58.7764"	3583552	655123	S	1.035	P	-207.261	-292.297	9	F
325	32° 23' 55.2331"	34° 33' 52.3986"	3585660	647084	S	0.727	P	-701.6	-768.9	18	F
326	32° 23' 15.6295"	34° 32' 0.8950"	3584399	644188	S	4.368	P	-824.8	-982.3	16	F
327	32° 23' 53.7547"	34° 32' 32.2705"	3585585	644991	S	1.232	S	-747.82	-898.02	20	F
328	32° 23' 49.8874"	34° 32' 34.7887"	3585466	645058	S	0.0921	T	-746.55	-750	16	F
329	32° 23' 34.8387"	34° 32' 32.9178"	3585002	645016	S	0.0492	T	-749.92	-827.37	19	F
330	32° 23' 0.1524"	34° 32' 1.0027"	3583922	644197	S	0.1137	S	-817.24	-844.67	14	F
331	32° 22' 48.6811"	34° 31' 35.2973"	3583559	643531	S	0.0728	S	-827.91	-858.26	21	F

Number	Lat (N)	Long (E)	Coordinates UTM (N)	UTM (E)	Section	Area (km^2)	Hierarchy	Scar Head Elevation(m)	Toe Elevation(m)	Scar Height (m)	Type
332	32° 21' 4.4956"	34° 30' 56.9358"	3580336	642574	S	22.053	P	-703.7	-1112.7	18	F
333	32° 23' 51.9789"	34° 28' 43.4588"	3585445	639013	S	0.2669	S	-1030.5	-1079.5	27	F
334	32° 23' 3.5516"	34° 29' 25.2164"	3583969	640125	S	0.0918	S	-945.55	-984	14	F
335	32° 22' 53.5542"	34° 29' 51.5612"	3583671	640818	S	0.2524	S	-891.97	-950.65	21	F
336	32° 21' 45.9280"	34° 31' 21.7352"	3581622	643204	S	0.4978	S	-706.96	-829.45	36	F
337	32° 21' 8.5870"	34° 31' 9.3314"	3580467	642896	S	0.3271	S	-697.25	-750.2	25	F
338	32° 21' 9.9050"	34° 31' 17.2892"	3580511	643103	S	0.0629	T	-718.7	-750.2	6	F
339	32° 20' 29.4045"	34° 31' 20.0849"	3579264	643194	S	0.713	S	-687.3	-776.31	40	F
340	32° 20' 33.1306"	34° 31' 21.9874"	3579380	643242	S	0.1159	T	-705.4	-750.2	39	F
341	32° 20' 19.4388"	34° 30' 22.9438"	3578936	641705	S	0.1081	S	-699.59	-782.07	16	F
342	32° 20' 25.6971"	34° 30' 9.1757"	3579124	641342	S	0.0412	S	-760.91	-792.32	24	F
343	32° 20' 33.3218"	34° 29' 46.0684"	3579350	640735	S	0.1204	S	-779.24	-819.66	18	F
344	32° 20' 46.5999"	34° 29' 27.8391"	3579753	640252	S	0.0408	S	-818.47	-836.15	8	F
345	32° 20' 55.3408"	34° 29' 14.7884"	3580017	639907	S	0.0541	S	-834.67	-854.61	14	F
346	32° 21' 15.6069"	34° 28' 33.9960"	3580626	638832	S	0.102	S	-865.87	-910.13	14	F
347	32° 21' 26.1568"	34° 28' 9.7560"	3580943	638194	S	0.0664	S	-907.62	-935.89	20	F
348	32° 17' 18.2365"	34° 33' 23.5544"	3573424	646508	S	91.362	P	-449.3	-1107.7	19	F
349	32° 17' 39.7547"	34° 33' 47.2595"	3574095	647118	S	0.521	S	-387.17	-505.68	13	F
350	32° 17' 31.8898"	34° 33' 38.3515"	3573850	646889	S	0.1053	T	-415	-480.61	14	F
351	32° 17' 10.7882"	34° 33' 47.0930"	3573203	647127	S	0.2832	S	-380.22	-462.89	32	F
352	32° 17' 8.8485"	34° 33' 47.2419"	3573143	647132	S	0.1077	T	-377.4	-438.53	33	F
353	32° 17' 2.7160"	34° 33' 27.3002"	3572947	646613	S	0.0212	S	-431.35	-455.34	13	F
354	32° 16' 45.8699"	34° 33' 21.2084"	3572426	646461	S	0.2828	S	-429.8	-501.28	13	F
355	32° 16' 12.1120"	34° 31' 30.5494"	3571345	643581	S	0.288	S	-591	-634.44	16	F
356	32° 15' 58.3688"	34° 29' 55.1162"	3570886	641090	S	0.1487	S	-675.99	-720.86	20	F
357	32° 16' 1.2997"	34° 29' 13.5595"	3570961	640001	S	0.1805	S	-710.4	-752.87	31	F

Number	Coordinates				Section	Area	Hierarchy	Scar Head	Toe	Scar Height	Type
	Lat (N)	Long (E)	UTM (N)	UTM (E)		(km^2)		Elevation(m)	Elevation(m)	(m)	
358	32° 16' 17.8063"	34° 27' 42.6138"	3571437	637614	S	0.184	S	-773.55	-809.87	11	F
359	32° 16' 0.0308"	34° 33' 5.6155"	3571008	646073	S	0.3799	P	-410.7	-544.8	14	F
360	32° 16' 7.6617"	34° 33' 7.1323"	3571244	646110	S	0.0199	S	-419.55	-454.68	12	F
361	32° 16' 2.8043"	34° 33' 6.5609"	3571094	646097	S	0.0077	S	-411.18	-426.47	8	F
362	32° 15' 54.9168"	34° 33' 1.5393"	3570849	645969	S	0.045	S	-410.25	-454.93	15	F
363	32° 13' 1.6256"	34° 31' 18.5276"	3565474	643349	S	8.947	P	-479.836	-841.359	9	F
364	32° 12' 36.7233"	34° 27' 48.2946"	3564631	637856	S	15.129	P	-675.5	-1040.5	39	F
365	32° 13' 44.4062"	34° 24' 23.3491"	3566643	632463	S	0.1975	S	-865.51	-914.09	12	F
366	32° 13' 2.5778"	34° 27' 47.7931"	3565427	637832	S	0.0881	S	-695.45	-734.03	25	F
367	32° 12' 41.4988"	34° 27' 50.6023"	3564779	637914	S	0.1408	S	-676.73	-722.99	23	F
368	32° 12' 13.4735"	34° 27' 37.1472"	3563911	637574	S	0.0999	S	-681.67	-718.9	28	F
369	32° 12' 0.7407"	34° 27' 12.1910"	3563510	636926	S	0.248	S	-685.09	-723.51	15	F
370	32° 12' 11.7018"	34° 26' 33.9763"	3563834	635920	S	0.1111	S	-705.9	-750.5	14	F
371	32° 12' 16.0470"	34° 26' 12.6475"	3563960	635360	S	0.0328	S	-727.55	-761.66	20	F
372	32° 12' 21.2354"	34° 25' 55.5269"	3564114	634910	S	0.0348	S	-750.9	-783.62	25	F
373	32° 12' 23.7528"	34° 25' 6.2670"	3564175	633619	S	0.764	S	-764.55	-875.04	26	F
374	32° 12' 19.6396"	34° 25' 38.9291"	3564059	634476	S	0.0618	T	-761.3	-804.4	32	F
375	32° 12' 19.9669"	34° 25' 25.7180"	3564065	634130	S	0.0183	T	-780.6	-805.01	23	F
376	32° 12' 22.7316"	34° 25' 17.7893"	3564147	633921	S	0.0213	T	-791.9	-821.96	21	F
377	32° 12' 21.5917"	34° 25' 8.1215"	3564109	633669	S	0.0388	T	-806	-840.14	20	F
378	32° 12' 26.0690"	34° 24' 50.5690"	3564240	633207	S	0.0398	T	-823.3	-852.02	30	F
379	32° 12' 30.6422"	34° 24' 40.3601"	3564378	632938	S	0.0389	T	-830.2	-864.49	25	F
380	32° 12' 30.0482"	34° 24' 29.6517"	3564356	632658	S	0.1307	T	-829.8	-871.96	10	F
381	32° 12' 49.9766"	34° 24' 9.9228"	3564963	632133	S	0.1462	S	-853	-890.1	22	F
382	32° 02' 51.9730"	34° 22' 43.6905"	3546519	630112	S	2.311	P	-542.4	-700.3	25	F
383	32° 03' 37.6956"	34° 22' 21.3637"	3547919	629508	S	0.525	S	-567.9	-656.65	35	F

Number	Coordinates				Section	Area	Hierarchy	Scar Head	Toe	Scar Height	Type
	Lat (N)	Long (E)	UTM (N)	UTM (E)		(km^2)		Elevation(m)	Elevation(m)	(m)	
384	32° 03' 17.2759"	34° 22' 30.2372"	3547293	629749	S	0.0281	S	-562.98	-598.44	26	F
385	32° 03' 9.7653"	34° 22' 41.3055"	3547066	630042	S	0.0629	S	-544.08	-579.2	15	F
386	32° 03' 3.4765"	34° 22' 45.4205"	3546873	630152	S	0.0318	S	-536.17	-566.21	25	F
387	32° 02' 50.8099"	34° 22' 46.1942"	3546484	630178	S	0.0668	S	-529.8	-564.47	25	F
388	32° 02' 43.8146"	34° 22' 22.8953"	3546260	629569	S	0.1664	S	-556.61	-585.58	15	F
389	31° 56' 49.3154"	34° 21' 40.2559"	3535330	628588	S	15.407	P	-565	-819.3	26	F
390	31° 58' 12.9780"	34° 21' 20.7159"	3537900	628043	S	1.115	S	-639.19	-698.34	18	F
391	31° 58' 8.1157"	34° 21' 28.9242"	3537753	628260	S	0.0749	T	-624.6	-677.59	16	F
392	31° 57' 34.8185"	34° 21' 17.2331"	3536724	627966	S	0.1299	S	-615.32	-666.56	18	F
393	31° 56' 29.0800"	34° 22' 47.3181"	3534729	630357	S	0.738	S	-401.2	-589.07	24	F
394	31° 55' 24.1639"	34° 20' 7.6593"	3532678	626190	S	3.809	P	-603.6	-781.9	45	F
395	31° 55' 30.3466"	34° 20' 16.2229"	3532871	626412	S	0.1102	S	-593.56	-642.36	22	F
396	31° 53' 9.0420"	34° 20' 2.5928"	3528515	626108	S	40.596	P	-483.3	-955	50	F
397	31° 57' 1.8026"	34° 16' 46.7329"	3535621	620877	S	0.0275	S	-831.47	-848.29	13	F
398	31° 56' 53.6004"	34° 16' 54.7158"	3535371	621090	S	0.0373	S	-824.18	-844.77	13	F
399	31° 56' 42.5558"	34° 17' 2.6587"	3535033	621302	S	0.0406	S	-813.95	-836.79	15	F
400	31° 56' 25.4964"	34° 17' 16.3907"	3534512	621669	S	0.0508	S	-796.99	-819.24	13	F
401	31° 56' 10.3536"	34° 17' 28.8993"	3534050	622003	S	0.1576	S	-774.47	-809.1	19	F
402	31° 55' 54.2456"	34° 17' 58.1108"	3533563	622776	S	0.1626	S	-738.44	-776.74	19	F
403	31° 55' 43.6849"	34° 18' 31.7198"	3533248	623663	S	0.2105	S	-707.23	-744.72	17	F
404	31° 54' 56.0301"	34° 19' 44.5383"	3531804	625593	S	0.581	S	-587.51	-667.04	21	F
405	31° 54' 13.5817"	34° 20' 2.9794"	3530503	626093	S	0.4664	S	-532.37	-619.19	38	F
406	31° 53' 26.0771"	34° 20' 16.4446"	3529044	626465	S	0.562	S	-468.61	-572.41	40	F
407	31° 52' 16.6554"	34° 20' 27.6841"	3526910	626787	S	1.937	S	-390.1	-552.99	26	F
408	31° 53' 3.8775"	34° 20' 5.2174"	3528357	626179	S	0.0559	T	-460.5	-527.54	31	F
409	31° 52' 48.3177"	34° 20' 19.4359"	3527883	626558	S	0.2193	T	-429.5	-527.26	20	F

Number	Coordinates Lat (N)	Long (E)	UTM (N)	UTM (E)	Section	Area (km^2)	Hierarchy	Scar Head Elevation(m)	Toe Elevation(m)	Scar Height (m)	Type
410	31° 52' 38.5665"	34° 20' 32.1353"	3527587	626896	S	0.1316	T	-396.6	-467.71	45	F
411	31° 52' 7.1893"	34° 20' 11.6315"	3526614	626369	S	0.0533	T	-403.5	-460.91	39	F
412	31° 52' 9.7660"	34° 19' 47.3192"	3526685	625729	S	0.612	T	-422.9	-561.06	28	F
413	31° 52' 47.5647"	34° 18' 11.4456"	3527819	623196	S	0.2586	S	-607.56	-644.1	30	F
414	31° 52' 58.4496"	34° 17' 55.4439"	3528149	622771	S	0.0645	S	-626.48	-645	11	F
415	31° 54' 35.2451"	34° 17' 15.2562"	3531117	621680	S	0.0711	S	-725.12	-749.5	10	F
416	31° 54' 53.5590"	34° 16' 42.3242"	3531670	620808	S	0.3652	S	-749.02	-795.59	18	F
417	31° 50' 42.7253"	34° 19' 18.6583"	3523996	625008	S	15.992	P	-395.1	-764.7	53	F
418	31° 53' 20.7265"	34° 16' 44.9223"	3528813	620910	S	0.2269	S	-692.82	-735.17	9	F
419	31° 53' 1.8421"	34° 17' 10.1953"	3528239	621581	S	0.1539	S	-655	-697.33	19	F
420	31° 52' 5.2189"	34° 18' 22.2975"	3526518	623496	S	0.0678	S	-559.81	-599.2	29	F
421	31° 51' 51.1279"	34° 19' 2.8610"	3526097	624568	S	0.3147	S	-488.62	-570.12	40	F
422	31° 51' 17.2651"	34° 19' 28.0776"	3525062	625243	S	0.4016	S	-409.05	-505.51	44	F
423	31° 50' 48.4248"	34° 19' 23.1458"	3524173	625124	S	0.1757	S	-393.8	-474.78	61	F
424	31° 50' 31.2830"	34° 19' 13.8443"	3523642	624886	S	0.1442	S	-391.68	-464.05	54	F
425	31° 50' 13.9997"	34° 18' 47.8978"	3523101	624211	S	0.2262	S	-406.58	-491.78	70	F
426	31° 50' 20.0665"	34° 18' 21.8550"	3523280	623524	S	0.0421	S	-473.76	-509.62	25	F
427	31° 50' 26.7061"	34° 18' 11.1168"	3523481	623239	S	0.0354	S	-495.57	-527.31	22	F
428	31° 51' 40.7401"	34° 17' 3.1162"	3525739	621425	S	0.1825	S	-618.2	-664.64	20	F
429	31° 51' 57.1991"	34° 16' 26.3732"	3526235	620453	S	0.1163	S	-672.05	-697.31	19	F
430	31° 49' 38.1281"	34° 18' 6.4725"	3521984	623135	S	29.807	P	-439	-831.9	36	F
431	31° 51' 44.3753"	34° 16' 17.0418"	3525837	620212	S	1.542	S	-650.94	-736.33	15	F
432	31° 50' 5.0055"	34° 18' 35.0909"	3522820	623877	S	0.4374	S	-420.05	-487.58	40	F
433	31° 48' 57.3644"	34° 17' 48.4214"	3520723	622675	S	0.533	S	-425.37	-526.57	41	F
434	31° 49' 31.7267"	34° 14' 5.6840"	3521713	616807	S	1.582	S	-671.86	-720.13	14	F
435	31° 46' 40.6064"	34° 16' 40.5956"	3516491	620941	S	39.221	P	-390.711	-979.16	90	F

Number	Lat (N)	Long (E)	Coordinates UTM (N)	UTM (E)	Section	Area (km^2)	Hierarchy	Scar Head Elevation(m)	Toe Elevation(m)	Scar Height (m)	Type
436	31° 52' 45.8666"	34° 11' 16.5673"	3527641	612295	S	0.104	S	-392.58	-479.2	14	F
437	31° 52' 29.7033"	34° 11' 20.6546"	3527145	612408	S	0.075	S	-879.08	-903	20	F
438	31° 51' 29.2809"	34° 11' 40.2017"	3525290	612942	S	0.0584	S	-836.22	-869.67	31	F
439	31° 51' 0.2510"	34° 11' 47.8489"	3524398	613153	S	0.0326	S	-819.69	-849.62	21	F
440	31° 50' 42.8750"	34° 11' 54.2160"	3523865	613326	S	0.093	S	-800.53	-842.32	41	F
441	31° 50' 25.6779"	34° 12' 8.8859"	3523340	613718	S	0.2597	S	-775.76	-831.22	31	F
442	31° 49' 47.7231"	34° 12' 44.5532"	3522181	614668	S	0.524	S	-744.79	-796.32	36	F
443	31° 49' 50.5735"	34° 12' 44.8943"	3522269	614676	S	0.0836	T	-742.6	-784.95	16	F
444	31° 48' 19.8910"	34° 15' 17.9416"	3519523	618732	S	0.756	S	-568.88	-660.42	24	F
445	31° 48' 4.6939"	34° 15' 34.8531"	3519060	619182	S	0.0429	T	-579.9	-609.67	24	F
446	31° 47' 44.0504"	34° 16' 1.0906"	3518432	619880	S	0.0577	S	-531.39	-576.59	37	F
447	31° 47' 11.8387"	34° 16' 51.5118"	3517456	621217	S	0.0736	S	-886.18	-906.07	52	F

תקציר

לאורך מדרון היבשת מול חופי ישראל נראות בפני השטח גלישות מדרון תת ימיות רבות, המצביעות על כך שהסדימנטים באזור זה אינם יציבים. אי היציבות שגורמת לגלישות כנראה קשורה לתהליכים טבעיים של בניית מדרון יבשתי על ידי סדימנטציה וכן לאוופוריטים המסיניים הנמצאים בבסיס הסדימנטים. עבודות קודמות שנעשו באזור התרכזו בתופעות הגדולות, שכונו 'הפרעות' כמו הפרעת פלמחים והפרעת דור וכן במיפוי בסיסי של ההעתקים שנצפו על מדרון היבשת. עקב הרזולוציה הזמינה, העבודות קודמות היו מנועות מלזהות כשלים קטנים יחסית, שיכולים להצביע על תהליכים משמעותיים של חוסר יציבות ועיצוב הנוף התת ימי. בעבודה זו אנו מראים שהנוף של שולי היבשת מושפע ביותר מחוסר יציבות, שמעצבת את קרקעית הים בתהליך מתמשך. השתמשנו בנתוני multi-beam ובחתכים סייסמיים, שניהם ברזולוציה גבוהה על מנת למפות ולבחון את הגלישות וההעתקים הקטנים יחסית. בנוסף השתמשנו בכלים סטטיסטיים לבחינת התפלגות שטחי הגלישות ולצורך השוואות לעבודות דומות בעולם. כמו כן, השתמשנו בתוכנות מיפוי לצורך חישובים של שיפועי המדרון ומיפוי שכבת המלח המסיני. מצאנו, שהגלישות וההעתקים נוצרים במנגנונים שונים שאינם תלויים זה בזה. הגורם העיקרי המשפיע על יצירת הגלישות הוא זווית המדרון וגורם עיקרי במנגנון יצירת ההעתקים הוא זרימת המלח המסיני לכיוון האגן. מתוך הממצאים שלנו אנחנו מסיקים כי קרקעית הים התיכון באזור שולי היבשת של ישראל כנראה פעילה עד היום מבחינה גאומורפולוגית. חשיבות תחום המחקר היא באימות ותיקוף מודלים של סיכונים סייסמיים וסיכוניי צונאמי, וכמו כן לצורך תכנון של מיקום צינורות גז ותשתיות אחרות על גבי הקרקעית. המחקר יכול לשמש כמיפוי לדוגמא של אזור בשולי הים התיכון ולשפוך אור על חוסר יציבות ותהליכי עיצוב נוף תת ימיים בים התיכון ובאזורים דומים בעולם.

תהליכים פעילים בעיצוב השוליים היבשתיים
מול חופי ישראל
על ידי גלישות והעתקים

עבודת גמר לתואר מוסמך במדעי הטבע

מוגשת על ידי:

עינב ראובן

בהדרכת:

ד"ר עודד כץ

פרופ' עינת אהרונוב

כסלו, תשע"ו

דצמבר, 2015

החוג לגיאולוגיה

המגמה למדעי כדור הארץ

הפקולטה למדעי הטבע

האוניברסיטה העברית בירושלים